Thermal Optimization of Flat Plate PCM Capsules in Natural Convection Solar Water Heating Systems

by

Padideh Sarafraz, B.A.Sc., Civil Engineering

University of Tehran

A thesis submitted to the

Faculty of Computational Science and Engineering

in partial fulfillment of the requirements for the degree of

Master of Applied Science in

Computational Science and Engineering

Department of Computational Science and Engineering

McMaster University

Hamilton, Ontario, Canada

September, 2013

The undersigned hereby recommends to the

Faculty of Graduate and Postdoctoral Affairs

acceptance of the thesis

Thermal Optimization of Flat Plate PCM Capsules in Natural Convection Solar Water Heating Systems

Submitted by **Padideh Sarafraz, B. A. Sc., Civil Engineering**

University of Tehran

in partial fulfillment of the requirements for the degree of

Master of Computational Science and Engineering

Dr. Marilyn F. Lightstone, Supervisor

Dr. James S. Cotton, Co-supervisor

Dr. Bartosz Protas, Examiner

Dr. Samir Ziada, Examiner

Department of Computational Engineering and Science

McMaster University

October, 2013

Abstract

This research is concerned with CFD modelling of thermal energy storage tanks containing water with submerged phase change materials (PCM). Under appropriate operating conditions, the energy density of this hybrid system can be significantly increased (two to five times) relative to a system containing water only. However, due to low thermal conductivity of phase change materials, the geometry and configurations of the PCM capsules in the tank should be optimized.

This research focused on the assessment of flat plate PCM modules submerged in a rectangular water tank. The encapsulation of the PCM within the slender flat plates resulted in a large PCM surface area and a reduction in the internal heat transfer resistance. The water was heated by coils placed at the bottom of the tank. The resulting natural convection currents acted to transfer heat from the hot coils to the PCM modules which were treated as isothermal at the PCM melt temperature.

It is concluded that the charge rate of the system increases to 2.8 times by increasing the PCM volume percentage from 2.5% to 15%. However for PCM volume percentages of more than 15%, the area of the PCM became much more

than the area of the coil (around 15 times) in a way that the charge rate of the system started to be controlled by the coil. In this stage, the charge rate of the system remained constant, and adding modules to the system only increased the heat capacity of the system. Therefore the charge rate of the system could only increase if the coil surface area was increased.

The heat transfer coefficients of the PCM modules and coil tubes were higher than those evaluated by the experimental correlations for natural convection. This was due to the recirculation of the flow in the tank "pumping effect" created by the coil for PCM modules and by the PCM modules for the coil.

It was also concluded that superheating of the PCM surface temperature decreases the heat transfer rate to the PCM significantly, and the charge rate of the system varies linearly with the temperature difference between the PCM modules and the coil.

Acknowledgements

I would like to thank Dr. Marilyn F. Lightstone and Dr. James. S. Cotton for their significant assistance and helpful advice throughout the course of this work. Dr. Cotton gave me great insights on heat transfer problems, and he is a great leader for the TMRL group. Dr. Lightstone is very knowledgeable and dear, from whom I learned enormously on both academic matters and career life. She is my inspiration.

I would also like to thank Stephen Murray, Matthew Cernick, Assad Jan, and everyone else in JHE 215 for their help and support. I would also like to thank the TMRL group for their great insight and helpful discussions. I learned a lot from them all.

Special thanks to my mother, Kefaiat, and my father, Gholamali for their never-ending devotion for the whole family, my brother, Rouzbeh, for his enormous care and guidance, my sister, Azadeh, for her encouragements and support, and my twin sister, Pazireh, who always cared for me and gave me confidence.

Last but not least, I would like to thank Natural Sciences and Engineering Research Council (NSERC) for financial support, Smart Net-Zero Energy Buildings Strategic Network, and ANSYS for providing the CFD code.

Table of Contents

List of Tables

Table of Figures

Nomenclature

Symbols	definition	Units
C	specific heat	$L^2T^{-2}\Theta^{-1}$
H_{fg}	heat of fusion	L^2T^{-2}
T	static (thermodynamic) temperature	Θ
ΔT	temperature difference	Θ
T_s	surface temperature	Θ
T_∞	bulk temperature	Θ
T_f	film temperature, $(T_\infty + T_s)/2$	Θ
E	energy stored	ML^2T^{-2}
M	mass	M
V	volume	L^3
t	time	T
h	heat transfer coefficient	$MT^{-3}\Theta^{-1}$
Δt	time step	T
$\vec{U}$	vector of velocity	LT^{-1}
U	velocity magnitude	LT^{-1}
u	fluctuating velocity component in turbulent flow	LT^{-1}
i	Cartesian components of vectors taking the values 1, 2 or 3	-

j	Cartesian components of vectors taking the values 1, 2 or 3	-
p	static (thermodynamic) pressure	$ML^{-1}T^{-2}$
S_M	momentum source	$ML^{-2}T^{-2}$
S_E	energy source	$ML^{-1}T^{-3}$
e	internal energy	ML^2T^{-2}
g	gravity	LT^{-2}
k	turbulence kinetic energy per unit mass	L^2T^{-2}
	thermal conductivity	$MLT^{-3}\Theta^{-1}$
P_k	turbulence production due to viscous forces	$ML^{-1}T^{-3}$
$P_{kb}, P_{\varepsilon b}, P_{\omega b}$	turbulence production due to buoyancy	$ML^{-1}T^{-3}$
L	length	L
x, y	cartesian coordinates	L
X, Y	dimensionless coordinates	-
V_o	buoyancy velocity, $V_o = \sqrt{g\beta H\Delta T}$	LT^{-1}
v	fluid velocity component in y direction	LT^{-1}
A	surface area	L^2
$\dot{Q}$	heat transfer rate	ML^2T^{-3}

Greek Symbols

Symbols	definition	Units
ρ	density	ML^{-3}
φ	PCM volume percentage	-
τ	time constant (in chapter 3)	-
	shear stress (in chapter 4)	$ML^{-1}T^{-2}$
μ	molecular (dynamic) viscosity	$ML^{-1}T^{-1}$
μ_t	turbulent viscosity	$ML^{-1}T^{-1}$
λ	thermal conductivity	$MLT^{-3}\Theta^{-1}$
β	coefficient of thermal expansion	Θ^{-1}
ν	kinematic viscosity	L^2T^{-1}
θ	non-dimensional temperature	-
δ	Boundary layer thickness	L

Subscripts

Symbols	definition	Units
s	solid phase	-
l	liquid phase	-
m	melting	-
w	water	-
i	initial	-
tot	total	-

PCM	phase change material	-
PCM-melt	melted PCM	-
$coil$	coil	-
H	hot surface	-
C	cold surface	-
ND	dimensionless value	-
f	at the film temperature	-
	fluid	-
b	body	-

Superscript

Symbols	**definition**	**Units**
0	value at the previous time step	-
‾	average value	-

Dimensionless Numbers

Symbols	**definition**	**Units**
Ra	Rayleigh number; $Ra = \frac{g\beta(T_h - T_c)L^3}{\nu\alpha}$	-
v_{ND}	Dimensionless velocity vector; $v_{ND} = \frac{v}{\sqrt{g\beta L(T_h - T_c)}}$	-
Pr	Prandtl number; $Pr = \frac{C_p\mu}{k}$	-
Nu	Average Nusselt number; $\overline{Nu} = \frac{hL}{k_f}$	-
Bi	Biot number; $Bi = \frac{hL}{k_b}$	-

CHAPTER 1 Introduction

1. The Importance of Thermal Storage

The ever increasing human population, fast growing energy demand, depletion of fossil fuels, and their proven harmful effects on our environment, have created a need for scientists and researchers to find alternative sustainable energy sources, as well as practical ways of reducing energy use, and energy waste. Developing effective methods for thermal storage is integral to this since there is a mismatch between when the renewable energy (or waste thermal energy) is available and

when it is needed, the requirement for thermal energy storage has risen and attracted much attention among researchers.

Thermal energy storage (TES) systems are used in numerous applications including solar thermal storage, refrigeration and air conditioning and industrial waste heat recovery. Zalba et al. [1] and Sharma et al. [2] have reviewed different fields in which TES systems have important roles.

2. Thermal Energy Storage Systems

A thermal energy storage system typically consists of one or more tanks, a charging circuit, discharging circuit, and heat transfer fluid (HTF). The charging and discharging circuits may also include pumps and heat exchangers. A heat transfer fluid is employed to transfer energy from the source to the tank and the tank to the load. A typical solar energy system is shown in Figure 1. In this system, during the charging period, hot fluid is fed to, and cold fluid is extracted from the tank. During discharging, the reverse happens as cold fluid is fed to the system, and hot fluid is transferred to the load. The fluid in the tank may be thermally stratified as a result of buoyancy forces. Maintaining thermal stratification in a TES system is crucial to the efficiency of the systems, since it both enhances the performance of the collector (heat source) and helps meet the requirements of the heat load. The enhanced energy collection arises from the collector receiving colder fluid hence reducing collector heat losses whereas the

hotter the fluid that goes to the heat load, the less auxiliary energy is needed to heat the fluid to the demand temperature.

There are a number of parameters that affect the degree of stratification [3]. These include the volume and configuration of the tank, the size, location, and the design of the inlets, outlets and flow rates of the charging and discharging fluids, and the duration of charging, storing and discharging periods. Mechanisms that tend to de-stratify tanks include heat losses to the surrounding environments, heat conduction between hot and cold regions, conduction along the tank wall and fluid mixing during charging and discharging [3].

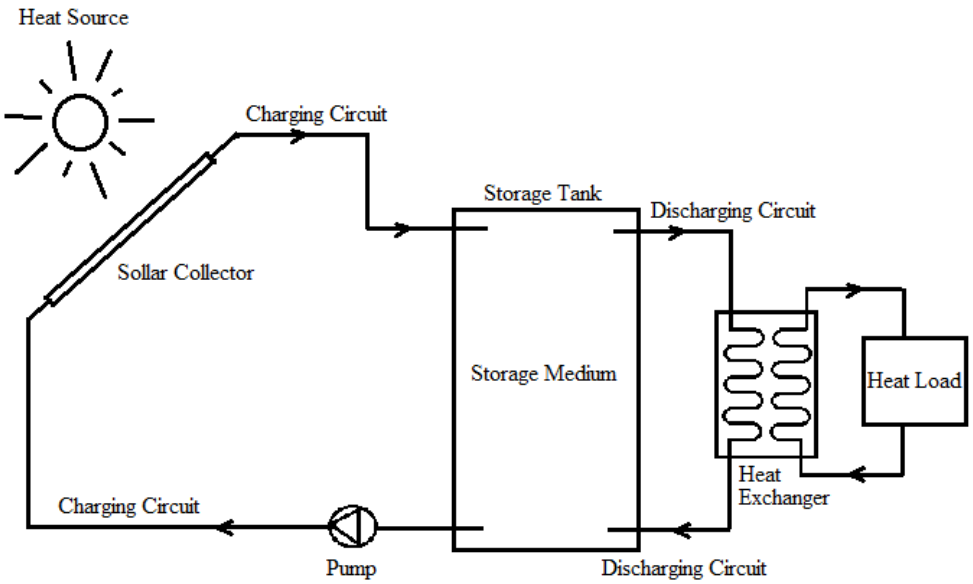

Figure 1-A sketch of a typical solar energy storage system

Depending on their application and energy demand, thermal energy storage systems can have different configurations. These are described below.

2.1. Direct (Open-loop) versus Indirect (Closed-loop) Energy Storage:

A heat storage system can be charged and discharged either directly or indirectly. In a direct storage system, the HTF is the same as the heat storage medium, and they are in direct contact. In other words, during the charging period, the heated fluid flows into the storage tank, and during discharging hot fluid is extracted from it. For example, in Figure 1, the TES system is discharged directly. However, in an indirect system, the HTF composition is different from the one of storage medium, and the heat transfer is carried out through a heat exchanger. The system shown in Figure 1 is charged indirectly. Indirect systems are mainly used when corrosion of the tank is a concern, or there is a possibility of freezing occurring within the collector. Glycol is often used under such conditions as the HTF with the collector.

In indirect systems, the heat exchanger can be located inside the tank (immersed heat exchanger), or outside the tank (side-arm heat exchanger as shown in Figure 1.) The immersed coil heat exchanger is usually placed at the bottom of the tank to heat up the coldest region of the tank, and ensure the highest heat transfer rate. However this configuration will result in the heated fluid rising and thus mixing the thermal layers in the tank. Therefore these types of tanks are usually considered fully mixed tanks. The tanks with side-arm heat exchangers, however, can maintain stratification, since cold fluid from the bottom of the tank goes through the heat exchanger, is heated up and enters the tank from the top. But this way the fluid can still be colder than the fluid at the top of the tank (plume

entrainment can occur). This process can be driven through natural convection or a pump [4].

2.2. Active versus Passive Systems

Active TES systems use a pump as the driving force for the heat transfer fluid. Passive systems, also called thermo-syphon systems, use the principal that hot water rises naturally. Therefore in these systems, the storage tank is located above the heat source, and as the HTF is heated, it rises and enters the tank. Some systems use a combination of actively and passively driven flows. The system shown in Figure 1 is actively charged and passively discharged.

2.3. Single- versus Multi-Tank Systems

Large energy storage requirements can be met through the use of a single large tank or through multi-tank systems. Multi-tank systems are generally more convenient and economical than using one single very large tank. Regular sized tanks are more easily available in the market as pre-fabricated tanks, and can be carried and fit through doorways, therefore they are more economical.

The tanks in a multi-tank system can be connected in parallel or series, depending on the application and purpose. These two configurations can have their own advantages and disadvantages which will be discussed in the next chapter. Figure 2 shows direct charging in parallel and series multi-tank systems.

2.4. Short Term versus Long Term Systems

A TES system can be classified as being either diurnal (short term) or seasonal (long term). For example a borehole TES system is considered as a seasonal energy storage which provides hot water during the winter. These types of systems have a much higher heat capacity in comparison to short term systems [3].

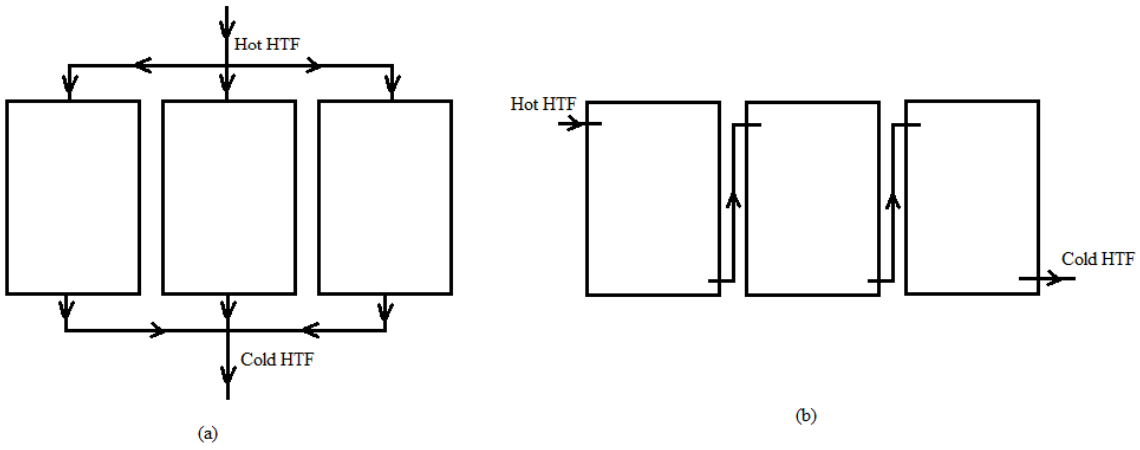

Figure 2-Direct charging in a multi-tank system (a) Parallel (b) Series

2.5. Thermal Energy Storage Methods: Sensible, Latent, and Chemical Energy Storage

TES systems can store heat in three different ways: (1) sensible, (2) latent and (3) chemical energy storage. Sensible energy storage (SES) systems store energy in the form of increased temperature of the storage medium. The capacity of this

system depends on the amount of storage medium used, its specific heat and the change in temperature. In latent energy storage (LES) systems, the storage medium undergoes a phase change when charging and discharging. The change in phase may be solid-liquid, solid-gas, solid-solid or liquid-gas transformations. These kinds of systems can reduce the size of a sensible heat storage system significantly, if the majority of energy storage is through phase change. Chemical energy storage (CES) systems use a reversible thermochemical reaction to store and release energy. While thermochemical systems can contribute to a significant reduction in the volume of an SES, they are not financially viable for low temperature storage systems

Phase change materials (PCM) usually have low heat capacities before and after changing phase. This deprives us from being able to fully take advantage of PCMs when used in TES systems with wide working temperature ranges (more detail on this matter is given in Chapter 3.) Phase change materials typically have low thermal conductivities, which can reduce the charge and discharge rates. Therefore careful design of PCM based thermal storage systems is required in order to exploit the advantages of PCM while minimizing the disadvantages [3].

3. Problem Definition

The system under consideration for the current work is motivated by the multi-tank storage technique as described by Mather et al. [6]. This system is charged

and discharged in series. Energy is added from hot water heated by solar energy which flows through coils at the base of each tank (closed-loop charging). A schematic showing the multi-tank concept is shown in Figure 3. Similarly, energy is extracted by running cool water through coils at the top of the tank. The multi-tank system allows for tank-to-tank stratification which has been shown to enhance overall system performance [6]. More detail on the behavior of this system is given in the next chapter.

The energy density of the multi-tank system can be further enhanced through use of PCM. The idea is to introduce a different type of PCM (with a different melt temperature) into each tank, Figure 4. This will allow for the concept of a 'tuned' energy storage system to be assessed. By applying a different type of PCM into each tank, it is proposed that this will allow for better control of the temperature of each tank which should enhance tank-to-tank stratification. The goal of the current research is to determine heat transfer characteristics of different PCM configurations within the tanks to ensure high heat transfer rates from the water to the PCM while maintaining a large energy density of the system. This study will focus on the single tank behaviour alone.

Careful design of the PCM encapsulation geometry is required to help overcome the other challenges inherent in PCM such as the low thermal conductivity. Parameters such as PCM volume percentage and PCM specific surface area play an important role in determining the heat transfer rate to PCM. The geometry of PCM capsules is also influential since it defines how PCM interact with the

natural convection flow in the tank. The tank geometry considered will be that used in Mather et al.'s work (2002) and consists of a 58 cm wide, 77 cm high, cylindrical tank containing a coil at the bottom. The commercial computational fluid dynamics code ANSYS CFX is used to simulate the heat transfer and fluid in a tank containing PCM capsules of different geometries and volumes. Preliminary validation is performed for natural convection problems (both laminar and turbulent) to provide confidence in the result. The goal of the research is to study the heat transfer characteristics of different PCM configurations and volume percentages during the melting phase of the process. The heat transfer coefficients predicted from the CFD simulations can then be used to create a multi-tank model which will allow for exploration of the tuned-storage concept.

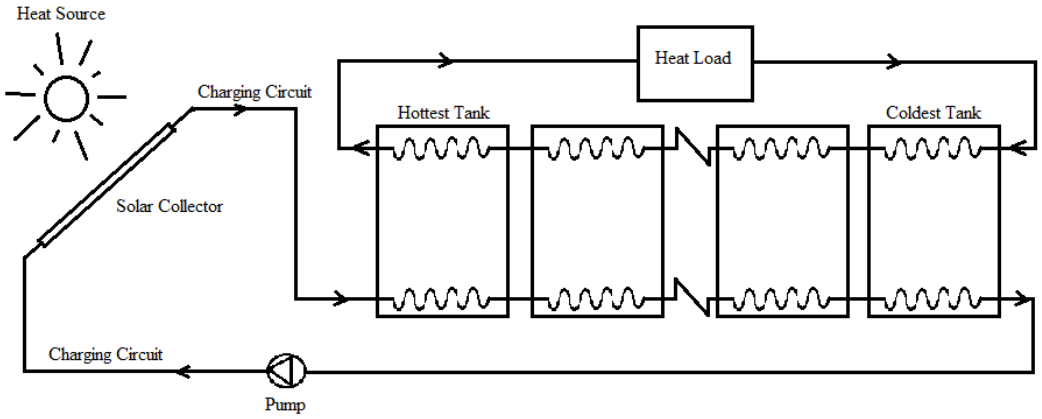

Figure 3-Multi-tank thermal storage system proposed by Mather et al. [6]

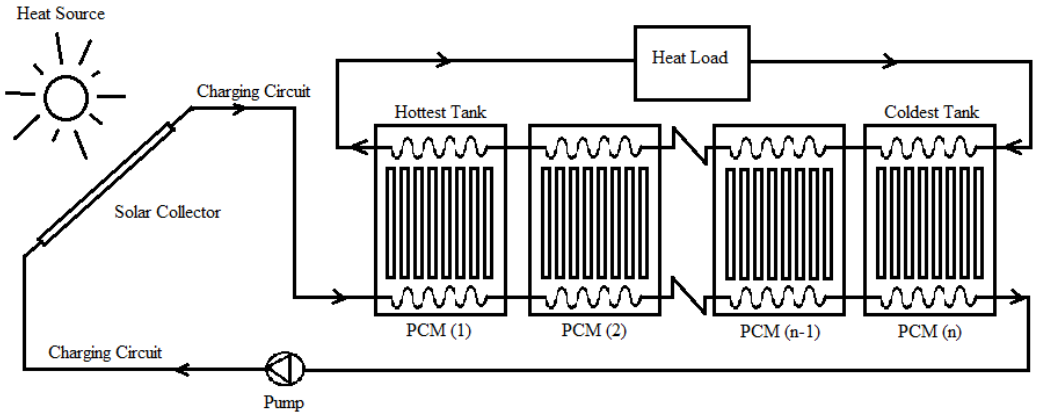

Figure 4-A schematic of the tuned energy storage

4. Contribution of Research

This work has:

a. developed a CFD model for a two dimensional tank containing PCM in ANSYS CFX environment.

b. investigated the performance of the system for different geometries, amounts and configurations of PCM.

5. Organization of Research

This study is conducted over a span of two years towards a master's degree in Computational Engineering and Science at McMaster University. A conference paper has been published during this study. The information provided in this study is presented in six chapters:

Chapter 1 presents an introduction to thermal energy storage systems, thermal stratification, different configurations of the system, and the scope of this study;

Chapter 2 presents a review of the studies conducted on multi-tank storage systems, PCM based storage systems, multi-PCM storage systems, and different PCM module geometries used;

Chapter 3 presents results of a lumped system model to assess the feasibility of the hybrid water/PCM storage medium which motivates the need for use of CFD to study PCM module configurations;

Chapter 4 presents the CFD modeling approach for the hybrid water/PCM tank, geometry, grid, boundary conditions, and turbulence model used;

Chapter 5 presents the results of the simulations, and an analysis of the results;

Chapter 6 presents conclusions and recommendations for future work;

Appendix A presents validation studies for heat transfer calculations in laminar and turbulent flows;

Appendix B presents a short description of the CFD method;

Appendix C presents experimental correlations for natural convection used in this study;

CHAPTER 2 Literature Review

1. Introduction

This chapter summarizes recent advances in enhancing the performance and cost efficiency of thermal energy storage (TES) systems. It begins with a discussion of multi-tank systems followed by a review of phase change materials for thermal energy storage.

2. Multi-tank Systems: Motivation and Performance

Economic advantages of using multi-tank systems over single tank systems for large storage volumes have motivated researchers to investigate and compare the

performance of these systems. Multi-tank systems, as discussed in the previous chapter, can be parallel/series, direct/indirect, and can have an immersed coil or a side arm heat exchanger.

In 2002, Mather et al. [6] investigated experimentally the performance of a series indirect charge and discharge multi-tank system with immersed coil heat exchangers. A schematic of their system is shown in Figure 3 of chapter 1 and for convenience is also shown here in Figure 5. In their study, they subjected an eight-tank 1600 l storage system, to various water inlet temperature scenarios. Although each tank in the system is at an effectively uniform temperature, they were able to demonstrate a high degree of tank to tank stratification. The system exhibited significant heat transfer between the coil and the fluid in the tank only if the fluid in the coil is hotter than the fluid in the tank. This is because of the fact that the coils are placed near the bottom of the tank and the unstable stratification occurs when water with higher temperature is located at a lower level from water with lower temperature. The unstable stratification results in significant natural convection heat transfer. In contrast, if the fluid entering the coil is cooler than the fluid within the tank, a stable stratification results and natural convection heat transfer is diminished. This phenomena ensures that the heat transfer is dominant in one direction resulting in a ‘thermal diode’ effect.

Cruickshank and Harrison [8] investigated the thermal performance of an indirect charge, direct discharge multi-tank system with side arm heat exchangers in the charge-loop using experimental data and computer simulation. Their multi-tank

system consisted of three 270 l tanks (a total volume of 810 l) connected in parallel or series, Figure 6. They reported that although high degrees of stratification can occur in both parallel and series configurations, slightly higher storage rates were achieved in the parallel configuration.

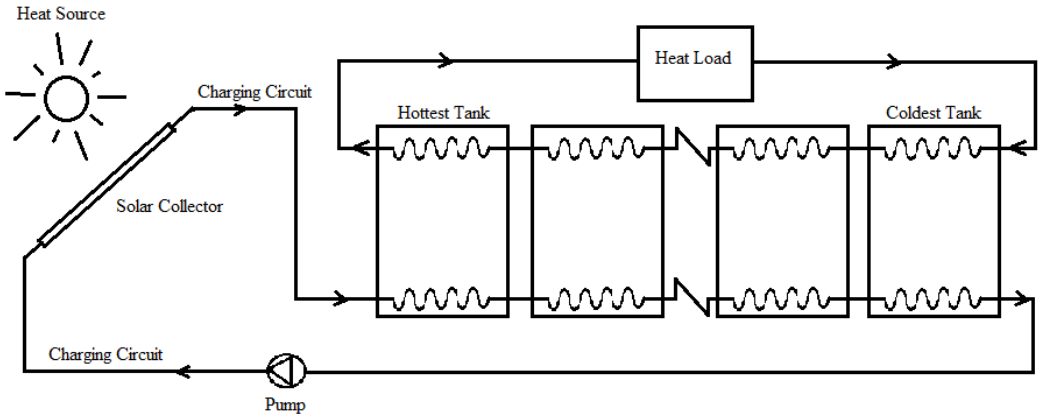

Figure 5-Multi-tank thermal storage system proposed by Mather et al. [6]

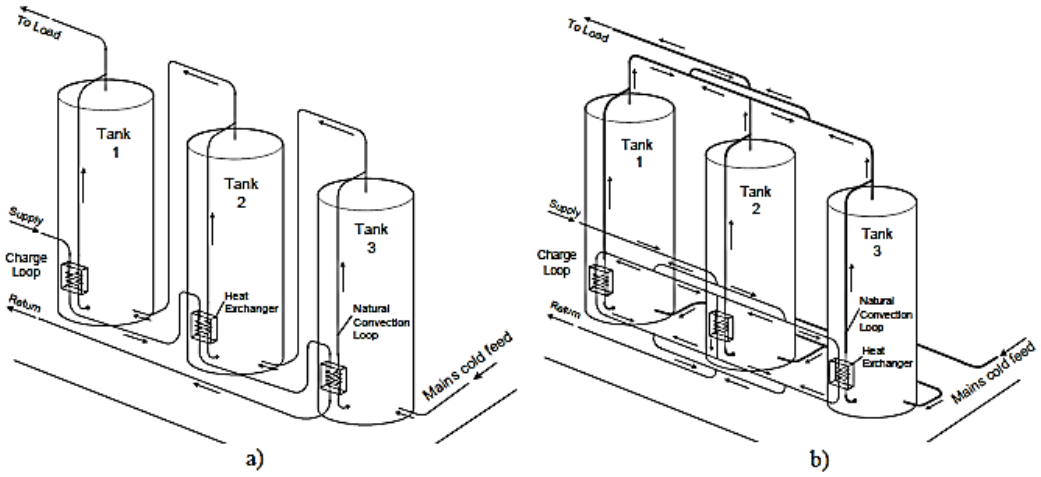

Figure 6-Multi-tank storage configurations studied: a) series-connected for charge and discharge, and b) parallel-connected for charge and discharge [8]

In Cruickshank and Harrison's following study in 2011 [9], they demonstrated that due to tank to tank stratification in the series charging, higher water

temperatures were achieved during high collector output power in comparison to parallel charging. During periods of falling collector output temperature, cooler water was deposited at the top of the tanks in both cases and caused de-stratification. However in the series configuration the level of de-stratification was lower, since stratification was maintained from tank to tank. De-stratification did not occur when Mather et al. [6] subjected their system to cooler water temperature, since they mounted their heat exchangers at the very bottom of the tanks, where water temperature is coldest. Cruickshank and Harrison [9] also showed the heat transfer rate is independent of the magnitude of the charge-loop flow rate. Therefore higher charge-loop flow rates in the series configuration resulted in water leaving the first tank without losing much energy and entering the second tank with almost the same temperature as before. This caused similar temperature distributions between the tanks in series and parallel configurations as if the series case was connected in parallel [9].

Dickinson et al. (2012) [10] continued Cruickshank's work by experimentally and computationally investigating the thermal behavior of the multi-tank systems described above with different configurations, when subjected to standard draw profiles. They studied three different configurations: series charge and series discharge, parallel charge and parallel discharge, and series charge and parallel discharge.

In series discharging, significant mixing occurred at the bottom of the tanks, since warm water from the top of the tanks entered the cooler region at the bottom of

the previous ones. However in parallel discharging, stratification was maintained, which in turn improved performance during charging, since cold water was available at the bottom of the tanks to go to the collector. At the end, they concluded that indirect series charging and direct parallel discharging is the best configuration out of the three studied.

From a comparison of the multi-tank systems studied the proposed system of Mather et al. [6] has a number of advantages. The placement of the coil at the bottom and top, for charging and discharging, respectively, allows for a thermal diode effect to occur. This enhances stratification for both conditions. Furthermore, the tanks are not subjected to mains pressure, inexpensive non-pressurized tanks or containers are suitable for this system.

3. PCM-based Tanks: Motivation and Performance

Phase change materials (PCM) have been incorporated into thermal storage systems, because of their operational advantages such as smaller temperature fluctuations, smaller size and lower weight per unit of storage capacity [11]. A beneficial by-product of using PCMs in a latent heat energy storage (LES) system is that during the phase change process, PCM remains at an almost constant temperature, and provides a constant driving force for heat transfer between inlet heat transfer fluid (HTF) and PCM [12].

In order to determine an appropriate PCM for this application, a number of factors must be considered. The most important thermal characteristics of phase change materials are phase change temperature, specific heat and thermal conductivity. Phase change temperature of a desirable PCM should be within the operating temperature range of the thermal storage system. Also the specific heat of a PCM should be high when it is storing heat as sensible, and at last thermal conductivity of the PCM should be high to ensure high heat tranfer rates from the surface to the core of the PCM module in the system. Regin et al. (2008) [27] summarized PCM desirable thermal, physical, chemical and economical characteristics which is given in Table 1.

Table 1- Main desirable characteristics of PCMs [27]

Thermal properties	**Physical properties**	**Chemical properties**	**Economic factors**
▪ Phase change temperature suitable to the desired operating range ▪ High specific heat ▪ High thermal conductivity in both solid and liquid phases	▪ High density ▪ Low density variation during phase change ▪ Little or no supercooling during freezing	▪ Chemical stability ▪ No chemical decomposition ▪ Compatibility with container materials ▪ Non-poisonous, non-inflammable and non-explosive	▪ Available in large quantities ▪ Inexpensive

Although the use of PCMs allow for an increased energy density of thermal storage, challenges remain in the incorporation of PCM into solar water heating systems.

Bjurstron and Carlsson (1985) [13] performed an analysis of the second law of thermodynamics on a well-mixed sensible heat store, a PCM store, and a stratified sensible heat store. The stores are assumed to have a uniform temperature, and the stratified store is assumed to have a sharp boundary between volumes at different temperatures. A schematic of their study is given in Figure 7. They reported that although PCM increases energy density, it did not seem to offer conclusive advantages in efficiency or cost in providing exergy in the store in comparison to the well-mixed sensible heat store. For both these systems, there was an optimum for the exergy fraction stored during the charging period which were fairly equal.

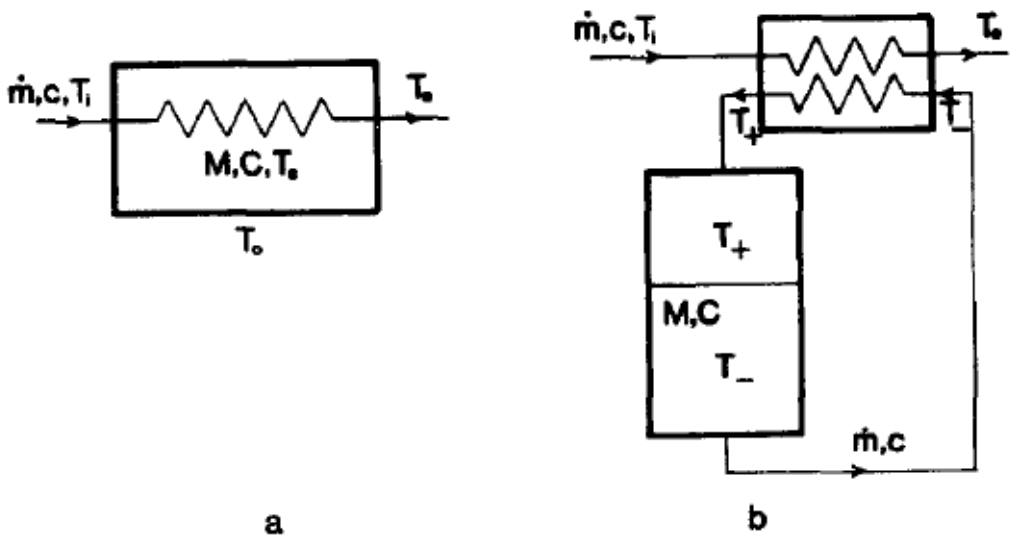

Figure 7-The configuration of (a) the well mixed sensible heat store or the PCM store and (b) the stratified sensible heat store [13]

Talmatsky et al. (2008) [7] computationally investigated the performance of a single tank solar water heating system with and without PCM over the course of a year. Their study showed that although including PCM in the tank decreases the

required stored volume, it does not increase the solar fraction to the end-user or the collector efficiency. They indicate that during the afternoon the water temperature in the tank containing PCM remains at a lower temperature in comparison to a tank without PCM and therefore there is low heat loss to the environment. However during the night time the trend reverses, and the water temperature in the tank containing PCM is higher due to reheating effect of the PCM and that makes the tank lose more heat to the environment. These two effects cancel each other in the period of a day, leaving almost the same solar fraction for both systems. They also pointed out that due to the pre-heating of water by PCM during the night, the collector efficiency drops in the morning in comparison to the system without PCM. That compensates for the higher efficiency of the collector for the system containing PCM during the afternoon when the outlet water remains at a lower temperature.

Kousksou et al. [16] reproduced the results obtained by Talmatsky et al. They also studied the sensitivity of the system behavior to the melting point of the PCM. They pointed out that in one of the systems studied by Talmatsky et al., the PCM melting point is too high, and therefore both water and PCM are storing heat sensibly for almost all the time. By reducing the PCM melting point and keeping every other property of the system unchanged, they were able to increase the reduction of the annual electrical energy backup of the system (by using PCM in the tank) from 7% to 14%. This improvement shows the high sensitivity of the system to the PCM melting point.

The above shows that while the motivation to use PCM is to reduce volume of storage, there seems to be an impact on solar fraction as well.

One of the challenges in using phase change materials is its relatively low thermal conductivity which leads to slow heat transfer from the surface of the PCM to its core. Therefore, a high temperature difference will occur between these two regions and the PCM surface over-heats. This consequently reduces the heat transfer rate from the HTF to the PCM. Therefore, PCMs may require heat transfer enhancement techniques to increase charge and discharge rates [14]. PCMs typically also have lower sensible heat storage capability in comparison to water. Because of the low sensible heat capacity of the PCM, if a large operating range is applied, the gain over sensible energy storage (SES) system becomes less noticeable.

Liu et al. [18] reviewed different techniques used by researchers to enhance the performance of LES systems. These techniques fall into four categories: using high conductive materials to increase the thermal conductivity of the PCM, extending the heat transfer surface of the PCM by using fins and capsules, using intermediate heat transfer medium or heat pipes, and using multiple PCMs.

Multi-PCM systems and heat transfer enhancement techniques are discussed in more detail in the next two sections.

4. Multi-PCM Systems: Motivation and Performance

The idea of using multiple phase change materials in an LES system is motivated by the excellent performance of PCMs within small temperature bands containing the melt temperature. By putting different PCMs in an LES system, researchers have been hoping to extend the advantages of PCMs over a wider operating temperature range. These systems are called cascaded latent energy storage (CLES) systems. In CLES systems the heat transfer fluid exchanges energy with a series of different PCMs starting with higher melting points to lower ones.

Watanabe and Kanzawa [19], showed that by using PCMs with different melting points the charging and discharging rates of a latent heat storage system can be significantly improved, which leads to higher exergy efficiency. They demonstrated that the efficiency of the system is highly dependent on the melting point distribution of the PCMs and that it can be optimized numerically. According to their study, the optimum melting point difference of the PCMs can be achieved when the difference between the water temperature and the melting point of PCMs is almost constant along the fluid flow direction in the system.

Gong and Mujumdar [20] showed that exergy efficiency of a multi-PCM system changes with the number of PCMs, the number of heat transfer units of the storage exchanger, and the inlet HTF temperature, and that they should all be optimized to get the maximum exergy efficiency. They showed that the exergy

efficiency of the system can be doubled or even tripled when using three or five PCMs.

Cui et al. [21] compared the performance of a single-PCM and a three-PCM thermal storage system and concluded that the three-PCM system showed higher heat transfer rates, and less fluctuations in the outlet HTF temperature.

Michels and Pitz-Paal [22] also reported a more uniform outlet temperature in a CLES system. However they pointed out that the low thermal conductivity of the PCMs is an obstacle to full use of this technology.

Seeniraj and Narasimhan [23] used fins to further enhance the heat transfer rate to the PCM in a multi-PCM thermal storage system. They reported significant energy storage in the form of latent heat in comparison to a single PCM model. They also pointed out the uniformity of the HTF exit temperature.

Rady [24] investigated both numerically and experimentally the performance enhancement of an LES system using multiple granular phase change composites (GPCC) with different ranges of melt temperatures in a packed bed. Rady [24] stated that in comparison to a single type of PCM, careful choice of mixing ratios of GPCCs in a composite bed results in a remarkable improvement of the performance of the unit.

Shabgard et al. [25] also reported that their cascaded LES recovered about 10% more exergy during a 24 hour charging-discharging cycle in comparison to the

best single-PCM LES system considered in their work. They reported that their best single-PCM system was the one with the lowest PCM melting point.

In summary, the above findings show that using different types of phase change materials with different melting temperatures has a significant improvement in the overall performance of the system. Specifically, in comparison to a single-PCM system, a multi-PCM thermal storage demonstrates higher charge and discharge rates, higher exergy efficiency, less fluctuations in the outlet HTF temperature, and higher energy stored in the form of latent heat (higher energy density). The factors that should be considered in CLES system improvement is the melting point distribution of PCMs, heat transfer rate to the PCMs and the amount and ratios of the PCMs.

5. PCM Geometry and Heat Transfer Enhancement

Phase change material modules in a hybrid system should be carefully designed to guarantee sufficient heat transfer rates from HTF to PCM and from PCM surface to PCM core. This is especially important because the thermal conductivity of phase change materials is relatively low, and the heat transfer inside the PCM is slow.

Due to PCMs' low thermal conductivity, several techniques have been proposed to increase the heat transfer rate within the PCM. Among the most popular ones are: using finned tubes with different configurations, inserting/dispersing PCM with high conductivity materials, embedding PCM in a metal or graphite matrix

structure, encapsulating PCM in thin aluminium plates, using brushes made of carbon fibers and making a composite based on PCM and a high conductivity material [23]. The goal of these techniques is to increase the effective thermal conductivity in the PCM while maintaining energy storage capacity.

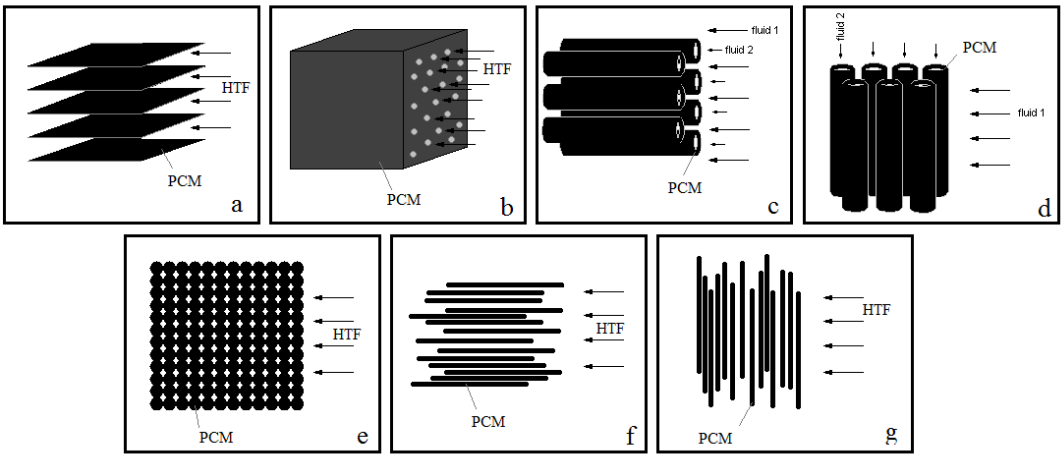

Figure 8-Different PCM geometries used in LES systems: (a) flat plate, (b) shell and tube with internal flow, (c) shell and tube with parallel flow, (d) Shell and tube with cross flow, (e) sphere packed bed, (f) cylinder with parallel flow, (g) cylinder with cross flow.

Another way to ensure high heat transfer rates from the HTF to the PCM is to carefully design PCM geometry, configuration, and volume percentage. Many different encapsulation geometries have been used including: flat plate, shell and tube with internal flow, shell and tube with parallel flow, shell and tube with cross flow, sphere packed bed, cylinder with parallel flow, cylinder with cross flow [27], as shown in Figure 8.

Esen et al. (1998) [28] numerically studied the diurnal transit behavior of a hybrid LES system with two different PCM geometries: cylinder with parallel flow, and

shell and tube with internal flow. These are shown in Figure 9. They studied the effect of various parameters such as cylinder radii, pipe radii, PCM volume percentage, HTF inlet mass flow rate, HTF inlet temperature. They concluded that for the same PCM percentage the charge time for the second configuration (shell and tube with internal flow) is much shorter than that of the cylindrical configuration, and this was basically due to higher PCM module thickness for the cylindrical configuration. The charge time varies almost linearly with PCM volume percentage. Higher HTF inlet flow rates also reduce charge time, although the PCM configuration inside the tank is much more influential in determining the charge time. They also showed that charge time reduces by increasing HTF inlet temperature, reducing PCM module and pipe radii.

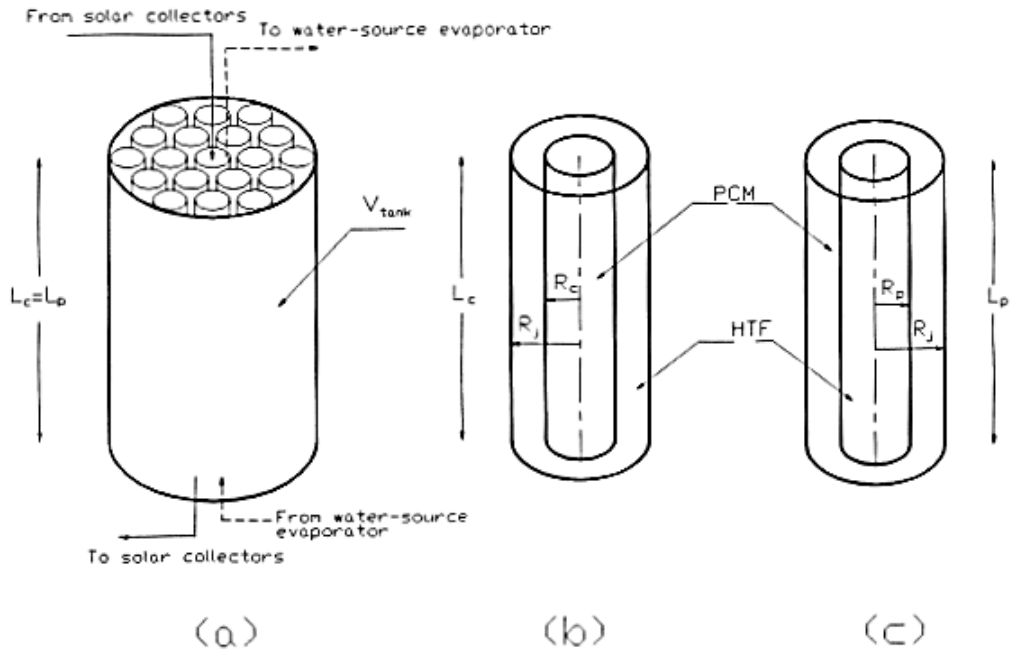

Figure 9- Latent heat energy storage tank with (a) cylinders or pipes, (b) cylinder model and (c) pipe model [28].

Wei et al. (2005) [15] encapsulated PCMs in four different geometries (sphere packed bed, cylinder with cross flow, flat plate and shell and tube with internal flow) as shown in Figure 10 to study the effects of capsule diameter (2, 3, 4 and 5 mm), shell thickness (0.2 and 0.4 mm) and void fractions (0.25 and 0.5) on the performance of an LES systems. They reported that for the same PCM volume percentage and capsule diameter, the heat release performance decreased in the order of sphere, cylinder, flat plate, and shell and tube, with the shell and tube with low void fraction showing the poorest performance. This is mainly due to reduced surface area of the encapsulation geometry. They also found that the discharge time decreases almost linearly when decreasing PCM diameter. For the same PCM diameter, the heat release performance was almost independent of void fraction for spherical and cylindrical capsules, while in the flat plate and shell and tube geometry, the heat release rate decreased with a decrease in void fraction. This is due to the fact that for flat plate capsules with low void fraction, the boundary layers interact with each other, while for the shell and tube configuration, lower void fraction associates with higher PCM thickness.

Esmail and Moraes (2009) [29] studied the variations in the solidification time of different phase change materials, in spherical and cylindrical shells with different diameters subject to a constant surface temperature. They reported that increasing the diameter of the spherical shell resulted in an increase in complete solidification time which is mainly due to more PCM material. They also observed, up to a specific diameter, the increase was relatively small, and the

dominant mode of heat transfer was conduction, however at a diameter of approximately 0.076 m convection in the liquid region moves the melt away from the solidifying front and delays complete solidification.

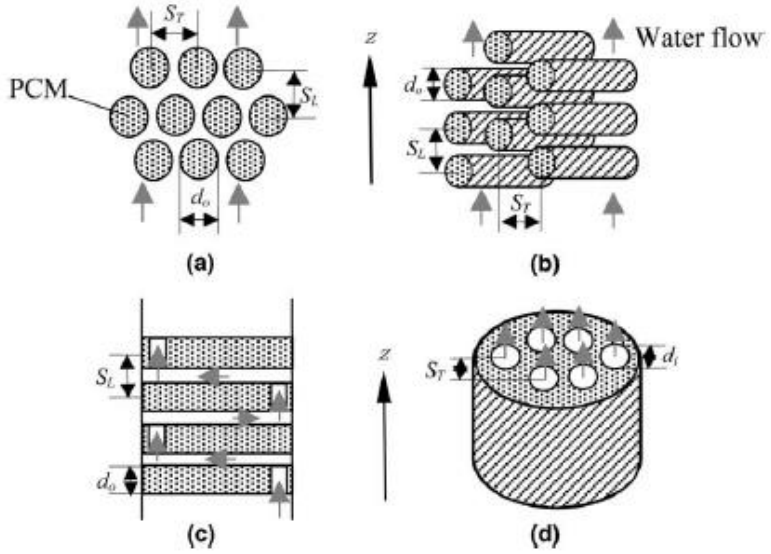

Figure 10-Arrangement of PCM in the heat storage tank of Wei et al. [15] work. (a) Sphere, (b) cylinder, (c) plate and (d) tube

Agyenim et al. [14] reviewed the studies performed on thermal performance evaluation of LES systems and emphasized the need for a unified platform to allow comparison and use of the knowledge gained from one test to the other. They indicated that although there are many studies conducted on these systems, they generally did not present their results in dimensionless numbers which made it almost impossible to compare different studies. Furtheremore the researchers who non-dimensionalised their data, it was seen that the PCM employed varied again making it difficult to cross-correlate the data. Some researchers developed correlations for thermal performance parameters such as melted volume fraction,

temperature profile, melt time, and melting rate. Agyenim et al. [14] pointed out that there are variations between correlations derived, which is mainly due to different methods of analysis and the choice of characteristic lengths. They also added that LES systems were first assumed to be conduction controlled, however recently natural convection in the fluid phase of the PCM has been included in the calculations which makes the analysis even more complicated. Table 2 shows different dimensionless numbers that are used to analyze the performance of LES systems.

6. LES Modeling and Performance Evaluation Methods

Verma et al. [36] reviewed mathematical modeling of latent heat thermal storage systems for optimum material selection and system performance optimization. They divided the mathematical modeling into two different categories: models based on the first law of thermodynamics, and models based on the second law of thermodynamics. They reported that most of the studies worked on the first law of thermodynamics. They stated that the second law (exergy analysis) is a good method in understanding the behavior or efficiency of the system, in contrast to the first law that does not take into account the charge or discharge duration.

In modeling heat transfer in PCM-based thermal storage systems, different modeling approaches have been adopted. Zalba et al. (2003) [1] reviewed different modeling approaches and divided them into four categories: moving boundary problems, numerical solution considering only conduction, numerical

solution considering also convection, and numerical solution in different heat exchanger geometries. The moving boundary problem models phase change in the PCM where the boundary between solid and liquid phases moves depending on the heat transfer rate at the boundary.

Table 2-Dimensionless numbers used to analyze the performance of LES systems [14].

Number	**Source**	**Formula**	**Significance (determination)**
Biot, *Bi*	[30]	$Bi = \frac{hl}{k}$	Ratio of conductive to convective heat transfers resistance. Determines uniformity of temperature in solid.
Nusselt, *Nu*	[31],[32]	$Nu = \frac{hd}{k}$	Ratio of the conductive thermal resistance to convective thermal resistance. Determines the actual heat transferred by a moving fluid to the heat transfer that would occur by conduction.
Stefan, *Ste*	[33]	$Ste = \frac{c_{p,l}\Delta T}{\lambda}$	Ratio of thermal capacity of the melted solid to the latent heat. Characterises heat flux into a body or system.
Dimensionless time or Fourier number, *Fo*	[31]	$\tau = \frac{kt}{\rho c_p l^2}$	
Rayleigh, Ra	[32]	$Ra = \frac{g\beta\Delta T l^3}{\alpha \upsilon}$	Determines the onset of convection. Below a critical value, heat transfer is primarily conduction.
Prandtl, Pr	[32]	$Pr = \frac{\nu}{\alpha}$	Approximates the ratio of momentum diffusivity to thermal diffusivity. Low Pr means effective heat convection with dominant momentum diffusivity.
Reynolds number, Re	[34]	$Re = \rho \frac{\upsilon D}{\mu}$	Ratio of inertial forces to viscous forces. Determines whether flow is laminar or turbulent.
Grashof number, *Gr*	[35]	$Gr = \frac{g\beta\Delta T l^3}{\upsilon^2}$	Approximates the ratio of buoyancy force to the viscous force.

Many of the early studies that modeled phase change only considered heat transfer through conduction. However, when some researchers performed experimental studies, it was seen that the modeling solutions were not in good agreement with the experimental data and natural convection in the liquid phase of the PCM has an important role in the heat transfer characteristics of the system [1]. Zalba et al. [1] reported that because of the complexity of equations and geometries the only generally applicable mathematical approach is that of numerical methods.

Al-abidi et al. [37] reviewed studies on numerical modeling of phase change materials in spherical, flat plate and cylindrical geometries through a commercial computational fluid dynamics (CFD) software or self-developed numerical model for programming in LES systems. They reported that: (1) The numerical solution of the PCM thermal behavior is more accurate than the analytical solution; (2) The numerical results of the 2D modeling are generally the same as those of 3D, which can reduce time and cost of the simulations. (3) Use of CFD analysis in designing LES systems is feasible since the results are highly accurate.

Rundle [54] validated ANSYS CFX for simulation of the heat transfer and fluid flow in atria geometries. The validations were performed for both laminar and turbulent natural convection flows, and reported that the simulations of laminar natural convection were in excellent agreement with the experimental data. For simulations of turbulent natural convection, Rundle used three different two-

equation turbulence models: $k-\varepsilon$, $k-\omega$, and SST. He reported that among these, the $k-\varepsilon$ model showed the worst results with very high errors. However the $k-\omega$ model and the SST model produced results in close agreement with the experimental data. More specifically, the $k-\omega$ model better predicted the velocity profiles in the boundary layers while the SST model better predicted the average Nusselt number. It was also reported that convergence was harder achieved when the SST model was used. Rundle [54] also investigated the effect of the addition of the buoyancy turbulence production term in the second equation of the models and concluded that it did not show any significant improvement in the prediction of the simulation results.

In summary, there are many analytical and numerical techniques in modeling heat transfer in an LES system most of which have complex geometries and complicated formulation. Due to these complexities numerical methods are reported to be more practical and accurate. In this study, we will be using CFD in modelling the heat transfer at the water side of the system. The assumptions made and the modeling approach are given in Chapter 4.

7. Summary

A number of different types of multi-tank systems have been proposed in the literature. The multi-tank system by Mather et al. [6] showed enhanced behavior during both charging and discharging as a result of the thermal diode effect, and

best maintained stratification between tanks in comparison to other multi-tank systems. It is also economical since pressurized tanks are not required.

Reviewing the literature on PCM-based tanks, it has been shown that using phase change materials in thermal storage tanks, helps increase energy density, reduce temperature fluctuations, and increase charge rate. However, PCMs usually have low thermal conductivity and sensible heat capacity and therefore need heat transfer enhancement techniques, and careful system designs.

The literature on multi-PCM systems reported promising performance enhancement of thermal storage systems. It was concluded that using several types of PCMs in a TES system, significantly increases exergy efficiency, reduces temperature fluctuations at the outlet, increases energy density, and shows higher charge and discharge rates.

A survey on different PCM encapsulation geometries showed that PCM configuration inside the tank can significantly influence the charge time. Generally, for the same PCM volume percentage, the charge time can be reduced by increasing the surface area of the PCM, and decreasing the PCM thickness. However, increasing PCM surface area is associated with increase in PCM encapsulation costs. Therefore, choosing PCM encapsulation is a trade-off between cost and performance.

Significant research has been performed on different techniques to improve thermal storage systems. However, there is a gap in the literature for multi-tank

systems that contain PCMs. Using phase change materials in multi-tank systems can reduce the total volume of the system. Incorporating multiple PCMs in a multi-tank system is especially interesting as each tank operates in a smaller temperature range in comparison to the whole TES system. This small operating temperature range in each tank helps take advantage of phase change materials' high specific enthalpy. This motivation is discussed further in Chapter 3.

CHAPTER 3 ‘Tuned’ Multi-Tank Hybrid Water-PCM Thermal Storage

1. Introduction

Phase change materials generally have exceptional energy storage capacity during phase change, but relatively poor sensible heat capacity in comparison to other energy storage media such as water. As such, there is motivation to exploit the latent heat capacity of the PCM while minimizing the use of PCM for sensible storage. In order to achieve this, the operating temperature range that the PCM is exposed to would ideally be restricted to a narrow band that includes the melt temperature. The benefit of a reduced operating temperature range is illustrated in Figure 11 which shows the theoretical energy storage per unit mass of water and

lauric acid (a typical phase change material) versus temperature for two different ranges of 40 degrees and 10 degrees. The gain in energy stored in PCM in comparison to that of water for the two temperature ranges is respectively 70% and 450%. The physical properties of lauric acid and water are given in Table 3.

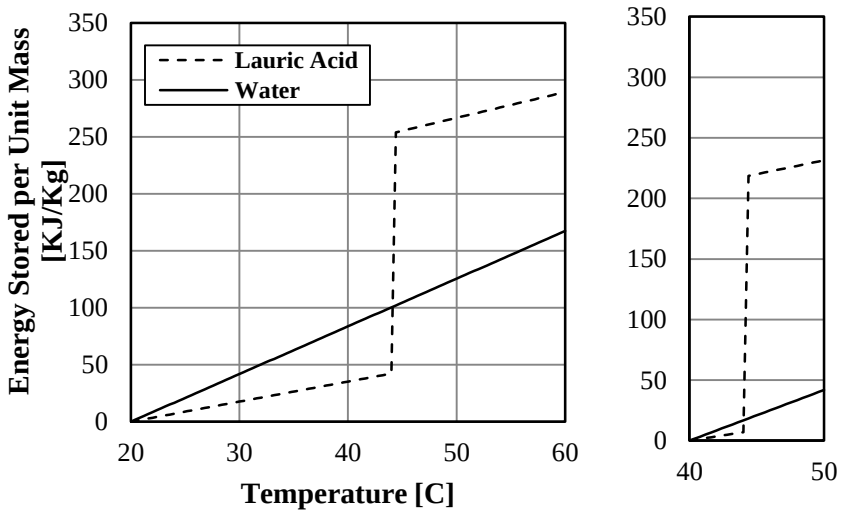

Figure 11-Energy stored per unit mass of water and lauric acid versus temperature

Table 3- Physical properties of Lauric acid and water [53]

Property	**Value**
Lauric Acid:	
Density, ρ	1007 kg/m^3
Specific heat of solid phase, C_s	1760 $J/kg.K$
Specific heat of liquid phase, C_l	2270 $J/kg.K$
Heat of fusion, H_{fg}	211.6 kJ/kg
Melting temperature, T_m	44.2 ℃
Water at 20℃:	
Density, ρ	1000 kg/m^3
Specific heat of water, C_w	4186 $J/kg.K$

This narrow operating temperature range restriction is, however, incompatible with the practical needs of most solar energy systems. A potential solution to this is to employ a multi-tank system, similar to that proposed by Mather et al (2002) [6], where PCMs with a range of melt temperatures are incorporated into the tanks. With this approach, the temperature of each tank could be controlled or 'tuned' in such a way as to ensure that the operating temperature range of a single tank is limited to a narrow band containing the melt temperature of the particular PCM contained in that tank. This would also act to enhance stratification between the tanks. The first step in the development of a 'tuned' multi-tank hybrid water-PCM thermal storage concept is to explore the energy storage characteristics of a single water tank with embedded PCM modules. That exploration is the focus of the current chapter.

2. Thermal Capacity of the System

Consider a hybrid tank that is being charged from an initial temperature ($T_{initial}$) to a final temperature (T_{final}), which is the coil temperature in the tank. The total accumulated energy (E_{tot}) in the hybrid system can be calculated using the following equation:

$$E_{tot,PCM} = M_w C_w (T_w - T_i) + M_{PCM} C_{PCM,s} (T_m - T_i) + M_{PCM} H_{fg,PCM} + M_{PCM} C_{PCM,l} (T_{PCM} - T_m) \quad (1)$$

A similar equation can be used for the case with no PCM (water only) installed in the system:

$$E_{tot,No\ PCM} = M_w C_w (T_w - T_i) \quad (2)$$

where, $H_{fg,PCM}$ is the latent heat of fusion of the PCM, while $C_{PCM,s}$ and $C_{PCM,l}$ are the specific heat capacities of solid and liquid PCM, respectively. At steady state, the final temperatures of the water and PCM in both cases reach the coil temperature. The gain of installing PCM in the storage system can be realized by dividing equations (1) and (2):

$$\text{Thermal Storage Gain} = \frac{E_{tot,PCM}}{E_{tot,No\ PCM}}$$

$$= 1 + \varphi \left[\frac{\rho_{PCM}}{\rho_w}\right]\left[\frac{H_{fg,PCM}}{C_w \Delta T_o}\right]$$

$$- \varphi \left[1 - \frac{0.5\left(C_{PCM,s} + C_{PCM,l}\right)}{C_w}\frac{\rho_{PCM}}{\rho_w}\right] \quad (3)$$

In equation 3, $\varphi = V_{PCM}/V_{tank}$ is the volume fraction of PCM and $\Delta T_o = T_{final} - T_{initial}$. The second term in the right hand side of equation (3) shows the benefit of using PCM in the storage system due to PCM's high heat of fusion, whereas the third term shows the penalty that could arise if the specific heat capacity of the PCM is lower than that of water. Figure 12 shows the effect of varying the volume fraction of the PCM and the operation temperature range on the gain.

This figure shows that the higher the volume fraction of the PCM, the higher the storage gain of the system compared to that with no PCM. Furthermore, it is shown that the lower the operating temperature range, the higher the storage gain. This means that both the coil temperature and the initial temperature of the system should be controlled within a narrow range around the melting temperature of the PCM to achieve the maximum gain.

Figure 12 can be used as a design tool. For example if we want to reduce the volume of our system by a factor of two, or increase the thermal capacity of the system to twice its value, we can use 25% lauric acid in the tank, in which we control the operating temperature range to be no more than around 11℃, or we can use 50% lauric acid in a tank that we control the operating temperature range to be no more than 20℃.

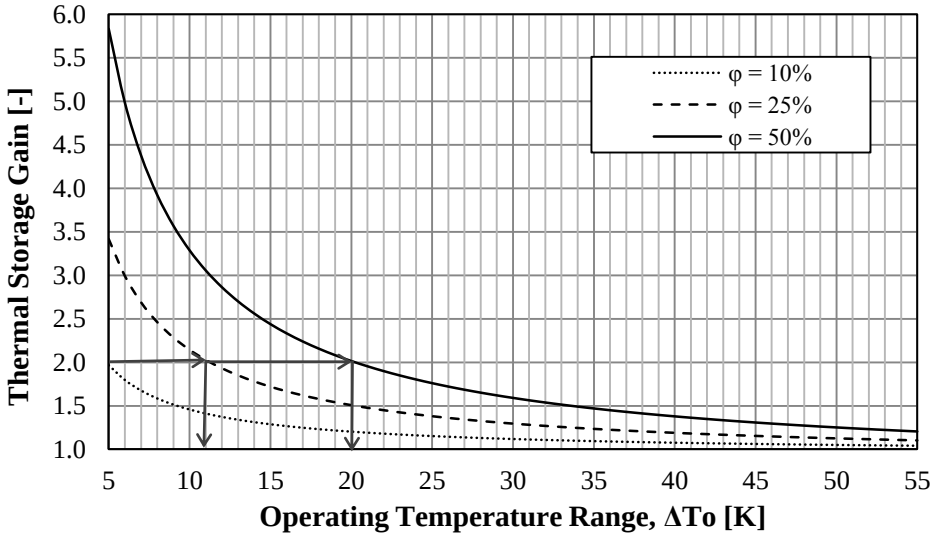

Figure 12-Thermal storage capacity gain of a hybrid system over a sensible storage system versus operating temperature range.

Figure 12 provides information on the thermal capacity of the system only, but does not provide information on how long it will take such systems to charge completely. As such, it is valuable to study the transient behavior of the system during charging. Therefore, a preliminary numerical model was formulated and solved to assess the important parameters that affect the heat transfer rates to the system.

3. Transient Behavior of the System

A numerical lumped capacitance model has been devised to solve the transient energy equation for the storage system under study. Figure 13 shows a schematic for the modeled system. This model encompasses the following assumptions:

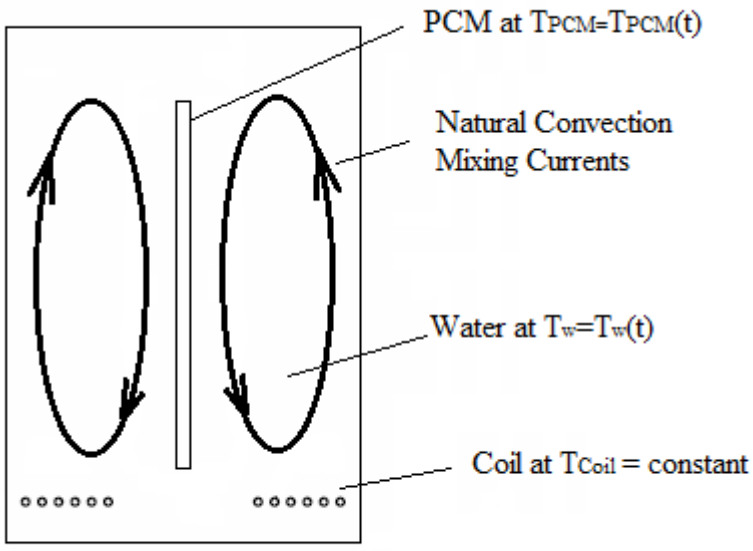

Figure 13-Schematic for the modeled system

a. The storage tank is considered as a lumped system. It is assumed that the natural convection mixing driven by the charging coil placed in the bottom of the tank is fast enough to maintain spatially homogeneous temperature inside the tank; i.e. $T_w = T_w(t)$ only. This assumption relies on the capability of the designed system to promote natural convection mixing inside the tank as in Mather [6].

b. The spatial temperature variation inside the PCM modules is assumed to be negligible. Therefore, the temperature of the PCM is only a function of time. This assumption could be valid if the Biot number of the PCM module is very small, Bi~0.1. This can be achieved by using very slender modules.

c. The PCM has a fixed melting temperature.

d. The charging coil temperature is assumed constant throughout the charging process.

e. The heat transfer coefficient between the coil and water is assumed to be constant.

f. The heat transfer coefficient between the water and PCM module is assumed constant.

g. The system is assumed to be perfectly insulated.

3.1. Mathematical Formulation

Energy Balance on Water:

For $T_{PCM} < T_m$, or $T_{PCM} > T_m$

$$(MC)_w \frac{dT_w}{dt} = (hA)_{coil} (T_{coil} - T_w) - (hA)_{PCM} (T_w - T_{PCM})$$

$$\frac{dT_w}{dt} = \left(\frac{1}{\tau}\right)_{coil} (T_{coil} - T_w) - \left(\frac{1}{\tau}\right)_{PCM} (T_w - T_{PCM}) \qquad (4-a)$$

For $T_{PCM} = T_m$

$$\frac{dT_w}{dt} = \left(\frac{1}{\tau}\right)_{coil} (T_{coil} - T_w) - \left(\frac{1}{\tau}\right)_{PCM} (T_w - T_m) \qquad (4-b)$$

Where, $\tau_{coil} = \frac{(MC)_w}{(hA)_{coil}}$ which represents the time constant of the water in reaction to gaining heat from the coil and $\tau_{PCM} = \frac{(MC)_w}{(hA)_{PCM}}$ which represents the time constant of water in reaction to heat transfer to the PCM. T_m is the PCM melt temperature.

Energy Balance on PCM Module:

For $T_{PCM} < T_m$, or $T_{PCM} > T_m$

$$(MC)_{PCM} \frac{dT_{PCM}}{dt} = (hA)_{PCM} (T_w - T_{PCM})$$

$$\frac{dT_{PCM}}{dt} = \left(\frac{1}{\tau}\right)_{PCM} (T_w - T_{PCM}) \qquad (5-a)$$

For $T_{PCM} = T_m$

$$\frac{dT_{PCM}}{dt} = 0.0 \qquad (5-b)$$

$$H_{fg}\frac{dM_{PCM-melt}}{dt} = (hA)_{PCM}(T_w - T_{PCM}) \qquad (5-c)$$

where H_{fg} is the heat of fusion of the PCM and $M_{PCM-melt}$ is the mass of melted PCM. A FORTRAN code has been implemented to solve equations (4) and (5) explicitly in time using a simple Euler method. The initial temperatures (T_i) for the water and the PCM and the coil temperature (T_{coil}) were set as inputs. The operating temperature range ($\Delta T_o = T_{coil} - T_i$) of the system was chosen in such a way that the melting temperature of the PCM, $T_m = \frac{T_{coil}+T_i}{2}$.

The discretized forms of equations (4) and (5) are as follows:

$$T_w = T_w^0 + \frac{\Delta t}{\tau_{coil}}\left\{(T_{coil} - T_w^0) + \frac{(hA)_{PCM}}{(hA)_{coil}}(T_{PCM}^0 - T_w^0)\right\} \qquad (6)$$

$$T_{PCM} = T_{PCM}^0 + \frac{\Delta t}{\tau_{PCM}}(T_w^0 - T_{PCM}^0) \qquad (7)$$

Where, Δt is the time step, while T_w^0 and T_{PCM}^0 are the values of the water and PCM temperature at the previous time step, respectively.

The code was designed in a way that when the temperature of the PCM reaches its melting temperature, the temperature is maintained at the melt temperature and the energy absorbed by the PCM causes it to melt and then the melt fraction is

calculated. Furthermore, when the melt fraction reaches 100%, the code allows the PCM temperature to rise again with heating. The code also solved the problem when the storage tank contains only water with no PCM included to illuminate the merits behind employing PCMs in the storage system.

At the end of the computations, the code provides the following:

a. Time history of the water and PCM temperatures.
b. Time history of the accumulated energy stored in water and PCM.
c. Time history of the total accumulated energy stored in the system.
d. Time history of the total accumulated energy stored in the system with no PCM.

3.2. Results and Discussion

The code was executed using time step of 10 seconds and simulation time of 8 hours. This simulation time has been chosen because it is common in solar energy storage applications. Also tests were performed to ensure time step independence. Two cases have been tested with the same volume fraction (φ = 25 %) but different $(hA)_{PCM}$ of 120 and 1200 W/K to investigate the sensitivity of the performance of the storage system to the natural convection heat transfer coefficient of the water and the surface area for the PCM modules. The values of coil and PCM heat transfer coefficients are calculated through experimental correlations for natural convection of fixed temperature horizontal cylinders and

vertical flat plates, respectively in an infinite environment. The initial water temperature and coil temperature where 40℃ and 50℃ respectively.

Figure 14 shows the effect of $(hA)_{PCM}$ on the temperature history of the PCM module during the charging period. This figure indicates that the increase of the value of $(hA)_{PCM}$ leads to modestly earlier melting of the PCM. The PCM for the case with higher $(hA)_{PCM}$ started melting after 3190 s, while the one with lower $(hA)_{PCM}$ started melting after 3300 s. Furthermore, higher $(hA)_{PCM}$ leads to higher melting rate. The figure shows that the PCM for the case with the higher $(hA)_{PCM}$ melting was completed after about 20230 s, while the data showed that the one with lower $(hA)_{PCM}$ was left with ~27% un-melted PCM after the charging time ended. As a result higher energy storage was found from the system with higher $(hA)_{PCM}$ at the end of the charge period because this will allow for better utilization of the latent heat capacity of the PCM.

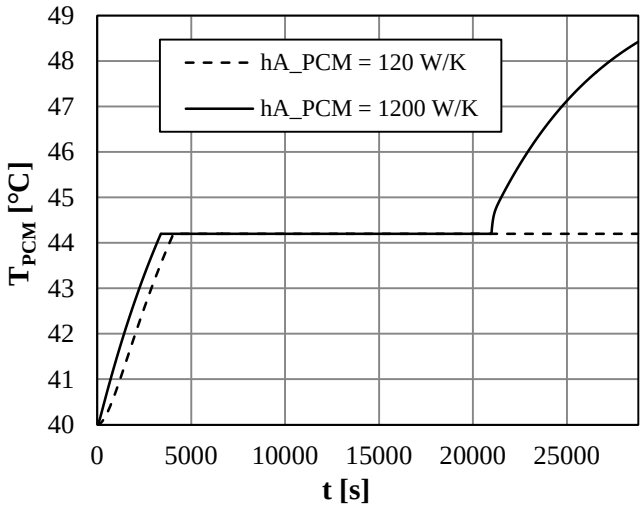

Figure 14-Charging history of PCM temperature for $(hA)_{PCM}$ = 120 and 1200 W/K

The water temperature history plays a vital role in controlling the thermal performance of the storage system, acting as the buffer zone between the charging flow and the PCM module. Figure 15 shows that for the case with higher $(hA)_{PCM}$ $(1200\ W/K)$, the water temperature levels off 1570 s after PCM melting commences which is much sooner that the one with lower $(hA)_{PCM}$, where the water temperature becomes steady 8330 s after PCM melting starts. Also in the case with higher $(hA)_{PCM}$ the average temperature of water is lower than the case with lower $(hA)_{PCM}$. These observations emphasize the crucial role of employing PCM in the storage system. That is, the water temperature is maintained at a constant value during the charging process. This results in constant temperatures in the tanks which promotes effective stratification in series multi-tank storage systems.

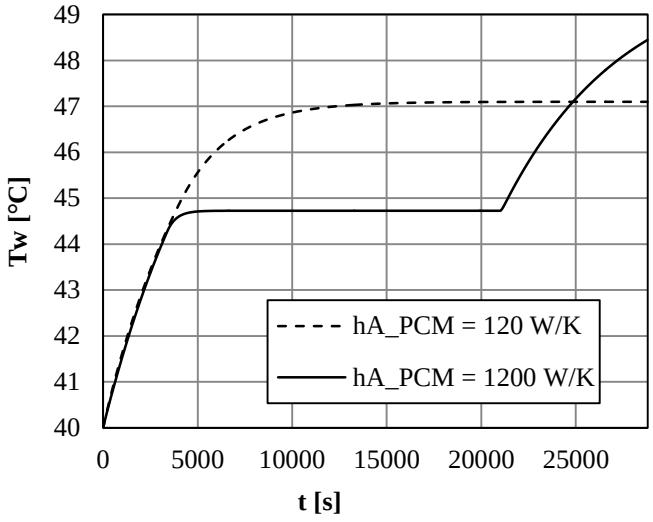

Figure 15-Charging history of water for $(hA)_{PCM}$ = 120 and 1200 W/K

In terms of the transient energy content of the tank during the charging period, Figure 16 shows that increased energy storage is associated with the system with the higher $(hA)_{PCM}$. It is shown that one order of magnitude increase in $(hA)_{PCM}$ leads to 33.7 % increase in the total amount of energy stored for the conditions considered. This is because the lower average water temperature associated with the higher $(hA)_{PCM}$ increases the rate of heat transfer from the coil to the storage medium.

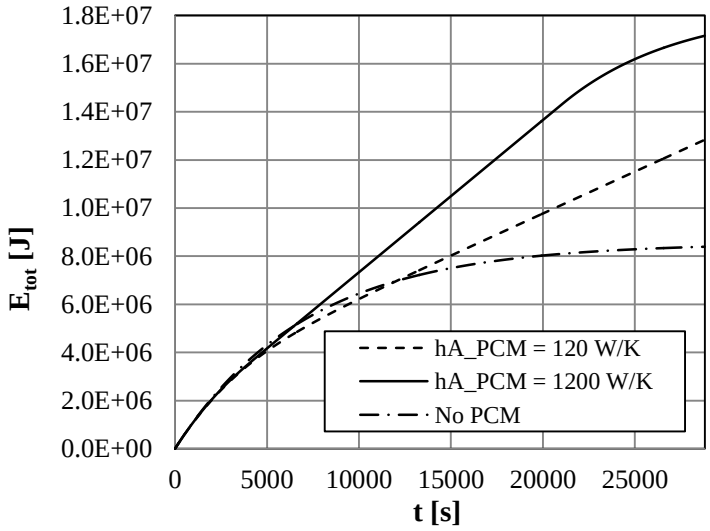

Figure 16-Charging history of total energy stored (E_{tot}) in the tank for $(hA)_{PCM}$ = 120 and 1200 W/K

In support of the hypothesis behind the current study, Figure 16 also shows a comparison between the total energy stored in the hybrid storage system and that in the water storage system with no PCM. The figure illustrates that for the same charging period, the hybrid system employing the PCM in the storage tank is characterized by higher storage capacity when compared to the system that uses water only in the tank. A storage gain of 53% can be achieved when $(hA)_{PCM}$ =

120 W/K, while a gain of 103 % can be achieved when $(hA)_{PCM}$ = 1200 W/K for the charging period considered. In the $(hA)_{PCM}$ = 1200 W/K case the energy stored in the tank is more than two times that of a water only tank, which was expected for 25% Lauric acid with 10℃ working temperature in Figure 12.

4. Summary

The lumped capacitance model showed that the system under consideration is highly sensitive to the heat transfer coefficient and the surface area of the PCM. The higher it is, the higher the charge rate of the system. In this study the values for $(hA)_{Coil}$ and $(hA)_{PCM}$ are calculated through experimental correlations for natural convection of fixed temperature horizontal cylinders and vertical flat plates, respectively in an infinite environment. It is expected, however, that the actual conditions are far from the ideal conditions for which the correlations apply. The closeness of the coil tubes and PCM modules in the tank especially for high PCM volume percentages, as well as the interaction of the upward flow from the coil with the downward flow from the PCM modules, is expected to influence the heat transfer coefficients of coil to water and water to the PCM modules.

In order to estimate realistic values of hA for both PCM and the coil, the flow field and its heat transfer characteristics must be explored in greater detail. Computational fluid dynamics (CFD) can be used as a tool to attain this information. The factors that may influence the heat transfer characteristics of the

flow include: encapsulation geometry, PCM module placement within the tank, PCM volume percentage and PCM surface area.

The study presented hereafter is focused on the prediction of heat transfer to the PCM and the coil from the natural circulation of water, and concentrates on the processes that lead to high heat transfer rates to the PCM surface. Future works will consider heat transfer processes within the PCM module.

The commercial CFD code ANSYS CFX 14.0 is used to simulate the heat transfer and fluid flow in a tank containing PCM capsules of different volumes and placements. The goal of the research is to determine the module configuration, surface area and PCM volume percentages that provide highest heat transfer rates during the melting phase of the process. The heat transfer coefficients predicted from the CFD simulations can then be used to create a multi-tank model which will allow for exploration of the tuned storage concept.

CHAPTER 4 Validation and Modeling Approach

This chapter presents an overview of CFD validations, the PCM module geometries considered in this work and the methodology for modeling the heat transfer and fluid flow in the hybrid tanks.

1. CFD Validation for Natural Convection

This section provides a summary of the validation studies that were performed in order to establish confidence by comparing CFD predictions with their corresponding experimental correlations established in past literature. The studies

focused on natural convection for both laminar and turbulent flow conditions. For all simulations care was taken to ensure that results are grid independent. Details of the validation studies are provided in Appendix A.

The first set of validation studies was performed for natural convection in a square air cavity for both laminar and turbulent flows. The motivation behind this study was to assess the accuracy of CFD modeling for natural convection flow in a closed system. The results of the simulation were then compared to the benchmark data available in the literature. It was found out that for laminar flows, CFD was excellently able to predict different features of the flow with errors in Nusselt number predictions were less than 0.05%. For turbulent flow, as Rundle [54] reported, the $k-\omega$ model showed better predictions of the velocity profiles in the boundary layer region, while the SST model better predicted the average Nusselt number. In this validation case the standard $k-\omega$ turbulence model was applied. The $k-\omega$ model predicted the flow fairly well. The temperatures and the Nusselt number were under-predicted. The Nusselt numbers were under-predicted by about 17%.

The second set of validation studies were performed for natural convection around a cooled vertical flat plate in an infinite environment for both laminar and turbulent flows. The Nusselt numbers and velocity profiles from the simulation were then compared to those given by experimental correlations available in the literature. This set of validations was performed to assess the accuracy of CFD predictions for fixed temperature vertical flat plates which would be useful later

on to evaluate thermal characteristics of PCM modules of the same length. In this case CFD was successful in predicting the velocity and temperature profiles. The Nusselt number of the plate was also predicted with less than 0.07% error. However, for the turbulent flow, it was concluded that since the flow considered in this study is somewhat transitional, the experimental correlations introduce a wide range of values. The SST model also under predicted the evaluated Nusselt number. The Nusselt number was under-predicted by 22%.

The last validation study was performed for a heated horizontal cylinder in an infinite environment for laminar flow, and the Nusselt number from the simulation was then compared with the experimental correlations available in the literature. This validation was performed to assess the accuracy of the CFD commercial code for laminar flow around a fixed temperature horizontal cylinder which would be used later on to evaluate thermal characteristics of coil tubes of the same diameter in the tank. Note that this validation is only performed for laminar flow because the calculated Rayleigh number for the coil was in the laminar region. The Nusselt number predicted by the simulation was in 1% of the Nusselt numbers calculated from the experimental correlations.

2. Geometry for Hybrid PCM tank

As discussed in the previous chapters, the geometry used in this research is inspired by the work presented by Mather et al. [6], who used 200 litre cylindrical tanks with a diameter of 0.58 m and a height of 0.77 m.

For simplicity and computational economy, the flow was modelled as two dimensional. The dimensions of the three dimensional cylindrical tank studied by

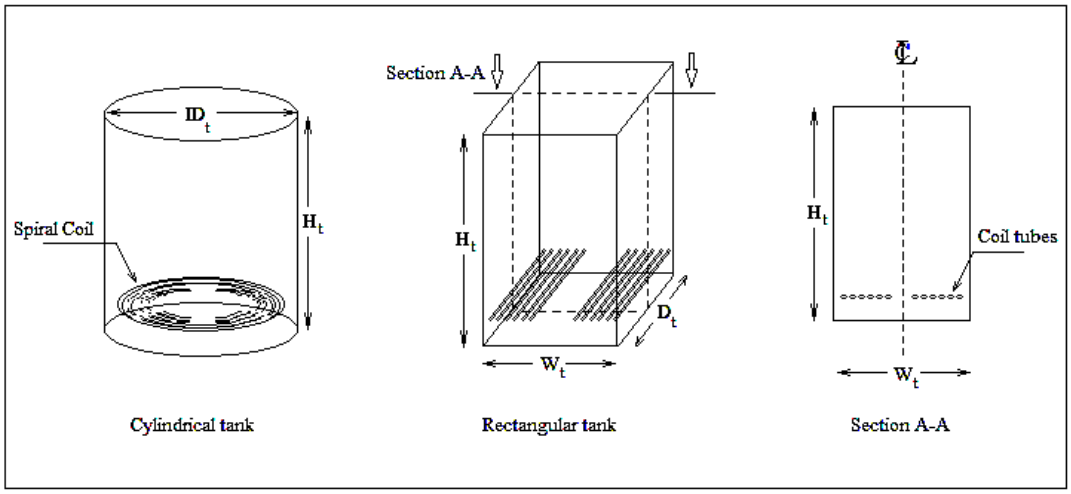

Figure 17-Transformation of the cylindrical tank to a rectangular tank and the vertical cross section under study

Table 4- Dimensions of the tank and coil used in Mather's [6] study

Parameter	**Value**
V_t, tank volume	0.2034 m^3
ID_t, tank inner diameter	0.58 m
H_t, water height in the tank	0.77 m
L_c, coil length	5.98 m
OD_c, coil outer diameter	0.0127 m
d_s, surface to surface coil spacing	0.012 m
W_v, gap between coil and the bottom of the tank	0.06 m

Mather et al. [6] was transformed to a square based rectangular tank of the same volume and height. The surface area of the coil is also maintained between the tanks and the centerline vertical cross section of the tank is modeled. The transformation of the tank geometry and the section under study is shown in Figure 17.

The dimensions of the cylindrical tank and coil used in Mather's study (shown in Figure 17) are given in Table 4.

The volume of Mather's tank is $V_t = H_t \times \pi \times {ID_t}^2/4 = 0.2034\ m^3$. A rectangular tank of the same volume and height with square horizontal cross sectional area has a width of $W_t = \sqrt{V_t/H_t} = 0.5140$ m. The surface area of the coil used is $A_c = L_c * \pi * OD_c = 0.2386\ m^2$. Using the same coil surface area in the rectangular tank, in the shape of parallel tubes, the perimeter of the coil in the vertical cross section of the tank will be $A_c/W_t = 0.4642$ m. This perimeter consists of $0.4642/\pi \times OD_c = 11.63$ tubes in a vertical cross section. If we use 12 tubes in the vertical cross section (which is also the case in Mather's spiral coil if we make a section from the center), the depth of the rectangular tank can be recalculated $D_t = A_c/12 \times \pi \times OD_c = 0.4984$ m. Now, having the same horizontal cross sectional area as of Mather's, our rectangular tank should have a width of $W_t = V_t/(H_t \times D_t) = 0.53$ m.

Table 5- Dimensions of the rectangular tank and coil in this study

Parameter	**Value**
V_t, tank volume	$0.2034\ m^3$
H_t, tank height	0.77 m
W_t, tank width	0.53 m
D_t, tank depth	0.5 m
N, number of horizontal tubes (coils) in a vertical section	12
S_c, coil spacing	0.012 m
H_{PCM}, PCM module height	0.55 m
W_{PCM}, PCM module width	0.02 *m*

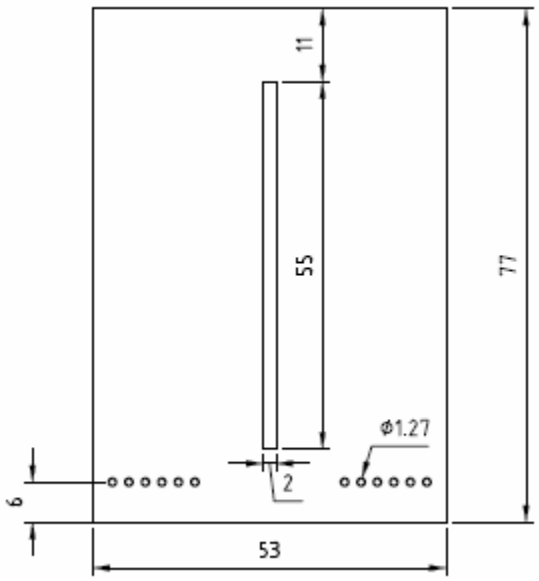

Figure 18-The dimensions (in centimeters) of the simulated model for 2.5% PCM in the tank

Table 6-PCM volume percentages studied and their corresponding number of PCM modules

Number of plates in the tank	***Number of plates in the simulation model***	***PCM volume percentage (actual value)***	***PCM volume percentage (nominal value)***
1	*0.5*	2.7%	2.5%
2	*1*	5.4%	5%
4	*2*	10.8%	10%
6	*3*	16.2%	15%
8	*4*	21.6%	20%
10	*5*	27.0%	25%
12	*6*	32.3%	30%
14	*7*	37.7%	35%

The PCM modules were chosen to have rectangular flat plate geometry of finite width. This shape was chosen since it allows for a large surface area per unit volume and a reduced internal resistance to heat transfer within the PCM (small

characteristic length). Allocating a 5 cm vertical gap between the plates and the charge coil in order to minimize the interference of the upward flow from the coil and the downward flow from the PCM, the final height of the plates will be 55 cm. Also after a survey of studies on different PCM module sizes and thicknesses the width of the modules is chosen to be 2 cm. The two dimensional model is assumed to be symmetric, and therefore the right half of the tank is simulated only. The dimensions of the final rectangular tank of the same volume, height and coil surface area given in Table 5. The geometry of the two dimensional model is also shown in Figure 18.

The PCM volume percentage of one PCM module in the tank is $(H_{PCM} \times W_{PCM})/(H_t \times W_t) = 2.7\%$ (nominally 2.5%). In this research, eight different PCM volume percentages were studied ranging from about 2.5% to 35% of the tank volume. The PCM volume percentages studied and their corresponding number of PCM modules is given in Table 6.

3. Grid

The grid used for the simulations was structured in the vicinity of the plates while a non-structured grid was employed near the coils similar to the grid arranged in the validation of natural convection flow around horizontal cylinders (Appendix A). Inflation layers at the walls of the tank, PCM and coil was generated. Inflation layers are non-uniform expanding grid and are created by inflating the local rectangular face elements. In the vicinity of the tank walls, 10 inflation layers with

a bias factor (total expansion ratio) of 15 was created, which have a total thickness of 1.75 centimeter. Around each PCM module, 20 inflation layers with a bias factor of 20 was created whose total thickness was set to be half of the gap between each two adjacent modules. For the coil, 15 inflation layers with an expansion factor of 1.03, was created. The first layer was set to 0.0002 m. In the third dimension of the model, two mesh layers were assigned. The mesh size was set to 4 mm in all directions. An example grid for 10% PCM in the tank is shown in Figure 19. The number of nodes of the standard grid for varied from around 115,000 nodes for 2.5% PCM volume percentage to 220,000 nodes for 35% PCM volume percentage in the tank.

To ensure that the results are independent of the grid, the models with the lowest and highest PCM volume percentages were also simulated with a finer grid. In this grid, the number of inflation layers at the vicinity of the tank walls and the PCM modules were increased to 15 and 30 respectively. Also at the coil, the first layer thickness was set to 0.0001 m, and the number of layers was increased to 20. The number of nodes of the fine grid varied from around 125,000 nodes for 2.5% PCM volume percentage to 330,000 nodes for 35% PCM volume percentage in the tank. The grid independence study was successful and the PCM and coil heat transfer coefficients had less than 1% difference. The detailed results of the grid independence study are presented in the next chapter.

4. Simulation Parameters

Results from the lumped system model presented in chapter 3 indicated that the critical parameters for system performance are the heat transfer coefficients for PCM and coil, heat transfer areas and PCM volume fraction. Therefore solving for the quantity "hA" in the system during charging can provide a good representation of the performance of the systems with different PCM module geometries and configurations. Moreover from the lumped system model studied, it was observed that when the PCM reaches its melting temperature, the system reaches a steady condition. Therefore, to compare the performance of different geometries of the PCM modules in the tank, it is of interest to obtain the steady state solution in which all the PCM in the tank is undergoing phase change and has a constant temperature equal to its melting point.

This study focuses on solving for the heat transfer characteristics of the natural circulation within the water for a given PCM melt and coil temperature. As such, the goal is to determine the heat transfer coefficients from water to the PCM for different geometries and configurations. Due to the PCM's low thermal conductivity, the temperature inside the PCM is not uniform and its surface temperature increases after melting. In the current work, however, the heat transfer within the PCM module is not considered and it is assumed that the PCM maintains a constant surface temperature while changing phase. Future studies

will account for the internal melting mechanisms and heat transfer characteristics of the PCM module during this stage.

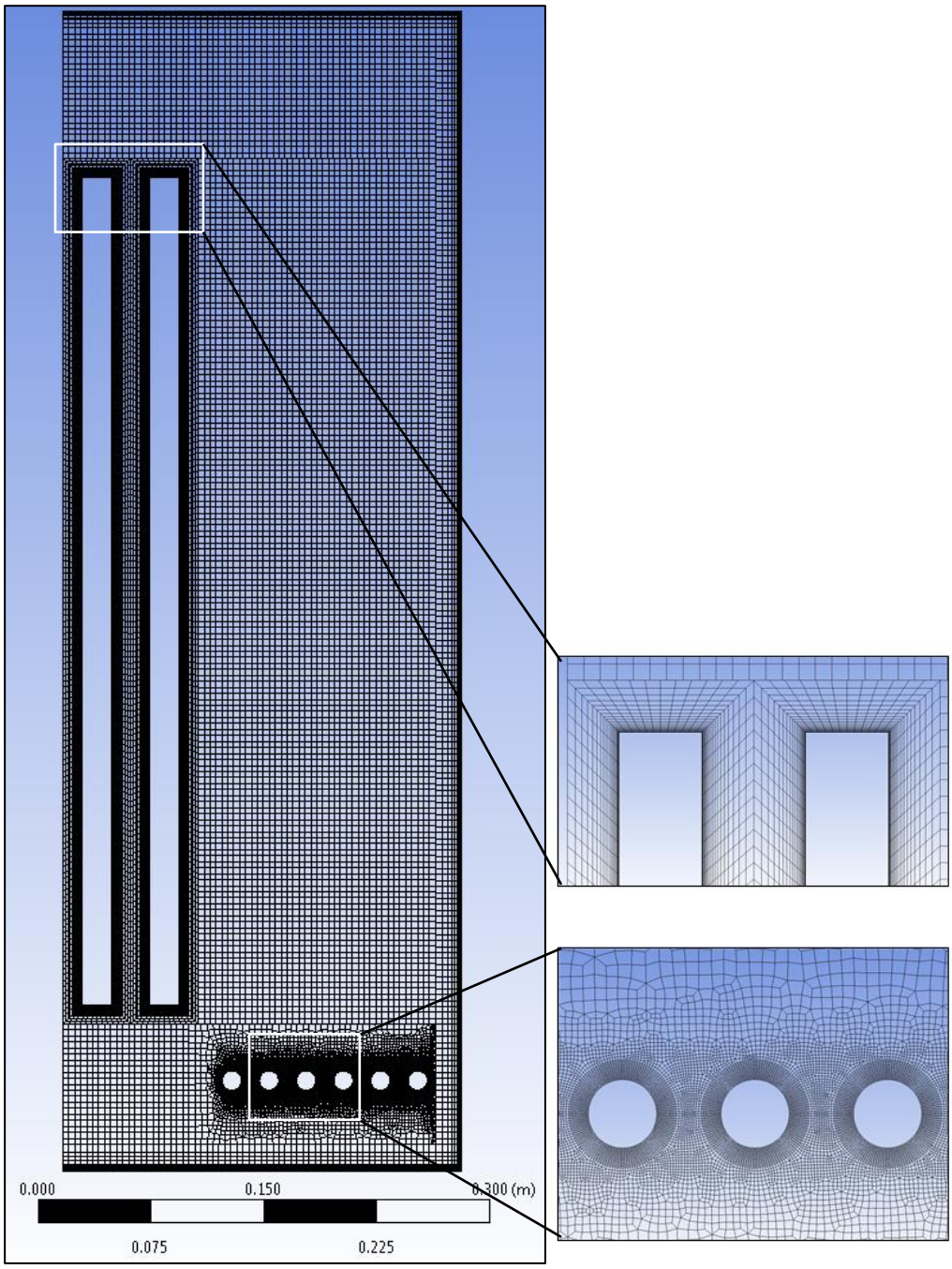

Figure 19-The grid for 10% PCM in the tank

Table 7-Model boundary conditions

Boundary Name	Boundary Condition
PCM	Fixed temperature no slip walls
Tank walls	Adiabatic no slip walls
Coil	Fixed temperature no slip walls
Left side	Symmetry
Front and back	Symmetry

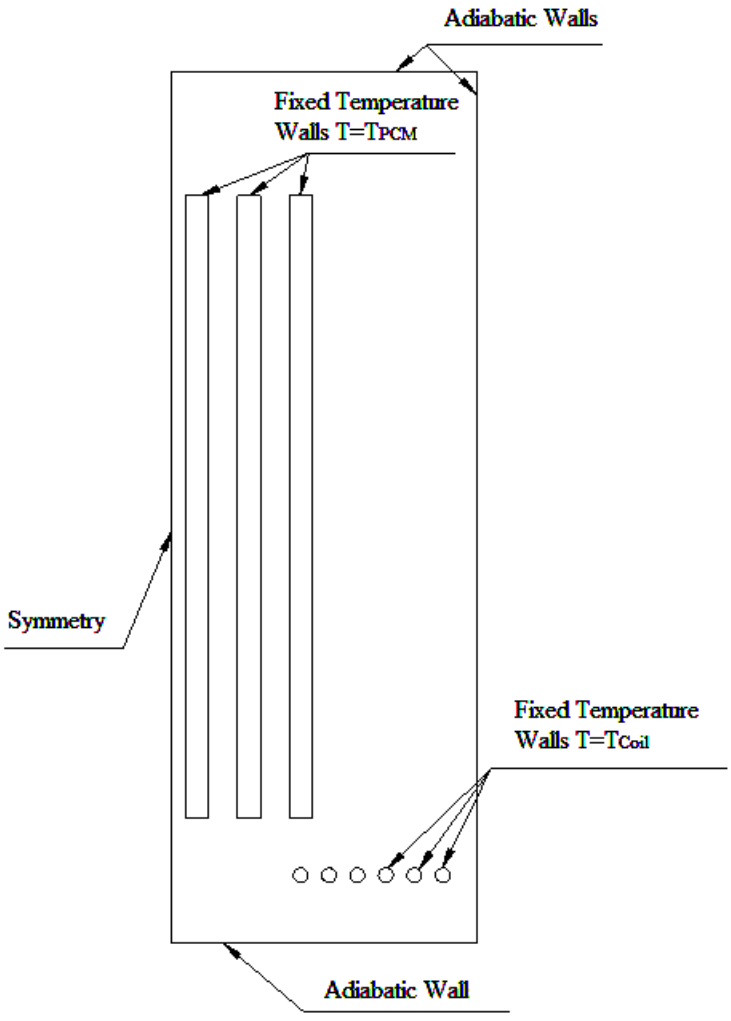

Figure 20-Boundary conditions of the model under study with 15% PCM

For all the cases studied, the coil is also assumed to have a constant temperature, which was estimated to be the average temperature of the inlet and outlet temperature to the system. The walls of the tank are assumed to be insulated and therefore their boundary condition is set to adiabatic walls. The details of the boundary conditions are given in Table 7 and Figure 20.

5. Numerical Solution

The Rayleigh number (Ra) for a 0.55 m fixed temperature flat plate with a 10℃ temperature difference between the surface of the plate and the infinity is $Ra = 3.57 \times 10^{10}$ which shows that the flow is expected to be turbulent. Therefore in modeling the tank containing PCM modules, the type of the flow is set as turbulent. However since Rayleigh number is close to the transitional region (10^9 [40]), the flow is expected to be transitional. As Rundle [54] reported, the SST model could predict the Nusselt numbers better than the other two-equation models ($k-\varepsilon$ and $k-\omega$). In this study we are mostly dealing with the predictions of the heat transfer coefficient of the PCM modules, therefore all the models are simulated with the $k-\omega$ based shear stress transport model (SST model) which is introduced in Appendix B.

Although the interest in this work is to solve for steady flow in the tank when the PCM is melting it was found that code convergence for exactly steady conditions did not occur: i.e. the RMS residuals of U, V and W did not converge below

10^{-3}. As the flow is buoyancy driven, unsteady plumes of heated water are created at the coil. These plumes and the overall low intensity of the turbulence in the tank are unsteady and of transient nature. Therefore, the flow was solved as transient with initial temperature of water being equal to the melting temperature of the PCM. The solution progressed as a transient until it reached a quasi-steady state. It was determined to be in a quasi-steady state when the time-averaged heat imbalance was small (less than 1% of the heat transfer rate to the PCM). The convergence factor was then the time averaged heat imbalance of the system during the last 2000 time steps of the simulation. The reason behind choosing an interval of 2000 time steps was that the average duration of the heat imbalance fluctuations was around 300 to 400 time steps, and it was necessary to capture a few of them to have a meaningful timed-average of the heat imbalance. The heat imbalance of the system is defined as the heat transfer rate from the coil to the system minus the heat transfer rate from the system to the PCM. When the time averaged heat imbalance of the system is zero, it means that although the flow shows some fluctuations and unsteadiness, the heat transfer is essentially constant. An example of the convergence of a model with 2.5% PCM in the tank is given in Figure 21. Figure 22 also shows the water bulk temperature during the simulation time for 2.5% PCM in the tank.

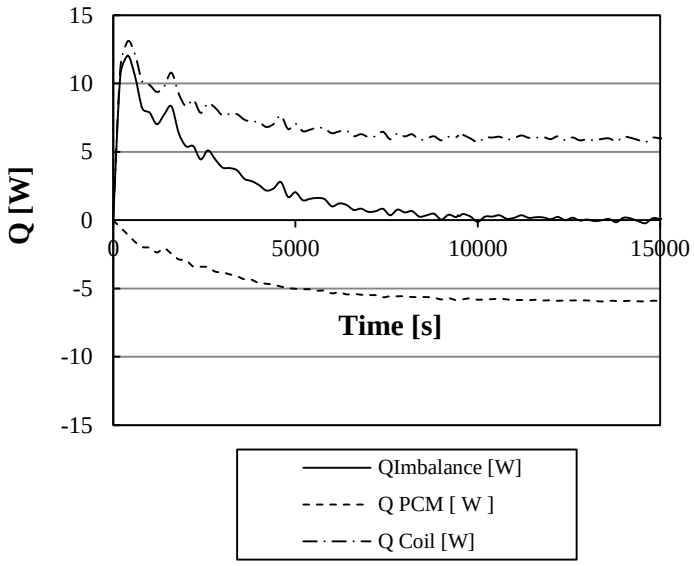

Figure 21-Heat imbalance, heat transfer rate from water to PCM, and heat transfer rate from coil to water in a system with 2.5% PCM in the tank (Note that the heat imbalance of the system is the summation of the heat transfer rate from the coil and to the PCM since $\dot{Q_{PCM}}$ is negative).

Initially water temperature is set to $295°K$ (same as PCM), so initially the coil heat transfer goes to heating the water and the heat transfer to the PCM is small. After some time the water bulk temperature flattens (Figure 22), and takes a constant value between coil temperature and PCM temperature. In this stage, the heat transfer from the coil to water equals the heat transfer from water to the PCM. The time-average heat imbalance of this system for the last 2000 time steps (time step = 1 [s]) is 0.00 [W].

The default initial and boundary conditions of the PCM, coil and water is given in Table 8.

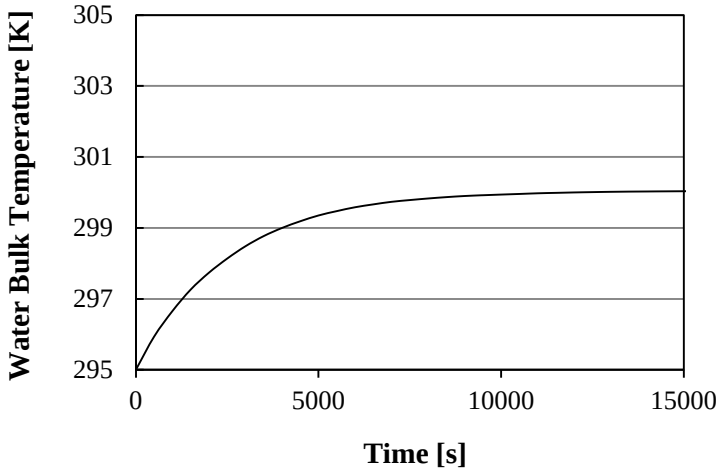

Figure 22-Water bulk temperature versus simulation time for 2.5% PCM in the tank

Table 8-Initial and boundary conditions of PCM, coil and water

Boundary	**Condition**
PCM	Boundary condition: Fixed temperature no slip wall $T_{PCM} = 295K$
Coil	Boundary condition: Fixed temperature no slip wall $T_{Coil} = 305K$
Water	Initial condition: $T_{water} = 295K$

6. Summary

In summary, the geometry used in this research is inspired by the work presented by Mather et al. [6]. The dimensions of the three dimensional cylindrical tank studied by Mather et al. is transformed to an almost square based rectangular tank of the same volume and height. The surface area of the coil is also maintained between the tanks and the centerline vertical cross section of the tank is modeled. In this research, eight different PCM volume percentages were studied. To ensure

that the results are independent of the grid, the models with the lowest and highest PCM volume percentages were also simulated with a finer grid. The goal of this study is to determine the heat transfer coefficients from water to the PCM for different PCM volume percentages and module placements for a specific surface temperature that the PCM modules have. The following chapter presents the results and discussions of different models studied.

CHAPTER 5 Simulation Results and Discussion

1. Introduction

This chapter presents and discusses the results of the simulations performed for two dimensional tank with submerged fixed temperature PCM modules and coil tubes. The first part of the chapter is allocated to mesh independence tests. This is followed by a section on the detailed results for one case (20% PCM in the tank). Then the study investigates the effect of various parameters on the heat transfer and the flow properties in the tank. The key parameters that affect the performance of the system are studied here which include: the gap between two

PCM modules, PCM volume percentage, and temperature difference between PCM and coil.

2. Mesh Independence Test

Simulations for the geometries with the smallest and largest PCM volume percentages (2.5% and 35%) were tested for mesh independence, through the use of two fine and coarse mesh sizes. The properties of the grids used are given in the previous chapter. The two geometries are shown in Figure 23.

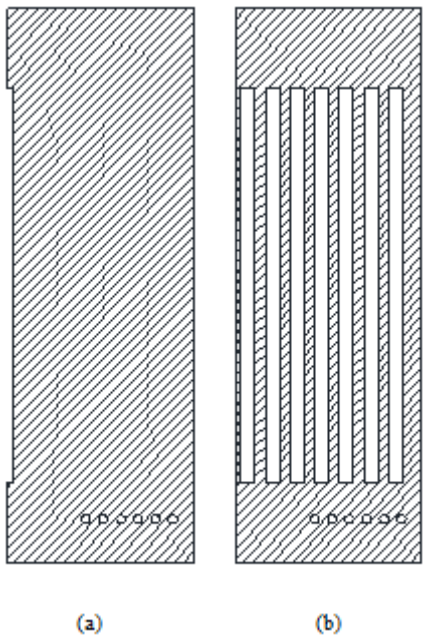

Figure 23-Geometries of the models with (a) 2.5% PCM, (b) 35% PCM in the tank studied to assess grid independence

Figure 24 shows the heat imbalance of the system as well as, the heat transfer rate from the coil and to the PCM separately throughout the simulation for both meshes in the two geometries. As shown in Figure 24, the heat imbalance in both systems converges to zero with an average absolute deviation of 0.13 W for $\varphi = 2.5\%$ and 0.28 W for $\varphi = 35\%$. The higher deviation in models with higher PCM volume percentages shows more fluctuations in the flow in these cases. When the timed-average heat imbalance of the system reaches zero, the heat transfer rate to the PCM modules equals the heat transfer rate out of the coils. This figure also shows the agreement of the heat transfer rates from the coil and to the PCM at the end and throughout the simulation for the two mesh sizes.

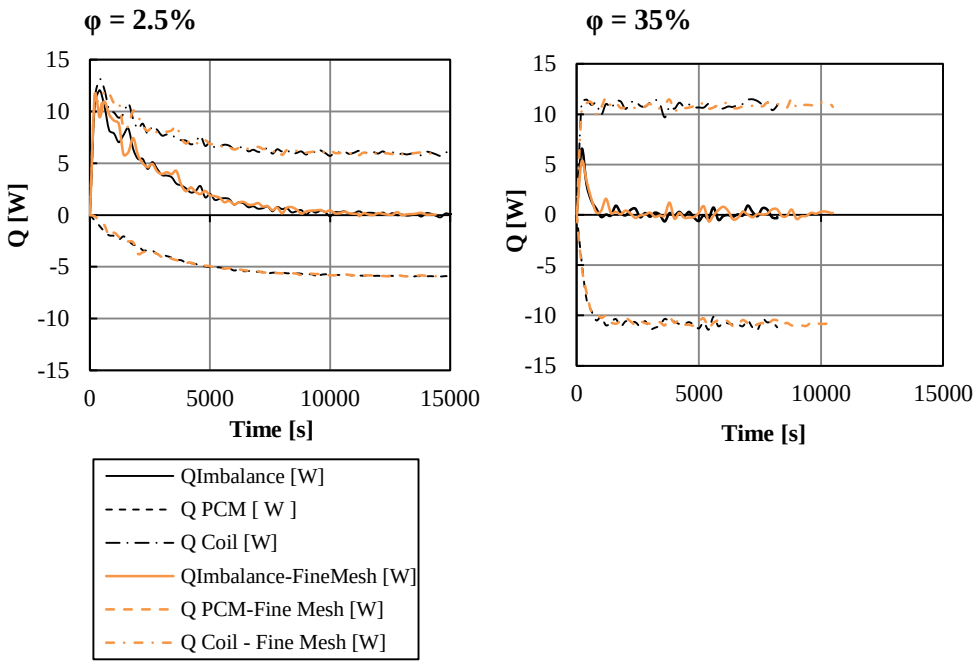

Figure 24-Heat imbalance, PCM heat transfer rate, and coil heat transfer rate vs. simulation time for 2.5% and 35% PCM in the tank for two mesh sizes

Table 9 compares different flow parameters and heat transfer characteristics in the two geometries for different mesh sizes. As it is shown in the table, the results of the coarse mesh have less than 1% difference in comparison to the results of the fine mesh.

Table 9- Results of the mesh independence test

Parameter	**Mesh size**	$\boldsymbol{\varphi = 2.5\%}$	$\boldsymbol{\varphi = 35\%}$
Water bulk temperature	Coarse	$300.0K$	$295.8K$
	Fine	$300.0K$	$295.8K$
	Difference	0.0%	0.0%
PCM heat transfer coefficient	Coarse	$260\ W/m^2K$	$214\ W/m^2K$
	Fine	$258\,W/m^2K$	$213\ W/m^2K$
	Difference	0.8%	0.5%
Coil heat transfer coefficient	Coarse	$621\ W/m^2K$	$628\ W/m^2K$
	Fine	$623\ W/m^2K$	$623\,W/m^2K$
	Difference	-0.3%	0.8%

3. Heat Transfer Characteristics of the Flow for 20% PCM in the Tank

This section presents the results for one of the cases studied (PCM volume percentage of 20%). The convergence of the heat imbalance of the system is shown in Figure 25. The time-averaged heat imbalance for the last 2000 time steps is 0.10 W, and the average deviation is 0.29 W.

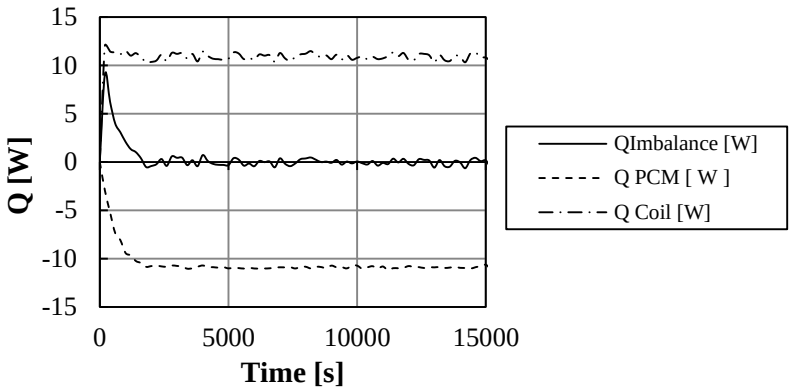

Figure 25-Heat imbalance, PCM heat transfer rate, and coil heat transfer rate versus simulation time for 20% PCM in tank

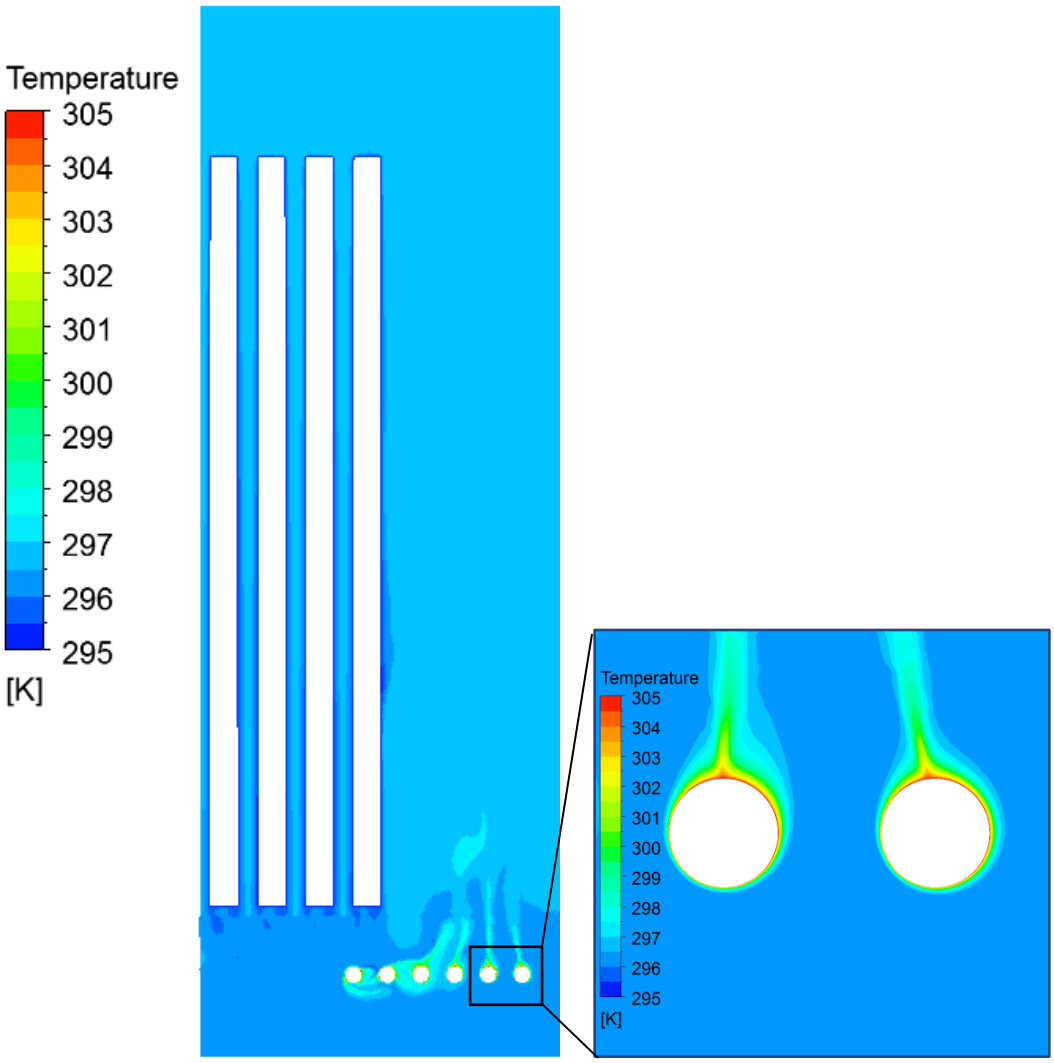

Figure 26-Temperature contours in a tank with 20% PCM

In this case, as in all other cases, PCM and coil temperature is set to $295K$ and $305K$ respectively, and the initial water temperature was $295K$. After convergence is achieved the water bulk temperature takes a constant value of $296.3K$. Temperature contours in the domain is shown in Figure 26. This figure shows how well mixed the tank is. The plumes of heated water created at the top of the coil are also evident in this figure.

The temperature profile at the mid-height of the tank is shown in Figure 27. Note that the water bulk temperature in this case is $296.3\ K$.

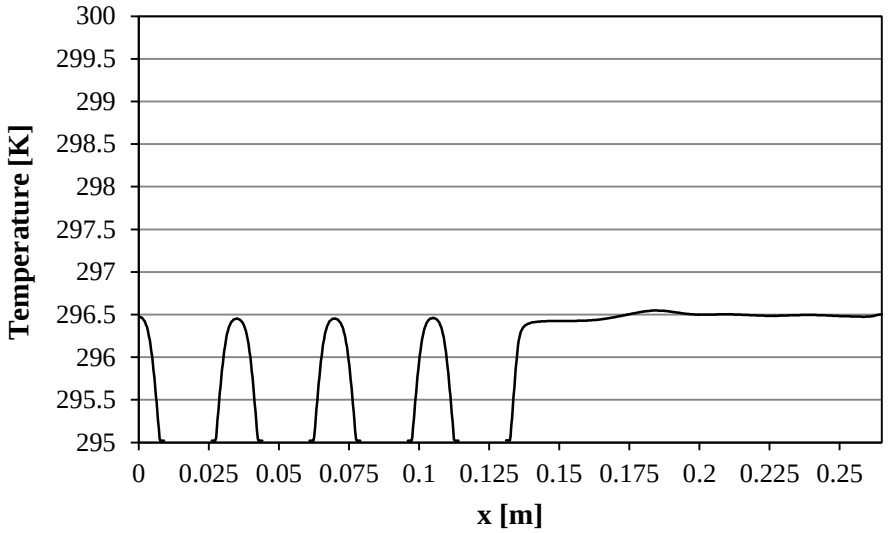

Figure 27-Temperature profile at the mid-height of the tank for 20% PCM in the tank.

The velocity vectors in the tank shown in Figure 28, shows the recirculation of the flow. Also in this figure the interference of the downward flow from the PCM modules with the flow from a few of the coil tubes is evident.

Figure 29 shows the turbulence eddy viscosity in the tank. As it is shown, the highest turbulence is occurring at the top right. This is the reason that the fluid is

well mixed in this region. This figure also shows how the flow around the coil is laminar.

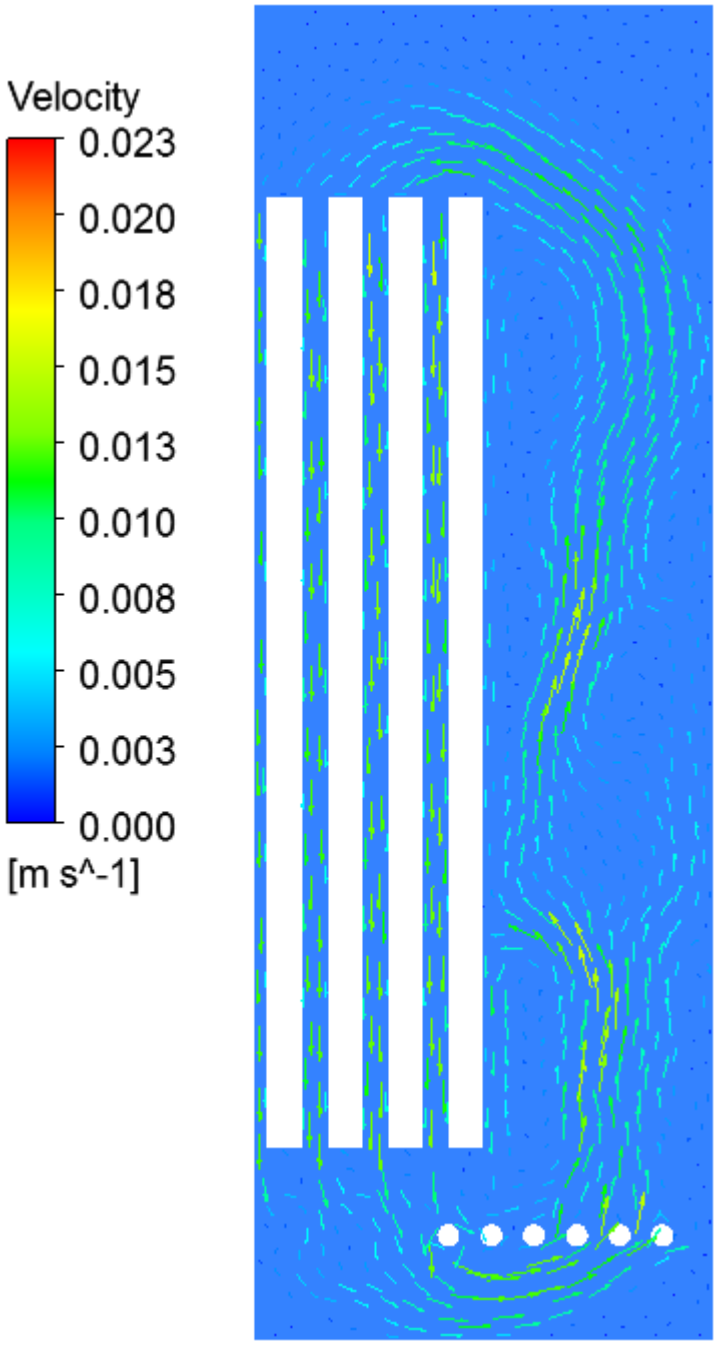

Figure 28-Velocity vectors in a tank with 20% PCM

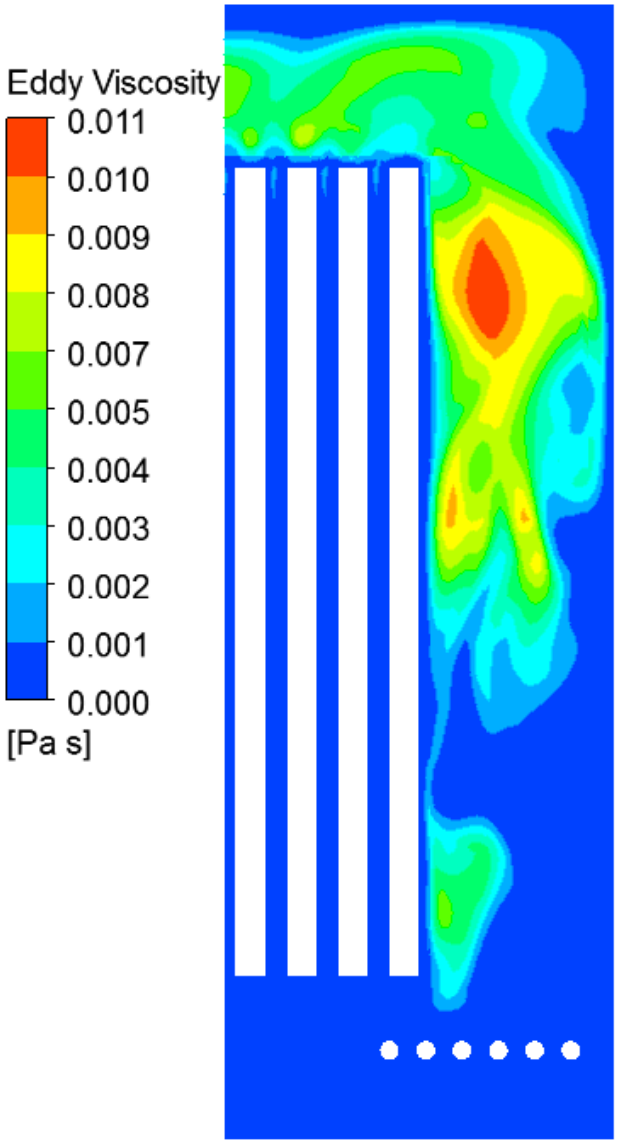

Figure 29-Turbulence eddy viscosity in a tank with 20% PCM

4. The Effect of the Gap Between the PCM Modules on the Heat Transfer Characteristics of the Flow

By adding modules in the tank in order to increase the PCM volume percentage in the tank and correspondingly increase the energy storage capacity of the system, the gap between the modules plays an important role in the heat transfer

characteristics of the systems. If the modules are too close to each other, the boundary layers created through natural convection will interact. This results in a decrease in the velocity of the flow between the plates which in turn reduces the heat transfer to the PCM. If the direction of the plate is the y direction and the boundary layer thickness at y distance downstream is called δ, then the boundary layer thickness at the bottom end of the PCM modules ignoring the interactions of the upward flow from the coil can be estimated through the equation below given by Holman [40].

$$\frac{\delta}{y} = 3.93 Pr^{-1/2}(0.952 + Pr)^{1/4} {Gr_y}^{-1/4} \tag{19}$$

$$Gr_y = \frac{g\beta(T_s - T_\infty)y^3}{\nu^2} \tag{20}$$

The value of the parameters in the above equation for water at $300K$ is given in Table 10.

Table 10-Properties of the flow at film temperature to study the effect of the gap between the PCM modules on the heat transfer characteristics of the flow [53]

Pr, Prandtl number	5.829	ρ, Density	$9.97 \times 10^2 \frac{kg}{m^3}$
g, Acceleration due to gravity	$9.806 \frac{m}{s^2}$	L, Module length	$0.55\ m$
β, Volumetric thermal expansion coefficient	$276.1 \times 10^{-6}\ K^{-1}$	T_s, Module surface temperature	$295K$
μ, Dynamic viscosity	$855 \times 10^{-6}\ N.\frac{s}{m^2}$	T_∞, Bulk temperature	$298.6K$

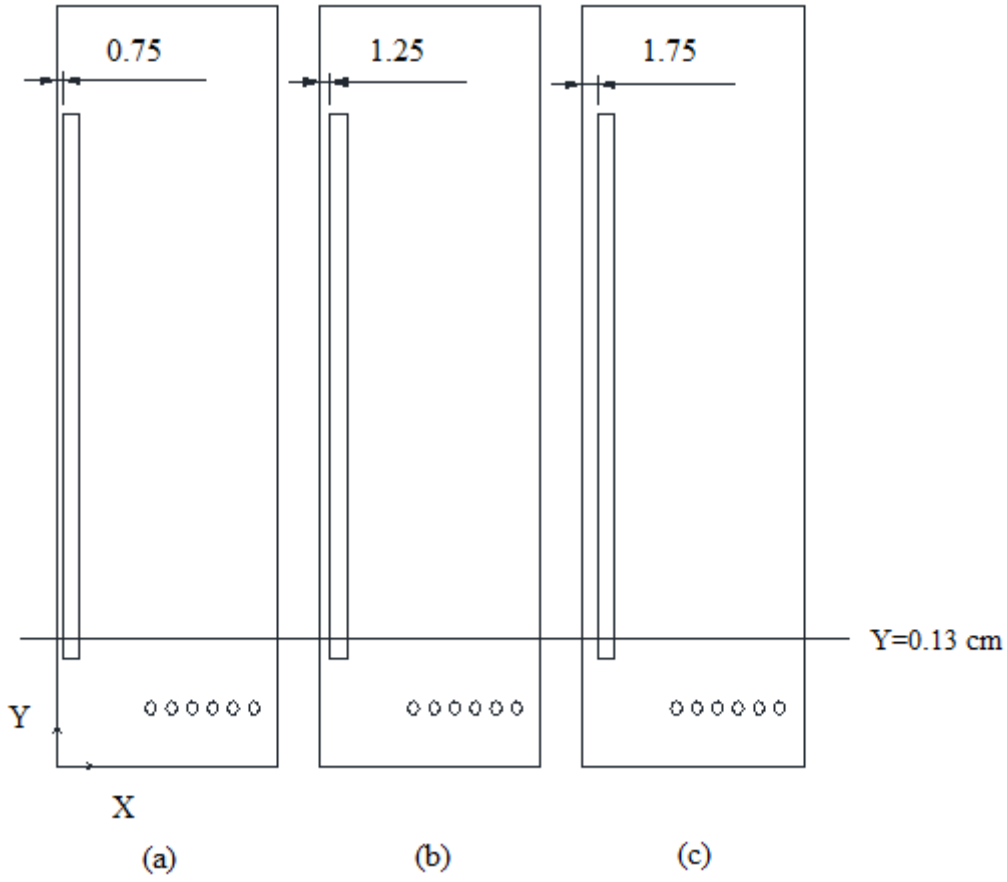

Figure 30-The geometry of the models with 5% PCM and different module gaps of: (a) 1.5 cm (b) 2.5 cm (c) 3.5 cm

For a $Gr = 2.20 \times 10^9$, the boundary layer thickness at the bottom end of the PCM module is approximately 0.67 centimeter. This means that the gap between the modules should be at least twice that in order to fully take advantage of the boundary layer development and maintain high heat transfer rates. To computationally assess the effect of the gap on the heat transfer coefficient of the PCM modules, three models containing 5% PCM (two modules in the tank) were studied. In these models, the two modules were set to have three different distances (1.5, 2.5 and 3.5 centimeter) from each other (note that only one module

is placed in the model since only half of the tank is modeled). The geometry of the models studied is given in Figure 30.

Comparing the heat transfer coefficients of the PCM and coil calculated in different models, Table 11, it is evident that the heat transfer characteristics of the flow is almost unchanged (within 1% of model 'c').

Table 11-Heat transfer characteristics of the flow for modules with different gaps

Parameter	Gap =1.5 cm	Gap=2.5 cm	Gap=3.5 cm
Water bulk temperature	$298.6K$	$298.6K$	$298.6K$
PCM heat transfer coefficient	$244\ W/m^2K$	$246\ W/m^2K$	$243\ W/m^2K$
Coil heat transfer coefficient	$653\ W/m^2K$	$657\ W/m^2K$	$651\ W/m^2K$

Figure 31 shows a comparison between the developments of the velocity profiles between the two plates at different heights for models 'a', 'b' and 'c'.

From this figure it is shown that although the initial parabolic shaped velocity profile and its peak varies for different module gaps, further downstream the peak velocities in the boundary layers created by natural convection is almost the same. This is further supported in Figure 32 which shows a closer look at the velocity profiles at $y = 0.13\ m$ for the three models.

These figures show that reducing the gap between the modules is not affecting the development of the boundary layer. In neither of the cases, the velocity profile is fully developed. Figure 33, shows the changes in the velocity profiles at different

heights in model ‘a’. This figure shows that the peak velocity in the boundary layer is increasing as we go further downstream.

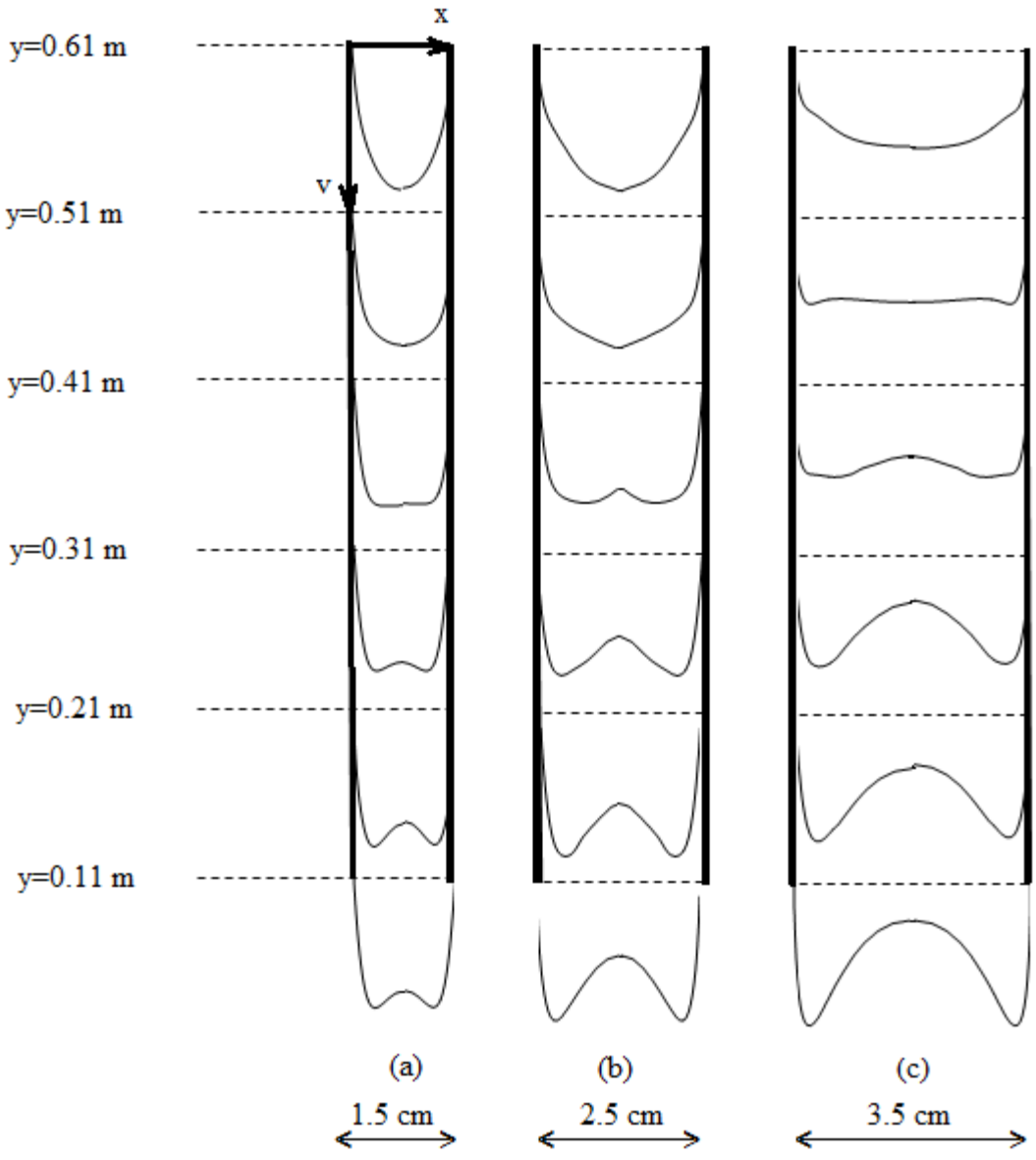

Figure 31- A comparison of the velocity profiles at different heights between two PCM modules with different gaps

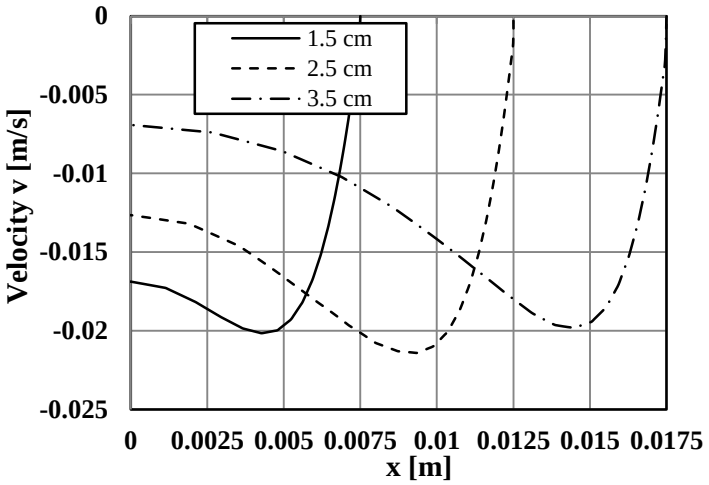

Figure 32-Velocity profiles at (y=0.13 m) and between the two PCM modules with different gaps, (Note that x=0 coincides with the tank centerline)

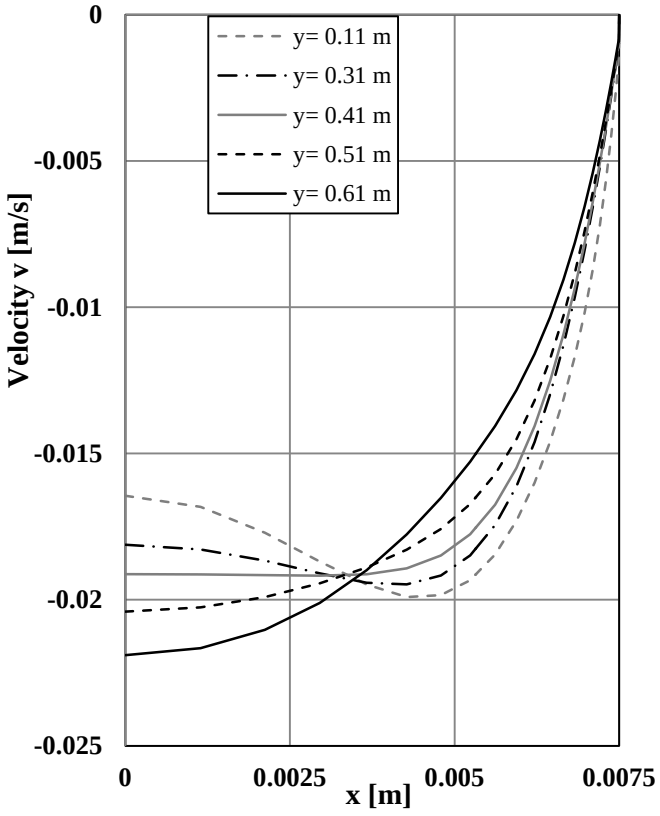

Figure 33-Right half velocity profiles at different heights between the PCM modules in model 'a' (gap=1.5 cm)

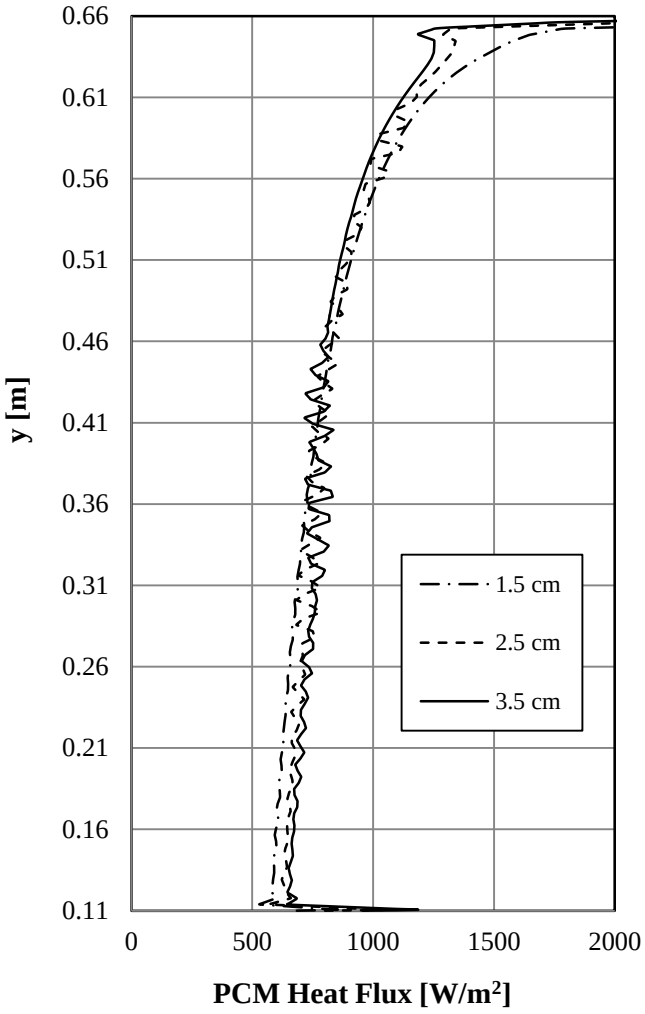

Figure 34- PCM local heat flux between the modules versus y for different modules gaps (Note that at the bottom of the plate y=0.11 m and at the top y=0.66 m)

Figure 34 shows the PCM local heat flux between the plates as a function of y. As it is shown in the figure, the overall area integration of the heat transfer rate is almost constant, which leads to very similar heat transfer coefficients for the three cases.

As shown in Figure 31 to Figure 34 the flow is developing over the entire length of the channel therefore the boundary layers do not interact, and the heat transfer

is not really affected by the gap. As long as the velocity profiles are developing and the gap between the plates is not less than the boundary layer thickness at the end of the modules, the gap between the plates will not affect the heat transfer coefficients of the modules.

5. The Effect of PCM Volume Percentage on the Heat Transfer Characteristics of the Flow

It was hypothesized that by spacing the PCM modules equally throughout the width of the tank, the upward flow of the coil would block the downward flow from the modules. From the previous section it was concluded that for the length of the channels considered, maintaining the gap between the PCM modules greater than 1.4 centimeter, the heat transfer characteristics of the flow would not be affected, for the conditions considered. Therefore, the PCM modules were placed in the center of the tank with small gaps between them. For high PCM volume percentages (greater than 20%) packing all the modules in the center was not possible with a minimum gap of 1.5 cm maintained between the modules. The goal was to create a recirculating flow from the coils at the sides upward, and from the modules in the center downward.

Eight different PCM volume percentages were studied. The volume percentages, their corresponding number of modules and the size of the gap between them are

given in Table 12. Figure 35 also shows the placement of the modules in the tanks.

Table 12-PCM volume percentages, their corresponding number of modules, and the gap between them studied

Model	**Number of plates in the tank**	**Number of plates in the simulation model**	**PCM volume percentage (Nominal value)**	**Module gaps (cm)**
a	*1*	*0.5*	2.5%	-
b	*2*	*1*	5%	3.5
c	*4*	*2*	10%	2.5
d	*6*	*3*	15%	2.0
e	*8*	*4*	20%	1.5
f	*10*	*5*	25%	1.5
g	*12*	*6*	30%	1.5
h	*14*	*7*	35%	1.5

The initial and boundary conditions of the models are the same as before, and are given in Table 8.

The heat transfer rate from the coil to the water, from water to the PCM and the heat imbalance of the system is calculated during the simulation and plotted versus time in Figure 36 for 5%, 15%, 25%, 35% PCM volume fractions in the tank. Figure 36 shows that the higher the PCM volume percentage in the tank, the faster the time-average heat imbalance of the system converges to zero.

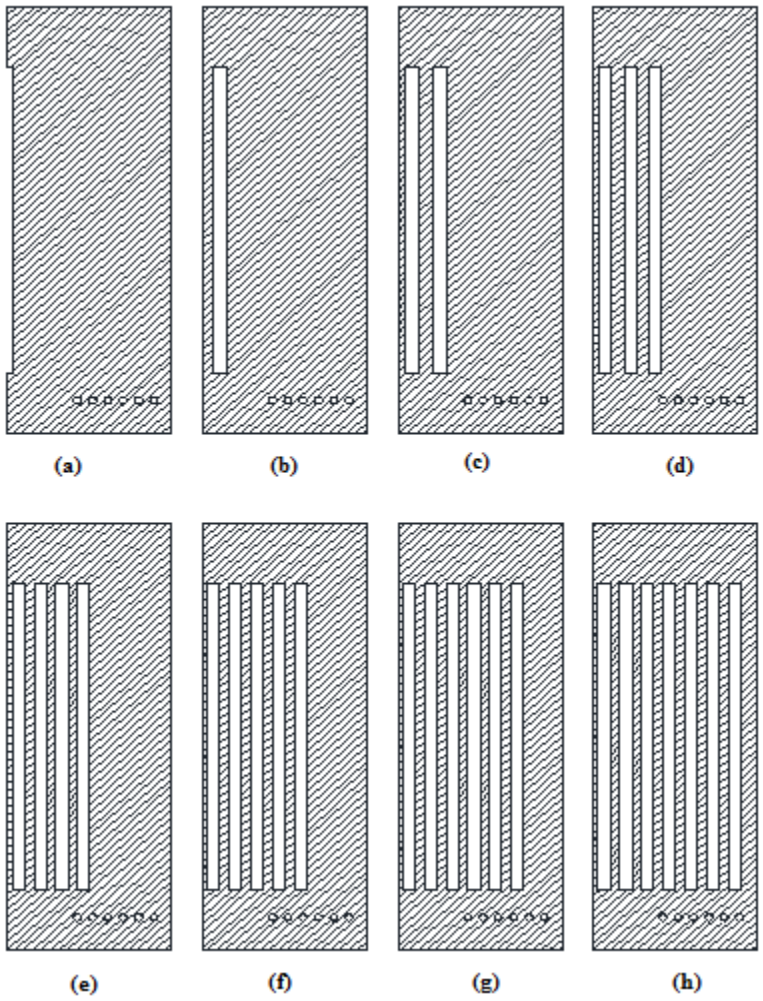

Figure 35-Geometries of the eight models simulated to study the effect of PCM volume percentage on the heat transfer characteristics of the flow

During the simulations the bulk temperature of water is calculated and plotted versus the simulation time. The plots for four different PCM volume percentages are given in Figure 37. This figure shows that the final bulk temperature of water is closer to the PCM surface temperature when PCM volume percentage is higher. Since the initial temperature of water is equal to the PCM surface temperature, the fact that the final water bulk temperature is closer to the PCM volume percentage

makes the heat imbalance of these systems converge faster. Also there is less water in tanks with higher PCM volume percentages which contributes to the cases converging faster.

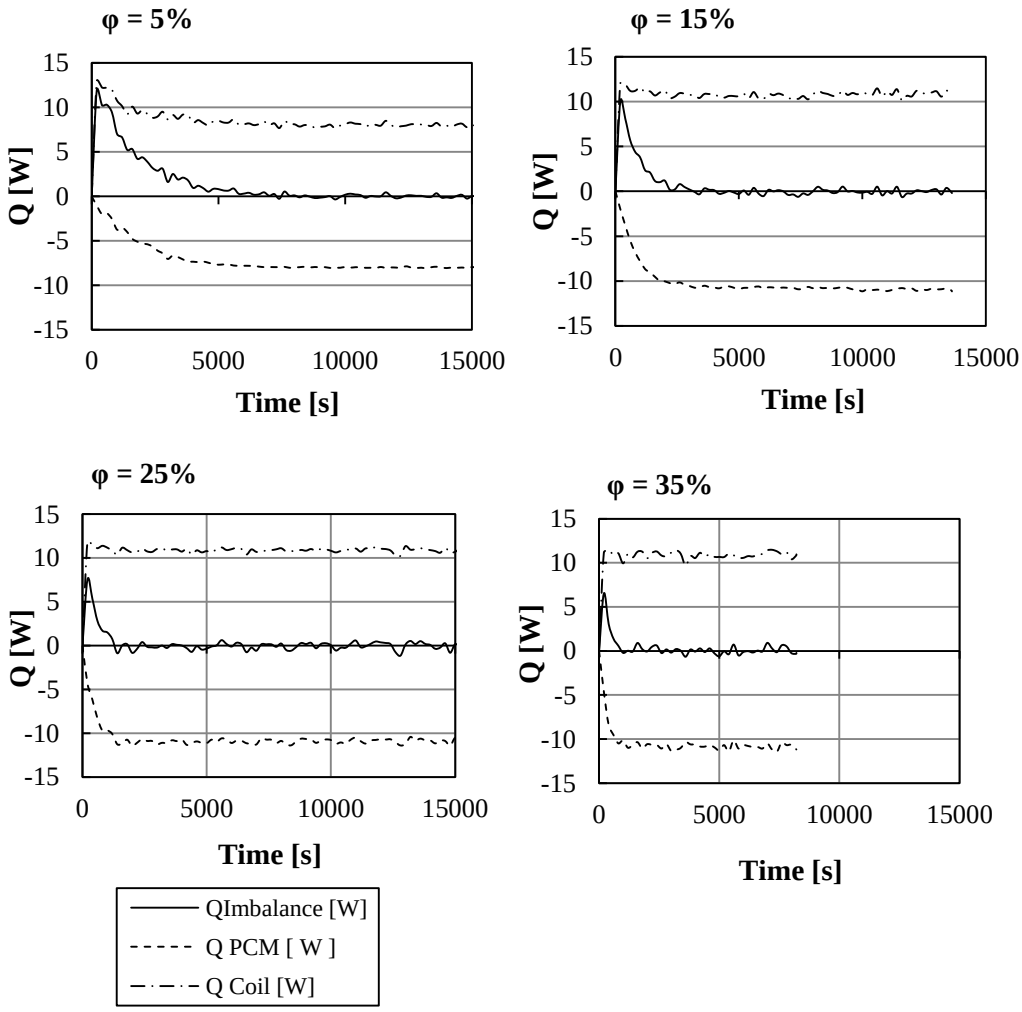

Figure 36-Heat transfer rate from the coil to the water, from water to the PCM, and the heat imbalance of the system versus simulation time

Figure 36 also suggests that there is an unsteady since that the value of the heat imbalance of the system is fluctuating. Time averaged value of this parameter is very close to zero which shows the models have reached convergence, and that

other properties of the flow are not expected to change with time. As is expected, when the heat imbalance of the system converges to zero, the water bulk temperature reaches a near constant value. This final value is considered as the bulk temperature where the heat transfer coefficient of the modules is calculated.

The time averaged heat imbalance of the system for the last 2000 time steps of the simulation for all the eight models studied is given in Figure 38. The maximum time averaged heat imbalance of the eight models is 0.02 W which in comparison to the average heat transfer rate to the PCM is very small (less than 0.5%).

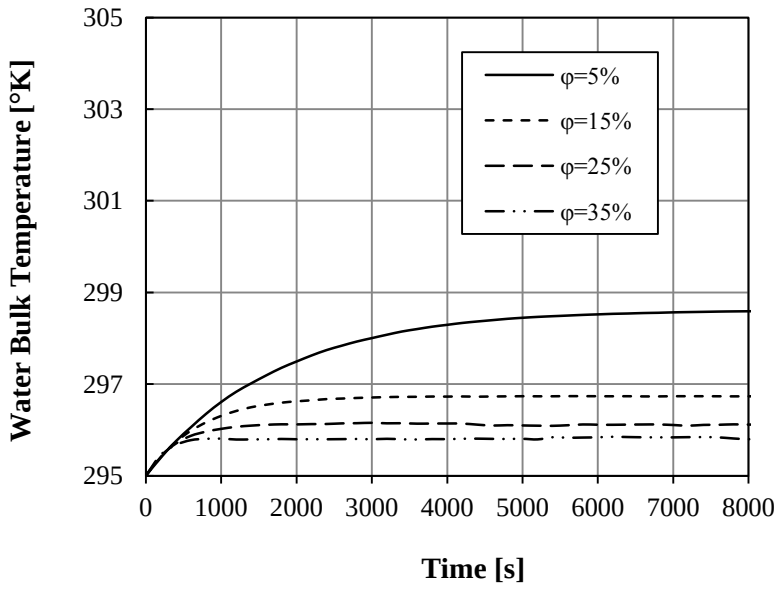

Figure 37-Water bulk temperature versus time for different PCM volume percentages where PCM temperature is $295K$ and coil temperature is $305\ K$

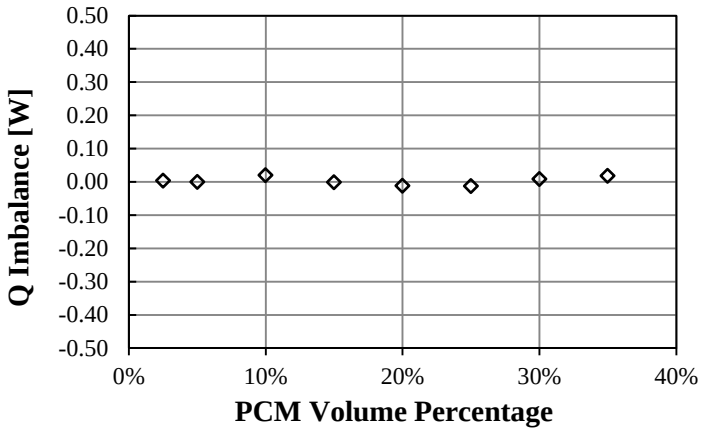

Figure 38-Time averaged heat imbalance of the system for the last 2000 time steps of the simulations versus PCM volume percentage

5.1. Water Bulk Temperature

Water bulk temperature is calculated through the area integration of water temperature over the domain. For every model, the water bulk temperature takes a value between the PCM and coil surface temperatures. To look at the variations of this parameter independent of the PCM and coil surface temperatures, it can be non-dimensionalized as follows:

$$\theta_w = \frac{\bar{T}_w - T_{PCM}}{T_{Coil} - T_{PCM}} \tag{21}$$

where θ_w, is the dimensionless average water bulk temperature. Plotting the dimensionless water bulk temperature for different PCM volume percentages, shown in Figure 39 suggests that by increasing PCM volume percentage in the tank θ_w decreases.

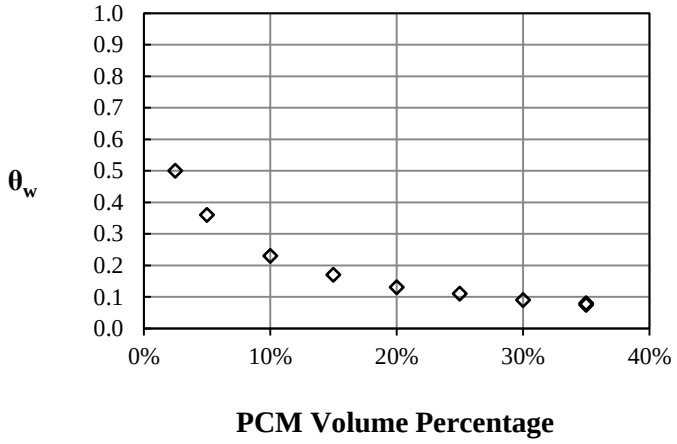

Figure 39-Dimensionless water bulk temperature versus PCM volume percentage in the tank

The charge rate of the system can be written as the following:

$$\dot{Q} = \frac{1}{R_{total}}(T_{Coil} - T_{PCM}) \tag{22}$$

in which the total resistance between the coil and the PCM, Figure 40, can be written as:

$$R_{total} = \frac{1}{(hA)_{coil}} + \frac{1}{(hA)_{PCM}} \tag{23}$$

Therefore, the highest charge rates are associated with the least total resistance.

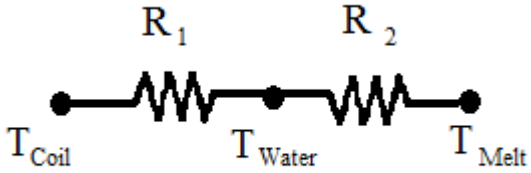

Figure 40-Total resistance between the water in coil and the PCM

The charge rate of the system can also be written as the heat transfer rate to the PCM:

$$\dot{Q}_{PCM} = h_{PCM} A_{PCM} (\bar{T}_w - T_s) \tag{24}$$

Therefore, the dimensionless water bulk temperature can be written as a function of $(hA)_{PCM}$ and $(hA)_{coil}$ as follows:

$$\dot{Q}_{PCM} = (hA)_{PCM} (\bar{T}_w - T_{PCM}) = \frac{1}{\frac{1}{(hA)_{coil}} + \frac{1}{(hA)_{PCM}}} (T_{Coil} - T_{PCM}) \tag{25}$$

then,

$$\theta_w = \frac{1}{1 + \frac{(hA)_{PCM}}{(hA)_{coil}}} \tag{26}$$

As the number of modules in the tank is increased, $\frac{(hA)_{PCM}}{(hA)_{coil}}$ becomes larger, and hence θ_w decreases.

5.2. PCM Heat Transfer Coefficient

The water to PCM heat transfer coefficient varies with different module placements and configurations. Figure 41 compares PCM module heat transfer coefficients from the simulations with the ones calculated from experimental correlations given by Bayley [50] and Warner et al. [49] for turbulent flows ($Nu = 0.1Ra^{1/3}$) and by McAdams [42] for laminar flows ($Nu = 0.59Ra^{1/4}$) for natural convection over a fixed temperature flat plate for different PCM

volume percentages in the tank. The ΔT used for the correlations is the temperature difference between PCM modules and water bulk temperature.

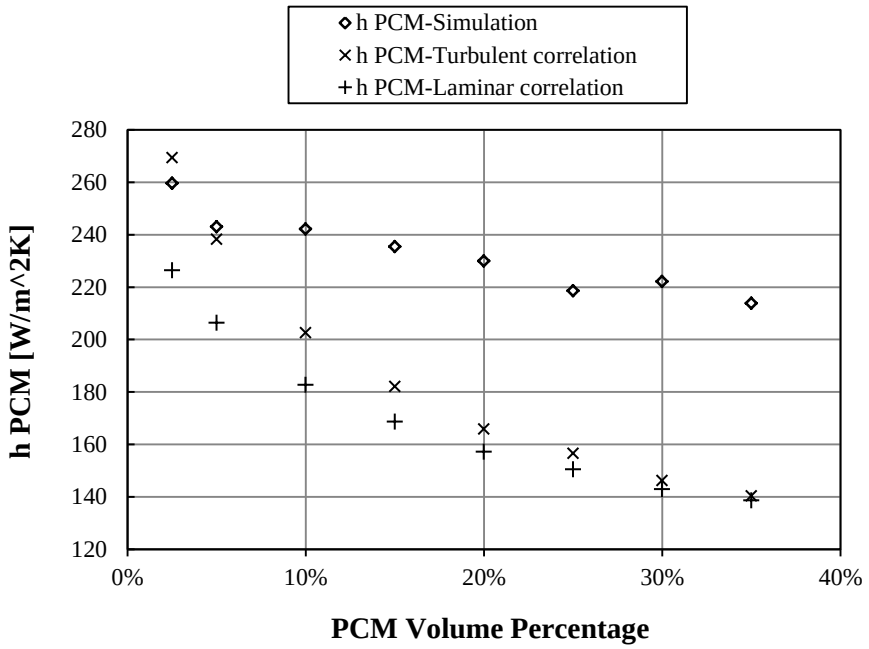

Figure 41- PCM module heat transfer coefficient versus PCM volume percentage in the tank calculated from the simulation, experimental correlation for turbulent flows, and experimental correlation for laminar flows. (Note that Rayleigh number was higher than 10^9 in all cases, and laminar correlation does not apply. However the purpose of using laminar correlation was only to follow the trend and compare the differences).

It is evident from this figure that the heat transfer coefficient of the PCM modules decreases with increasing PCM volume percentage. This is expected since water bulk temperature decreases as PCM volume percentage increases. This results in a smaller temperature difference, smaller Rayleigh numbers and therefore smaller PCM heat transfer coefficients. The water to PCM heat transfer coefficient calculated from the simulations for 35% PCM in the tank has reduced 18% in comparison to when there is only 2.5% PCM in the tank. The average of the

standard deviation of water to PCM heat transfer coefficient over the last 2000 time steps for different PCM volume percentages is 3 W/m^2K. The average value of the PCM heat transfer coefficient for these eight models is 233 W/m^2K.

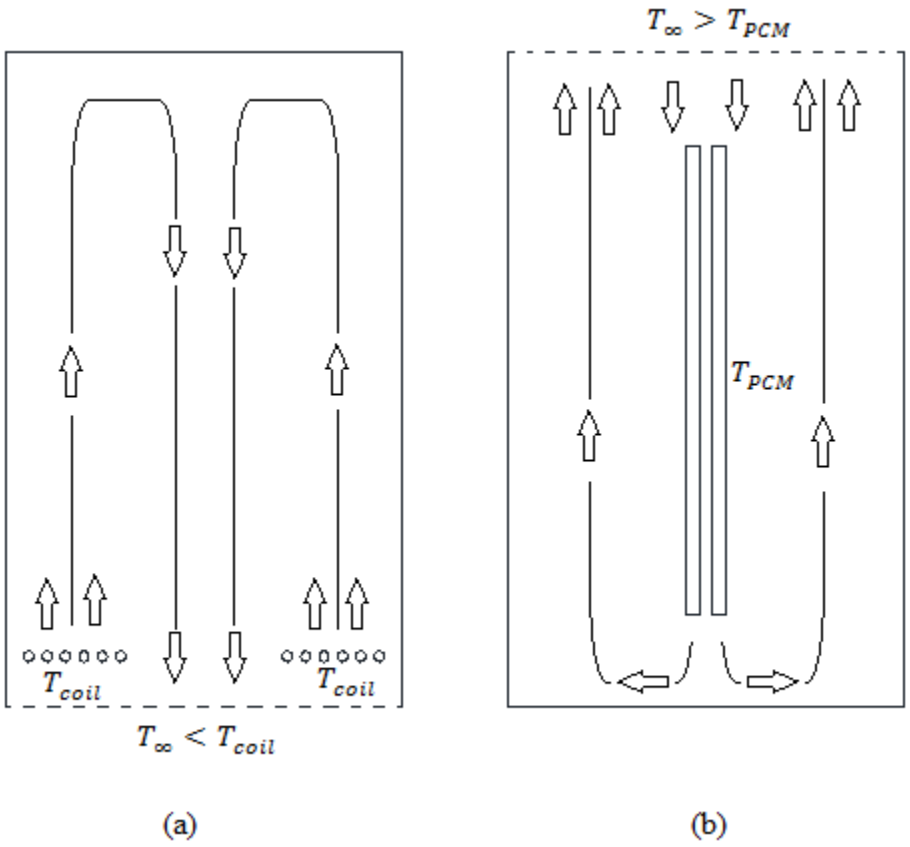

Figure 42-Natural convection flow around (a) heated coil in a tank with an open bottom with a fixed T_∞ (b) cooled PCM modules in a tank with open top with a fixed T_∞.

Figure 41 shows that the water to PCM heat transfer coefficients calculated from the simulations are by far bigger than the ones calculated from the correlations. This can be explained through Figure 42 which shows a schematic of the natural convection flow around (a) heated coil in a tank with an open bottom with a fixed T_∞ and (b) cooled PCM modules in a tank with an open top with a fixed T_∞. This

figure shows that both the PCM modules and coil tubes create a natural-convection-driven recirculation of the flow in the tank independently. Therefore placing them both in a closed tank will result in not only natural convection around each piece but also forced convection as a result of the circulation of the flow driven by the other piece, 'pumping effect'.

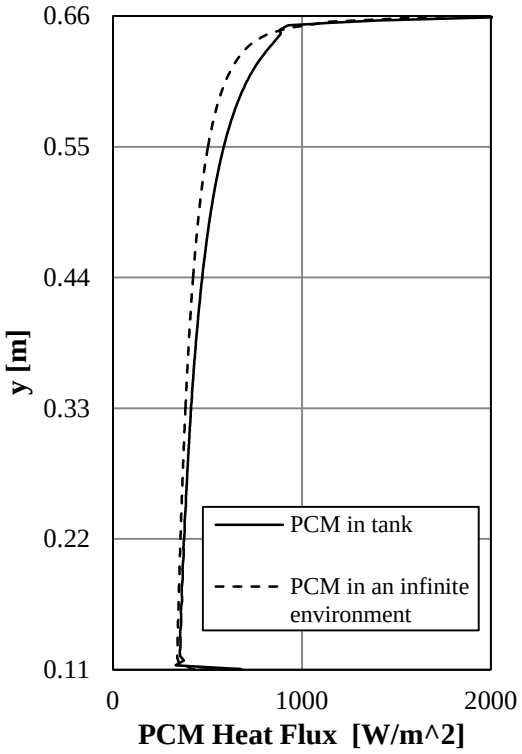

Figure 43-A comparison between the local heat flux at the PCM module in a tank with 10% PCM and the local heat flux at a fixed temperature vertical flat plate in an infinite environment with the same surface temperature as PCM and infinity temperature equal to the water bulk temperature in the tank.

To validate this idea, the local heat flux at the PCM modules for 10% PCM in the tank is compared to the local heat flux created solely by natural convection around a vertical flat plate, Figure 43. This figure shows that the heat flux at the top of the

plates is higher in the tank in comparison to when the plate is located in an infinite environment. This is mainly due to the recirculation of the flow in the tank that creates higher initial velocity profiles at the top of the PCM modules.

The velocity profiles at the mid-height of the tank ($y = 0.385\,m$) for 5 to 35% PCM is shown in Figure 44. As it is evident the velocities between the PCM modules decrease when adding modules to the tank. This is mainly due to the high number of modules in the way of the flow. The smaller velocity profiles between the modules are the main reason for the reduction of the heat transfer coefficient when PCM volume percentage is increased.

The recirculation of the flow is also shown in Figure 45. Figure 45 shows the velocity vectors for 15 and 30% PCM in the tank. For 35% PCM in the tank, the downward velocity vectors at the coil tubes under the modules shows the blocking of the upward flow from the coil by the downward flow from the PCM.

Figure 46 shows the quantity $(hA)_{PCM}$ plotted of PCM volume percentage. From the figure it is evident that the variations of h_{PCM} do not significantly affect the value of hA_{PCM} and the trend of this term is almost completely dominated by the trend of A_{PCM} which is a linear function of the number of modules in the tank.

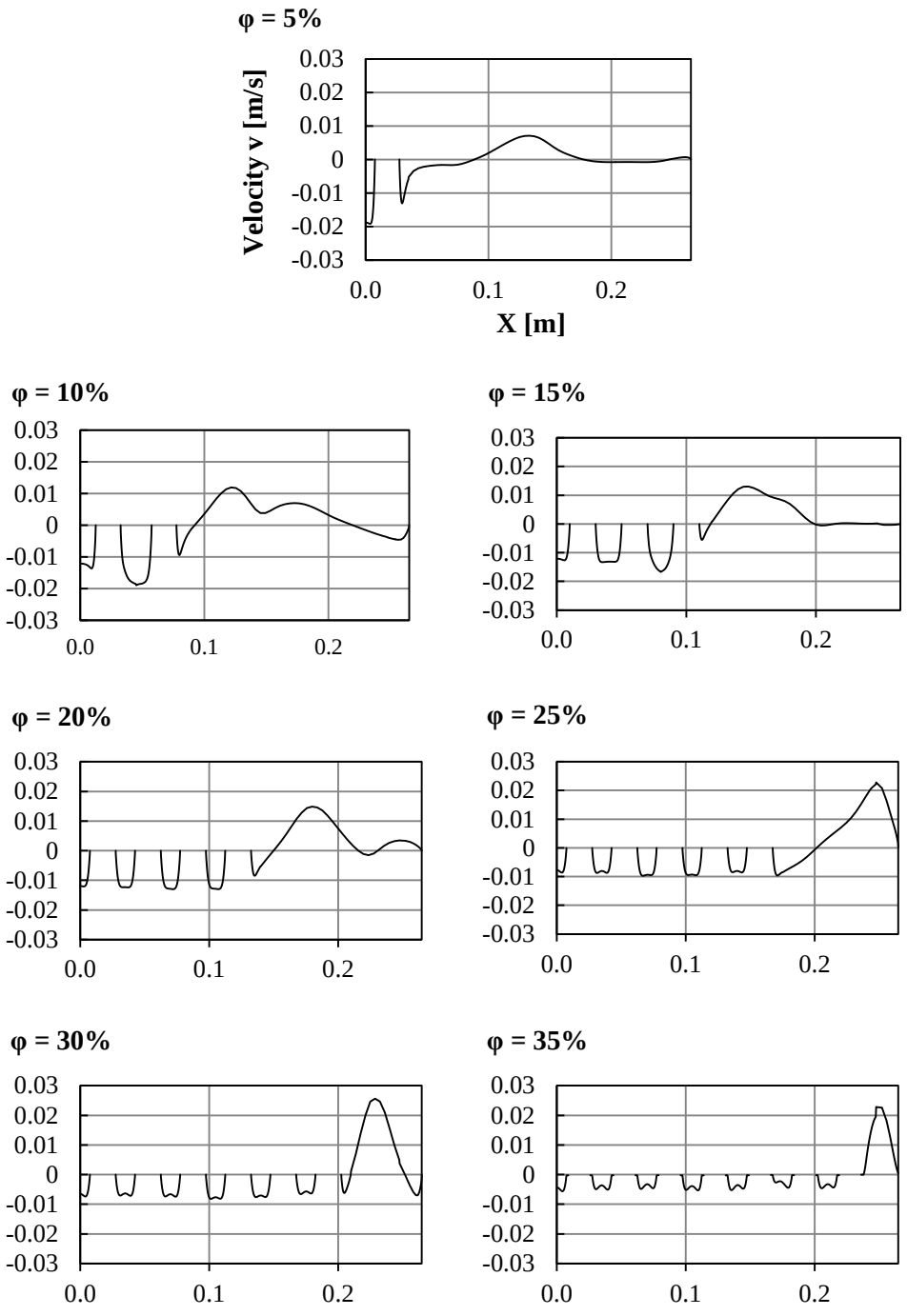

Figure 44-Velocity profile at the mid-height of the tank for different PCM volume percentages

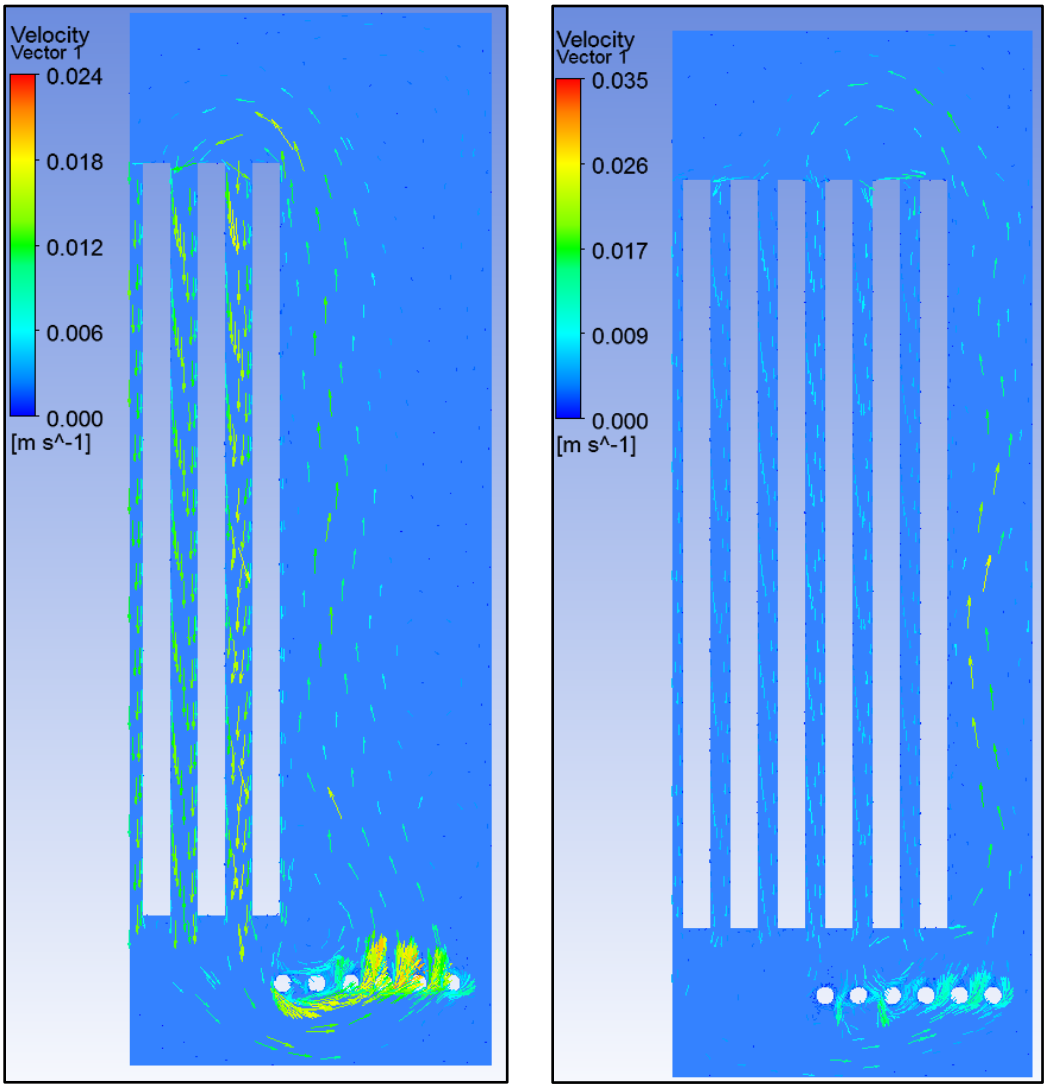

Figure 45- Velocity vectors in the models with 15 and 35%PCM show recirculation of the flow in the tank

Figure 46 also shows that the estimation of $hA_{PCM} = 1200\ W/K$ for 25% PCM in the tank used in the analytical analysis presented in chapter 3 is not unrealistic and values of even more than that can be achieved by adding more PCM modules in the tank.

In summary, it can be concluded that the plates should be kept $2\delta_L$ apart. The module heat transfer coefficients are a weak function of the PCM volume percentage, and since A_{PCM} is a strong linear function of the PCM volume percentage, hA_{PCM} is basically linear.

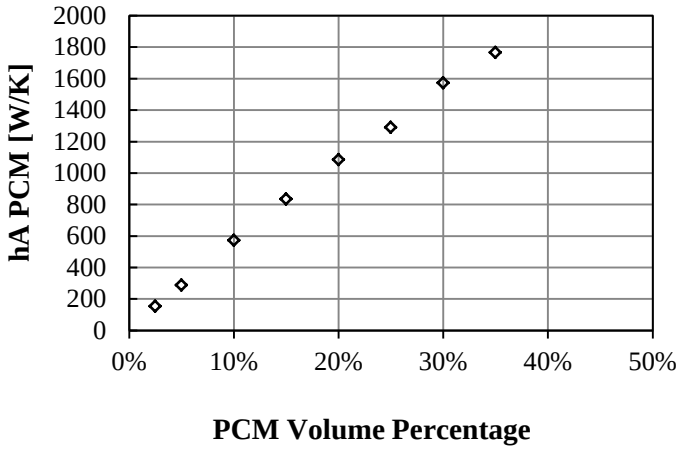

Figure 46-Variations of hA_{PCM} versus PCM volume percentage in the tank

5.3. Coil Heat Transfer Coefficient

Coil heat transfer coefficients calculated from the simulations is compared to the ones calculated from the experimental correlation for laminar natural convection around a fixed temperature horizontal cylinder by McAdams [42] ($Nu = 0.53Ra^{1/4}$) for different PCM volume percentages in the tank is shown in Figure 47. The average of the standard deviations of coil to water heat transfer coefficients for the last 2000 time steps for different PCM volume percentages is $14\ W/m^2K$. The average value of the coil heat transfer coefficient for theses eight models is $651\ W/m^2K$.

Adding PCM modules to the tank decreases water bulk temperature, and therefore increases the ΔT between coil and water. This leads to higher Rayleigh numbers around the coil which in turn increases turbulence and coil heat transfer coefficient. The heat transfer coefficients calculated from the experimental correlations are lower than those calculated from the simulations when there is less than 25% PCM in the tank. This can be explained by the pumping effect discussed in the previous section.

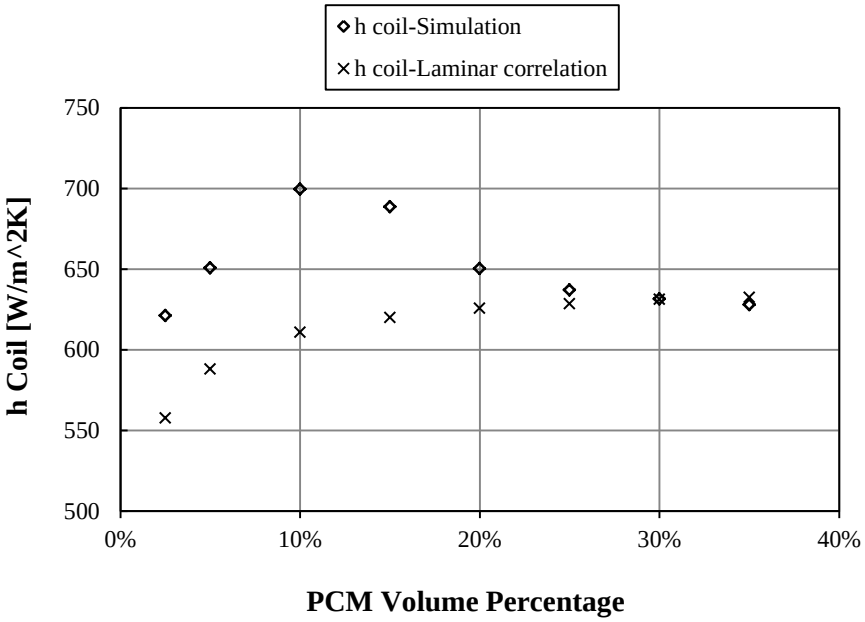

Figure 47-Variations of coil heat transfer coefficient with PCM volume percentage in the tank

Figure 47 shows that the coil heat transfer coefficient increases until 10% PCM, but after that by adding more modules, it decreases. The reason behind this can be explained by looking at the velocity profiles around the coil. The velocity profiles on a line passing through the coil at $(y = 0.06\,m)$ for 5 to 35% PCM is given in

Figure 49. Figure 49 shows how the recirculation is happening around the coil. Water is going upward from the coil and downwards at the center of the tank (at the symmetry line). The velocity profiles in this figure show that adding modules to the tank interferes with the flow from the coil. This interference as discussed before is evident in Figure 45 which shows geometry and velocity vectors for 15% and 35% PCM in the tank. In this figure, the flow from the first few coils from the left shows zeroed to even negative velocities. This results in a reduction of the coil heat transfer coefficient for the part of the coil that is placed directly under the PCM modules. Figure 48 compares the average coil heat transfer coefficient for the first and the last three tubes in a tank with 20% PCM. The first three tubes in this figure are located under PCM modules and show lower heat transfer coefficients in comparison to the last three modules.

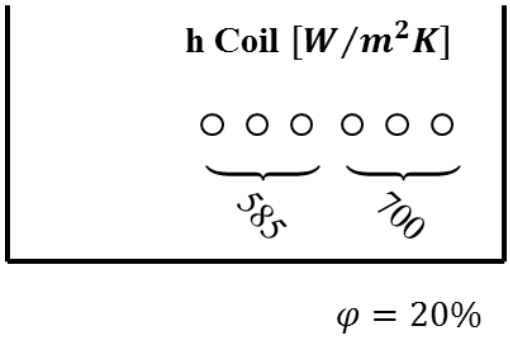

Figure 48-Coil heat transfer coefficients for 20% PCM in the tank

The coil surface area is constant. Therefore $(hA)_{coil}$ follows the same trend as h_{coil}. The variations of $(hA)_{coil}$ versus PCM volume percentage in the tank is given in Figure 50. Figure 50 shows that the variations in h_{coil} has changed the value of $(hA)_{coil}$ by 12%.

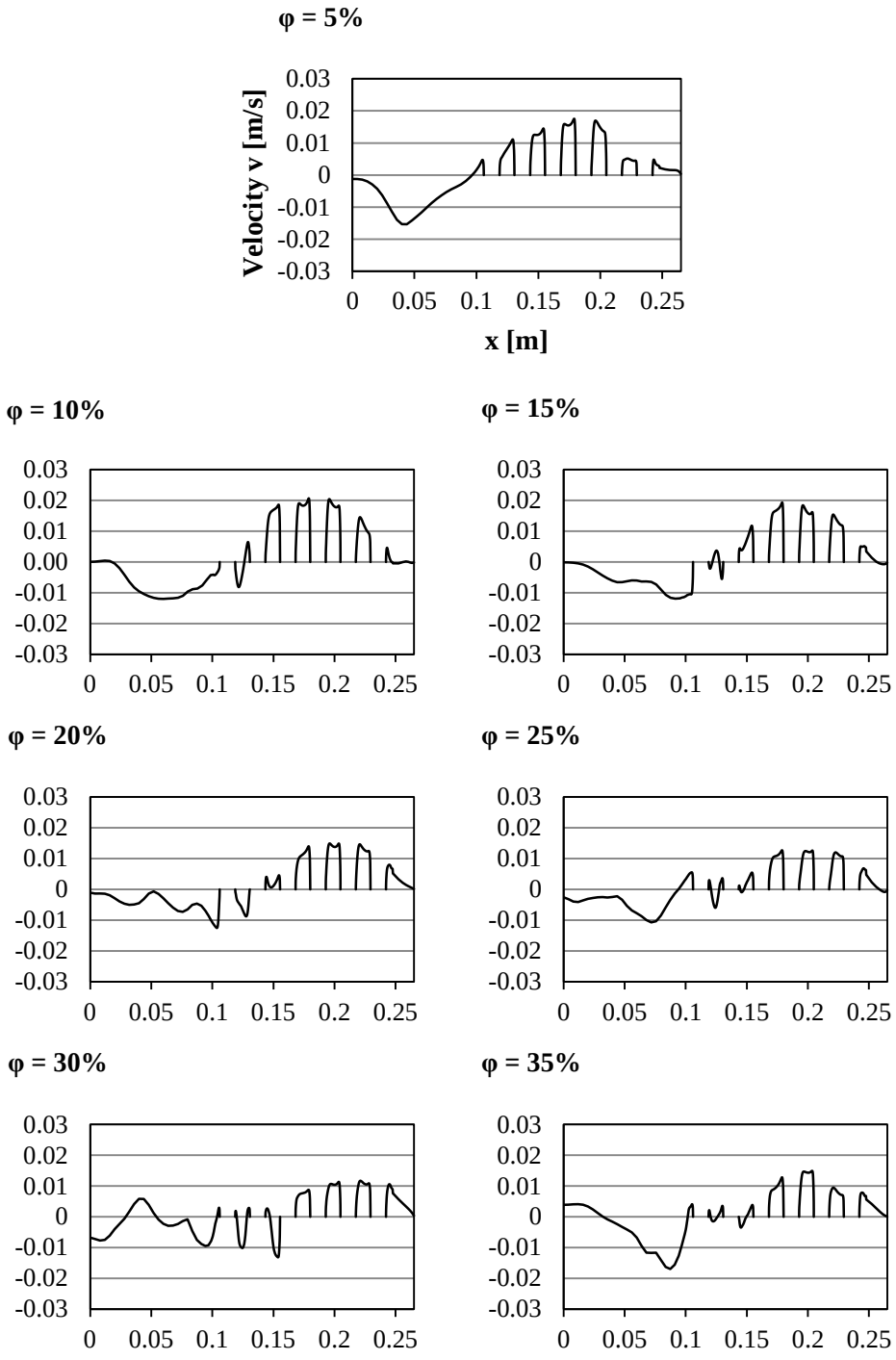

Figure 49-Velocity profiles on a line passing through the coil at ($y = 0.06\ m$) for 5 to 35% PCM in the tank

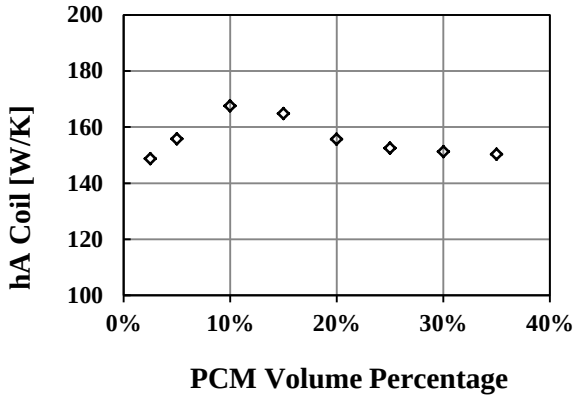

Figure 50-Variations of hA_{Coil} versus PCM volume percentage in the tank

5.4. Charge Rate of the System

From the previous sections, it is realized that both $(hA)_{PCM}$ and $(hA)_{coil}$ are changing with PCM volume percentage, and therefore they both influence the charge rate of the system.

The total amount of the heat transfer rate from water to the PCM modules calculated from the two dimensional models is transformed to estimate that of the three dimensional rectangular tank by accounting for the other side of the symmetry line as well as the depth of the tank. Figure 51 shows this parameter versus the PCM volume percentage in the tank. This figure gives us very interesting information on the heat transfer behavior of the system when PCM modules are added to the tank. As observed from the figure, when adding PCM modules to the system the heat transfer rate to the PCM increases, until we reach a PCM volume percentage of 15%. After that, by adding PCM modules to the tank,

the heat transfer to the PCM neither increases nor decreases, but stays constant. This means that for more than 15% PCM in the tank, the speed of charging is independent of the PCM volume percentage, and adding PCM modules will only increase the heat capacity of the system.

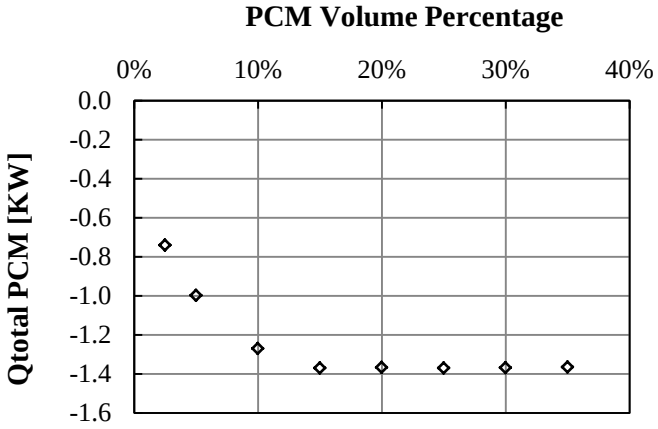

Figure 51-Total heat transfer rate from water to the PCM in the three dimensional tank versus PCM volume percentage

Considering equation (22), $(T_{Coil} - T_{PCM})$ is constant. Therefore the trend of the heat transfer rate to the PCM is governed by $(hA)_{tot}$. If we write $(hA)_{tot}$ in the form of:

$$(hA)_{tot} = \frac{(hA)_{coil}}{\frac{(hA)_{coil}}{(hA)_{PCM}} + 1} \tag{27}$$

It is realized that as $(hA)_{PCM}$ gets bigger, $\frac{(hA)_{coil}}{(hA)_{PCM}}$ becomes smaller, and therefore the denominator gets closer to one, which means that the value of $(hA)_{tot}$ will be dominantly controlled by $(hA)_{coil}$ and therefore becomes independent of the

PCM volume percentage. Calculating the values of $\frac{(hA)_{coil}}{(hA)_{PCM}}$ for different PCM volume percentages, it is realized that after 15%, the value of this fraction is less than 0.2. This is the main reason that the charge rate of the system remains constant after 15% in Figure 51. From the above equation it is realized that the theoretical maximum charge rate of this system is $\dot{Q} = (hA)_{coil}(T_{Coil} - T_{PCM})$ which in this case is $1.55 \pm 0.2\ KW$.

6. The Effect of the Surface Temperatures of PCM and Coil on the Heat Transfer Characteristics of the Flow

In the previous section it was concluded that for high PCM surface areas, hA_{PCM} becomes very large, and therefore the charge rate of the system is controlled by the coil, and becomes independent of the PCM volume percentage. However, this is only the case when the PCM surface temperature remains at its melting point. Therefore we need to investigate how PCM surface temperature can affect PCM and coil heat transfer coefficients and water bulk temperature.

This study is especially important, because increasing the number of PCM modules in the tank, and having the same charging rate, means less heat transfer rate to each module. This will lead to a slower increase in PCM surface temperature and consequently less reduction in heat transfer rate to the PCM due

to super heating. Therefore, in reality, the charging rate for different PCM volume percentages in the tank can be different.

This part of the investigation first focuses on the effect of PCM and coil surface temperatures on water bulk temperature, and then, studies the changes in PCM heat transfer coefficients with the temperature difference between PCM and water. Different scenarios studied are given in Table 13. These scenarios are performed on two different PCM volume percentages of 2.5% and 35% in the tank.

Table 13- PCM and coil surface temperatures in the models leading to the Nusselt number correlation

Model	PCM Volume Percentage	T_{PCM} $[K]$	T_{Coil} $[K]$	ΔT $[K]$
a	2.5%	295	305	10
i	2.5%	299	305	6
j	2.5%	301	305	4
k	2.5%	290	310	20
h	35%	295	305	10
l	35%	299	305	6
m	35%	301	305	4

6.1. Water Bulk Temperature

In order to study the variations of water bulk temperature, the variations of $(\bar{T}_w - T_{PCM})$ with $(T_{Coil} - T_{PCM})$ for different cases were studied and shown in Figure 52.

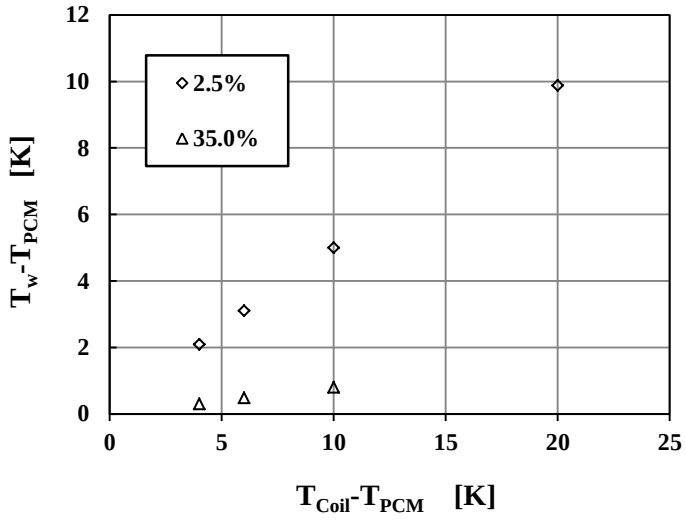

Figure 52-Temperature difference between water and PCM versus temperature difference between Coil and PCM for 2.5% and 35% PCM volume percentage

The behavior is linear which means that for a specific PCM volume percentage in the tank the value of $\theta_w = \frac{\bar{T}_w - T_{PCM}}{T_{Coil} - T_{PCM}}$ is independent of PCM and coil temperatures. Moreover, since $\theta_w = \frac{1}{1+\frac{(hA)_{PCM}}{(hA)_{coil}}}$, changing the PCM and coil temperatures will not change the value of $\frac{(hA)_{PCM}}{(hA)_{coil}}$.

6.2. PCM Heat Transfer Coefficient

Since Rayleigh number in the tank is close to 10^9, the flow in the tank is expected to be transitional. The Nusselt numbers calculated through the simulation for the PCM modules under this study are expected to be between the Nusselt numbers calculated from the turbulent and laminar correlation for fixed temperature vertical flat plates. Based on the experimental data for natural convection flow

along a fixed temperature vertical flat plate [49][50] and [51] , for laminar and turbulent flows, Nusselt number is related to Raleigh number with the following correlations:

$$\text{For Laminar flow: } \mathrm{Nu} = 0.59 \times \mathrm{Ra}^{1/4} \tag{27}$$

$$\text{For Turbulent FLow: } \mathrm{Nu} = 0.10 \times \mathrm{Ra}^{1/3} \tag{28}$$

Figure 53 shows Nusselt number versus Rayleigh number for the PCM module for the simulation with the lowest PCM volume fraction ($\varphi = 2.5\%$). As it is shown in the figure, the Nusselt number of the PCM modules are between those calculated from the laminar and turbulent correlations. This further supports the transitional behavior of the flow.

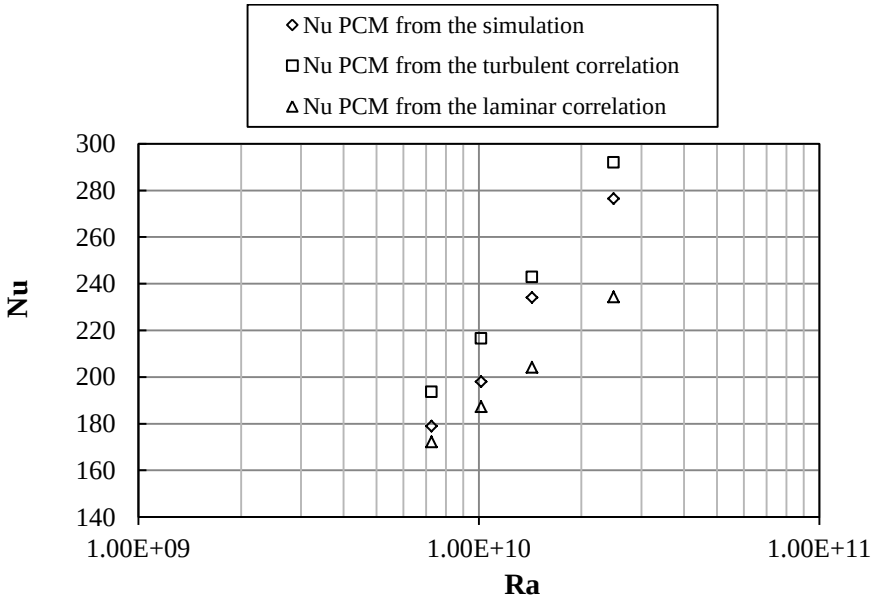

Figure 53-PCM Nusselt number from the simulation, laminar correlation and turbulent correlation versus PCM Rayleigh number for a single PCM module in the tank

As it is evident from the figure, the first two models with lower Rayleigh numbers have Nusselt numbers close to those calculated from the laminar correlation, whereas the last two models have Nusselt numbers closer to the one calculated from the turbulent correlation. Figure 53 is an evidence for the transitional behavior of the flow.

6.3. Coil Heat Transfer Coefficient

Based on the experimental data for natural convection around a fixed temperature horizontal cylinder [42], for laminar flow, Nusselt number is related to Raleigh number with the following correlation:

$$\text{For Laminar flow: } \mathrm{Nu} = 0.53 \times \mathrm{Ra}^{1/4} \qquad (30)$$

Figure 54 shows Nusselt number versus Rayleigh number for the coil for the cases studied. The values of Nusselt numbers from the simulation are higher that the values suggested by the correlation for laminar natural convection flow around a horizontal cylinder. This can be explained by the circulation of flow driven by natural convection over PCM modules in the tank. The heat transfer in the tank around the coil is not driven only by natural convection but is also driven by forced convection through the flow created by PCM modules.

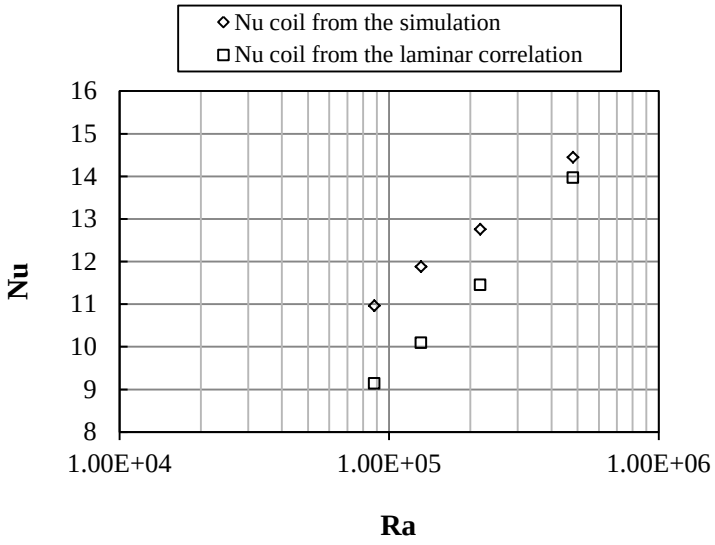

Figure 54-Coil Nusselt number versus coil Rayleigh number for a single PCM module in the tank for 2.5% PCM in the tank

6.4. Charge Rate of the System

The heat transfer rate to the PCM (charge rate of the system) for four models with 2.5% PCM and different PCM and coil temperatures is plotted versus the temperature difference between the coil and the PCM, Figure 55. This figure shows that the variations in the PCM and coil heat transfer coefficients due to changes in PCM and coil temperatures, have barely any effect on the trend of the heat transfer rate of the system, and the trend of this parameter is almost completely dominated by $(T_{Coil} - T_{PCM})$. This means that variations in $(hA)_{tot}$ due to changes in PCM and coil temperatures, has barely any effect on the trend of the charge rate of the system.

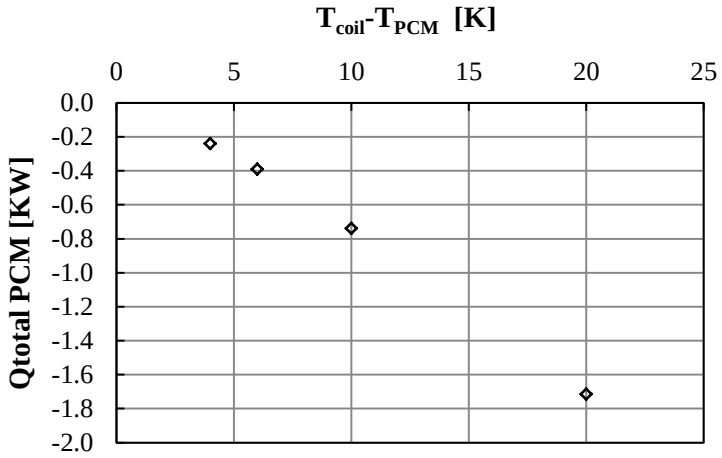

Figure 55-PCM heat transfer rate versus temperature difference between coil and PCM for 2.5% PCM in the tank

CHAPTER 6 Conclusions and Recommendations for Future Work

1. Conclusions

Phase change materials have a high potential to reduce the size of thermal storage systems. However, innovative design of the systems containing these materials is necessary due to the specific characteristics of these materials. Phase change materials exhibit a high thermal capacity due to their latent heat of fusion which corresponds to a very short range of temperature, and outside that range they show a relatively small heat capacity. This characteristic of phase change materials is problematic since thermal storage systems usually work on a wide

temperature range. However, researchers reported that using several types of PCMs in the system, called cascaded latent heat storage system, can enhance both heat capacity and exergy efficiency of the system dramatically.

It has been shown by Mather et al. [6] that one of the best ways of connecting the tanks is to charge and discharge the tanks indirectly (using coils at the bottom and top of the tanks) in series.

The idea was to use a multi-tank system in series, each of which contains a specific type of PCM. This way, since each tank in a multi-tank system works in a specific narrow temperature range.

Through a lumped system model created for a single tank having a coil at the bottom and PCM modules inside and coding it in FORTRAN, it was shown that the lower the temperature range in which the tanks operate, the higher the gain in heat capacity. This further supports the idea of using different PCMs in different tanks of a multi-tank system.

It was also found out that the higher the term hA of the PCM (h being the heat transfer coefficient of water to PCM modules and A being the surface area of the PCM modules) the faster the system charges. The plots from the code showed that the thermal behavior of the system is highly sensitive to hA of the PCM. Therefore, maintaining a high hA for the modules is necessary to maintain a high charge rate.

After studying the lumped system model, it was concluded that it is essential for us to optimize the geometry and configurations of the PCM modules in the tank in

order to design a successful and efficient multi-tank system. Thus, the heat transfer characteristics of different PCM module geometries and configurations were studied using computational fluid dynamics.

The geometry of the cylindrical tanks used by Mather et al. was transformed to a rectangular tank with the same volume, height and coil surface area. Then a very thin vertical slice of this tank was simulated in a CFD commercial code (ANSYS CFX). The model used was two dimensional.

Reviewing the studies on PCM module geometries used by researchers, and considering the geometry and conditions of the tank under study, flat plate PCM modules were chosen. A set of CFD validations were performed to ensure that the results of the code are compatible to previous experimental investigations.

Studying the lumped system model, it was concluded that when PCM modules are undergoing phase change, the state of the system is steady. Therefore, we decided to model the system when the PCM modules are changing phase. In the models, the coil and PCM modules were set to be fixed temperature no slip walls, where PCM modules where at their melting point. The models studied were tested for mesh independencies.

The first study was performed on the effect of the gap between the modules on the heat transfer characteristics of the flow in the tank. It was concluded that for bigger than 1.5 centimeter the boundary layers of the modules do not interfere with each other and therefore, the heat transfer characteristics of the flow such as module heat transfer coefficient remain nearly constant.

A second study was performed to investigate the effect of PCM volume percentage on the heat transfer characteristics of the flow. It was found that the dimensionless water bulk temperature decreases when PCM volume percentage is increased. This was due to higher PCM surface area in comparison to that of the coil.

The PCM heat transfer coefficient decreased by 18% for 35% PCM in the tank in comparison to when there was 2.5% PCM in the tank. However for all the cases except the one with a single PCM, the PCM heat transfer coefficient was higher than those calculated by experimental correlations. Considering the fact that the simulations are under-predicting the real heat transfer coefficients, it is probably the case for all simulations. This was because of the "pumping effect" of the flow by the coil in the tank. The overall "hA" of the PCM only varies linearly with the PCM volume percentage, and the reductions in the PCM heat transfer coefficients did not have noticeable effect on the value of "hA" of the PCM.

The coil heat transfer coefficient increased with the PCM volume percentage initially however started to decrease at 10% PCM, where the downward flow from the PCM modules started interacting with the upward flow from the coil. The calculated coil heat transfer coefficients were also higher than those evaluated from the experimental correlations. The overall "hA" coil changed by 12% in comparison to its average value.

The charge rate of the system increased up to 15% PCM in the tank but then when the value of $\frac{(hA)_{coil}}{(hA)_{PCM}}$ became less than 0.2, the value of the charge rate remained

constant which meant that it is being controlled by “hA” of the coil. This means that, for the geometry studied, for more than 15% PCM in the tank, adding modules to the system will only increase the heat capacity of the system, unless the surface area of the coil is increased.

The third study was performed to investigate the effect of the PCM and coil temperature on the heat transfer characteristics of the flow. It was found out that the dimensionless water bulk temperature was independent of the PCM and coil temperatures and was only a function of $\frac{(hA)_{PCM}}{(hA)_{coil}}$. PCM and coil heat transfer coefficients increased by increasing the temperature difference between the coil and the PCM. However their changes did not significantly affect the charge rate of the system, and the charge rate of the system change nearly linearly with the temperature difference between the coil and the PCM.

In summary, changing the gap between the modules will not change the PCM heat transfer coefficient, for gap sizes greater than 1.5 cm. Adding PCM modules to the system increases the charge rate, however beyond 15% PCM in the tank, the charge rate remains constant and adding modules will only increase the heat capacity of the system unless the surface area of the coil is increased. The dimensionless water bulk temperature is only a function of the geometry of the system and is independent of the PCM and coil surface temperatures. The charge rate of the system varies linearly with the temperature difference between the PCM and coil.

2. Recommendations for Future Work

The investigations presented is computational, and although they are tested and validated, still there is a need for experimental validations.

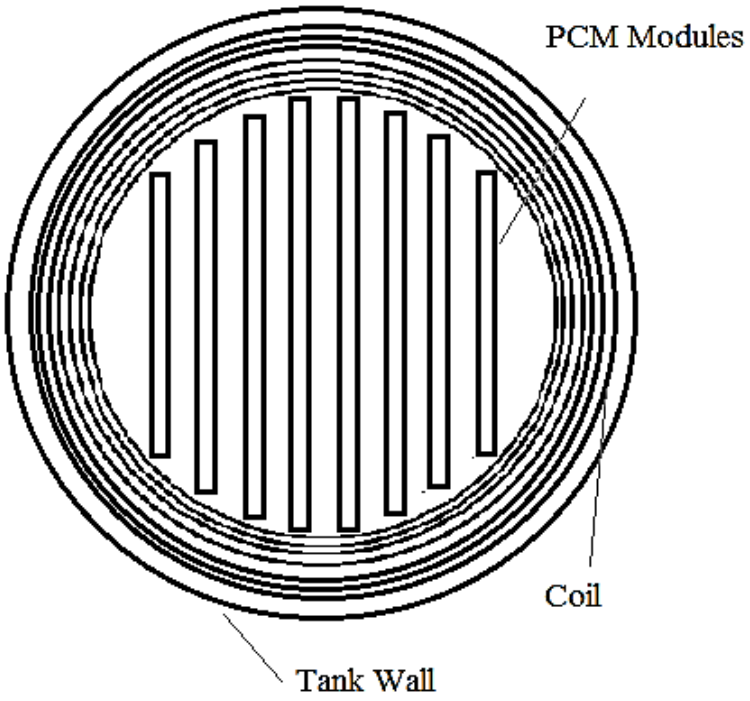

Figure 56-Top view of the proposed configuration of the PCM modules and the coil in a cylindrical tank.

In this study, it was concluded that in order to decrease the interference of the flow from the coil and the PCM it is recommended that the coil is placed around the edges of the tank and the PCM modules are packed in the middle with a minimum gap of $2\delta_L$. The proposed configuration for a cylindrical tank is shown in Figure 56.

Furthermore the heat transfer characteristics of the flow inside the modules should be studied, the resistance of the PCM modules and the super heating of the phase change material at its surface during the charge process should be considered. In this approach, conduction through the PCM as well as convection in the melted region of the module should be studied. Superheating the melted PCM leads to significant reduction in the charging rate of the system, and this is the reason that the geometry should be optimized according to the heat transfer characteristics inside the PCM, too. Also this study is necessary to assess the real charge rate of the system when trying to design the multi tank system.

After thorough investigations of the heat transfer characteristics of the system, and optimizing the geometry of the PCM modules taking into account the heat transfer on the PCM side, the performance of the multi-tank system should be assessed both experimentally and computationally. The PCM volume percentage in each tank, the melting point of the PCMs, the number of tanks in the series, the inlet temperature and eventually the coil design, configuration, orientation and surface area and the volume of the tank should be optimized.

After designing and optimizing the multi-tank system, it is also needed to compare the performance and efficiency of this system to a sensible storage system with the same volume, or capacity in a single or multi-tank configuration.

The final objective of these investigations is to assess the gains of this system over conventional sensible thermal storage systems, or single tank latent heat

storage systems. At the end a design algorithm should be developed with non-dimensional numbers so that the study can be applied to different thermal storage needs with different capacities, working temperatures and requirements.

References

[1] B. Zalba, J. M. Martin, L. F. Cabeza, and H. Mehling. "Review on Thermal Energy Storage with Phase Change: Materials, Heat Transfer Analysis and Applications." *Applied Thermal Engineering* **23** (3), 251- 283 (2003).

[2] A. Sharma, V. V. Tyagi, C. R. Chen, and D. Buddhi. "Review on Thermal Energy Storage with Phase Change Materials and Applications." *Renewable and Sustainable Energy Reviews* **13** (2), 318-345 (2009).

[3] I. Dincer, and M. A. Rosen. *Thermal Energy Storage – Systems and Applications.* ISBN 0-471-49573-5. John Wiley and Sons, Inc., New York, NY (2002).

[4] R. M. Dickinson. "Analysis and Development of Draw Strategies for a Multi-Tank Thermal Storage System for Solar Heating Applications", Master's thesis, Carleton University, Ontario, Canada (2012).

[5] B. Ramlow, B. Nusz. *Solar Water Heating: A Comprehensive Guide to Solar Water and Space Heating Systems.* ISBN 978-0-86571-668-1. New Society Publishers, Gabriola Island, Canada (2011).

[6] D. W. Mather, K. G. T. Hollands, J. L. Wright. "Single- and Multi-tank Energy Storage for Solar Heating Systems: Fundamentals." *Solar Energy* **73**(1), 3-13 (2002).

[7] E. Talmatsky, A. Kribus. "PCM Storage for Solar DHW: An Unfulfilled Promise?" *Solar Energy* **82**, 861-869 (2008).

[8] C. A. Cruickshank, S. J. Harrison. "Analysis of a Modular Thermal Storage for Solar Heating Systems." *Canadian Solar Buildings Conference, Montreal, August 20-24, (2004).*

[9] C. A. Cruickshank, S. J. Harrison. “Thermal Response of a Series- and Parallel-connected Solar Energy Storage to Multi-day Charge Sequences.” *Solar Energy* **85**, 180-187 (2011).

[10] R. M. Dickinson, C. A. Cruickshank, S. J. Harrison. “The Effect of Discharge Configurations on the Thermal Behavior of a Multi-tank Storage System.” *Energy Procedia* **30**, 215-224 (2012).

[11] S. M. Hasnain. “Review on Sustainable Thermal Energy Storage Technologies, Part I: Heat Storage Materials and Techniques.” *Energy Convers. Mgmt* **39**(11), 1127-1138 (1998).

[12] N. Nallusamy, S. Sampath, R. Velraj. “Experimental Investigation on a Combined Sensible and Latent Heat Storage System Integrated with Constant/Varying (Solar) Heat Sources.” Renewable Energy **32**, 1206-1227 (2007).

[13] H. Bjurstrom, B. Carlsson. “An Exergy Analysis of Sensible and Latent Heat Storage.” *Heat Recovery Systems* **5**(3), 233-250 (1985).

[14] F. Agyenim, N. Hewitt, P. Eames, M. Smyth. “A Review of Materials, Heat Transfer and Phase Change Problem Formulation for Latent Heat Thermal Storage Systems (LHTESS).” *Renewable and Sustainable Energy Reviews* **14**, 615-628 (2010).

[15] J. Wei, Y. Kawaguchi, S. Hirano, H. Takeuchi. “Study on a PCM Heat Storage System for Rapid Heat Supply.” *Applied Thermal Engineering* **25**, 2903-2920 (2005).

[16] T. Kousksou, P. Bruel, G. Cherreau, V. Leoussoff, T. El Rhafiki. “PCM Storage for Solar DHW: From an Unfulfilled Promise to a Real Benefit.” *Solar Energy* **85**, 2033-2040 (2011).

[17] S. Jegadheeswaran, S. D. Pohekar, T. Kousksou. “Exergy Based Performance Evaluation of Latent Heat Thermal Storage System: A Review.” *Renewable and Sustainable Energy Reviews* **14**, 2580-2595 (2010).

[18] M. Liu, W. Saman, F. Bruno. “Review on Storage Materials and Thermal Performance Enhancement Techniques for High Temperature Phase Change Thermal Storage Systems.” *Renewable and Sustainable Energy Reviews* **16**, 2118-2132 (2012).

[19] T. Watanabe, A. Kanzawa. “Second Law Optimization of a Latent heat Storage System with PCMs Having Different Melting Points.” *Heat Recovery Systems & CHP* **15**(7), 641-653 (1995).

[20] Z. X. Gong, A. S. Mujumdar. “Thermodynamic Optimization of the Thermal Process in Energy Storage Using Multiple Phase Change Materials.” *Applied Thermal Engineering* **17**(11), 1067-1083 (1997).

[21] H. Cui, X. Yuan, X. Hou. “Thermal Performance Analysis for a Heat Receiver Using Multiple Phase Change Materials.” *Applied Thermal Engineering* **23**, 2353-2361 (2003).

[22] H. Michels, R. Pitz-Paal. “Cascaded Latent Heat Storage for Parabolic Through Solar Power Plants.” *Solar Energy* **81**, 829-837 (2007).

[23] R. V. Seeniraj, N. Lakshmi Narasimhan. “Performance Enhancement of a Solar Dynamic LHTS Module Having both Fins and Multiple PCMs.” Solar Energy 82, 535-542 (2008).

[24] M. Rady. “Thermal Performance of Packed Bed Thermal Energy Storage Units Using Multiple Granular Phase Change Composites.” *Applied Energy* **86**, 2704-2720 (2009).

[25] H. Shabgard, C. W. Robak, T. L. Bergman, A. Faghri. “Heat Transfer and Exergy Analysis of Cascaded Latent Heat Storage with Gravity-assisted Heat

Pipes for Concentrating Solar Power Applications." *Solar Energy* **86**(3), 816-830 (2012).

[26] B. Zalba, J. M. Marin, L. F. Cabeza, H. Mehling. "Review on Thermal Energy Storage with Phase Change: Materials, Heat transfer Analysis and Applications." *Applied Thermal Engineering* **23**, 251-283 (2003).

[27] A. F. Regin, S. C. Solanki, J. S. Saini. "Heat Transfer Characteristics of Thermal Energy Storage System Using PCM Capsules: A Review." *Renewable and Sustainable Energy Reviews* **12**, 2438-2458 (2008).

[28] M. Esen, A. Durmus, A. Durmus. "Geometric Design of Solar-aided Latent Heat Store Depending on Various Parameters and Phase Change Materials." *Solar Energy* **62**(1), 19-28 (1998).

[29] K. A. R. Ismail, R. I. R. Moraes. "A Numerical and Experimental Investigation of Different Containers and PCM Options for Cold Storage Modular Units for Domestic Applications." *International Journal of Heat and Mass Transfer* **52**, 4195-4202 (2009).

[30] J. Fukai, Y. Hamada, Y. Morozumi, O. Miyatake. "Effect of carbon-fibre brushes on conductive heat transfer in phase change materials." *Heat and Mass Transfer* **45**, 4781-4792 (2002).

[31] Y. Hamada, W. Ohtsu, J. Fukai. "Thermal Response in Thermal Energy Storage Material Around Heat Transfer Tube: Effect of Additives on Heat Transfer Rates." *Solar Energy* **75**, 317-28 (2003).

[32] Y. Wang, A. Amiri, K. Vafai. "An Experimental Investigation of the Melting Process in a Rectangular Enclosure." *Heat and Mass Transfer* **42**, 3659-3672 (1999).

[33] R. H. Henze, J. A. C. Humphrey. “Enhanced Heat Conduction in Phase-change Thermal Energy Storage Devices.” *Heat Mass Transfer* **24**, 459-474 (1981).

[34] Z. Liu, X. Sun, C. Ma. “Experimental Investigations on the Characteristics of Melting Processes of Stearic Acid in an Annulus and Its Thermal Conductivity Enhancement by Fins.” *Energy Conversion Management* **46**, 959-969 (2005).

[35] H. El-Dessouky, F. Al-Juwayhel. “The Effectiveness of a Thermal Energy Storage System Using Phase Change Materials.” *Energy Conversion Management* **38**(6), 601-617 (1997).

[36] P. Verma, Varun, S. K. Singal. “Review of mathematical modeling on latent heat thermal energy storage systems using phase-change material.” *Renewable and Sustainable Energy Reviews* **12**, 999-1031 (2008).

[37] A. A. Al-abidi, S. B. Mat, K. Sopian, M. Y. Sulaiman, A. Th. Mohammed. “CFD Applications for Latent Heat Thermal Energy Storage: A Review.” *Renewable and Sustainable Energy Reviews* **20**, 353-363 (2013).

[38] G. De Vahl Davis, I. P. Jones. “Natural Convection in a Square Cavity: a Comparison Exercise.” *International Journal of Numerical Methods in Fluids* **3**, 227-XXXX (1983).

[39] F. Ampofo, T. G. Karayiannis. “Experimental Benchmark Data for Turbulent Natural Convection in an Air Filled Square Cavity.” *International Journal of Heat and Mass Transfer* **46**, 3551-3572 (2003).

[40] J. P. Holman. *Heat Transfer* 10th ed., New York: McGraw-Hill, ISBN 978-0-07-352936-3 (2010).

[41] S. Ostrach. “An Analysis of Laminar Free Convection Flow and Heat Transfer about a Flat Plate Parallel to the Direction of the Generating Body Force.” *National Advisory Committee for Aeronautics, Report 1111, 1953.*

[42] W. H. McAdams. *Heat Transmission*, 3d ed., New York: McGraw-Hill, 1954.

[43] S. W. Churchill, H. H. S. Chu. "Correlating Equations for Laminar and Turbulent Free Convection from Vertical Plate." *International Journal of Heat Mass Transfer* **18**, 1323-XXX, 1975.

[44] V. T. Morgan. "The Overall Convective Heat Transfer from Smooth Circular Cylinders." In T. F. Irvine and J. P. Hartnett, Eds., *Advances in Heat transfer* **11**, Academic Press, New York, 199-264 (1975).

[45] S. W. Churchill. "A Comprehensive Correlating Equation for Laminar, Assisting, Forced, and Free Convection." *American Institute of Chemical Engineers Journal* **23**(1), 10-XXX (1977).

[46] ANSYS CFX-Solver Theory Guide, ANSYS CFX Release 11.0, December 2006.

[47] F. R. Menter. "Zonal Two Equation $k-\omega$ Turbulence Models for Aerodynamic Flows." *AIAA*, 93-2906 (1993).

[48] F. R. Menter. "Two-Equation Eddy-Viscosity Turbulence Models for Engineering Applications." *AIAA Journal* **32**(8), 1598-1605 (1994).

[49] C. Y. Warner, and V. S. Arpaci. "An Experimental Investigation of Turbulent Natural Convection in Air at Low Pressure along a Vertical Heated Flat Plate,"*Int. J. Heat Mass Transfer* **11**, 397 (1968).

[50] F. J. Bayley. "An Analysis of Turbulent Free Convection Heat Transfer," *Proc. Inst. Mech. Eng.* **169**(20), 361 (1955).

[51] E. R. G. Eckert, and T. W. Jackson. "Analysis of Turbulent Free Convection Boundary Layer on a Flat Plate," *NACA Rep.* 1015 (1951).

[52] J. Mathieu, and J. Scott. *An Introduction to Turbulent Flow*, New York: Cambridge University Press, ISBN 978-0521-77538-0 (2000).

[53] C. Yaws. *Chemical Properties Handbook*, McGraw-Hill Professional, ISBN 978-0070-3401-2 (1999).

[54] C. Rundle. "Validation of Computational Fluid Dynamics for Atria Geometries." Master's thesis, McMaster University, Ontario, Canada (2009).

[55] S. W. Churchill, and H. H. S. Chu. "Correlating Equations for Laminar and Turbulent Free Convection from a Horizontal Cylinder," *Int. J. Heat Mass Transfer* **18**, 1049 (1975).

Appendix A

CFD Validations

1. Introduction

This section presents the results of a series of validation exercises pertaining to natural convection flows. Both laminar and turbulent cases are considered. A methodical approach was taken in selecting the validation cases. The goal of this study is to assess the capability of the CFD code to predict the important separate effects for the final flow of interest. The commercial CFD code ANSYS CFX 14.0 is used throughout this work.

2. Air Filled Square Cavity

The first set of validation cases was performed on a two dimensional air filled square cavity. The top and bottom of the cavity were set to be adiabatic walls and left and right were defined as fixed temperature walls as shown in Figure 57. Different boundary conditions in CFD modeling used in this are introduced in Appendix B.

The dimensions of the cavity and the temperature difference between the walls were calculated in a way that Rayleigh number is 10^4 and 1.58×10^9 for laminar and turbulent flows respectively, Table 14. The Rayleigh number is defined as:

$$Ra_L = \frac{g\beta(T_H - T_C)L^3}{\nu\alpha} \tag{18}$$

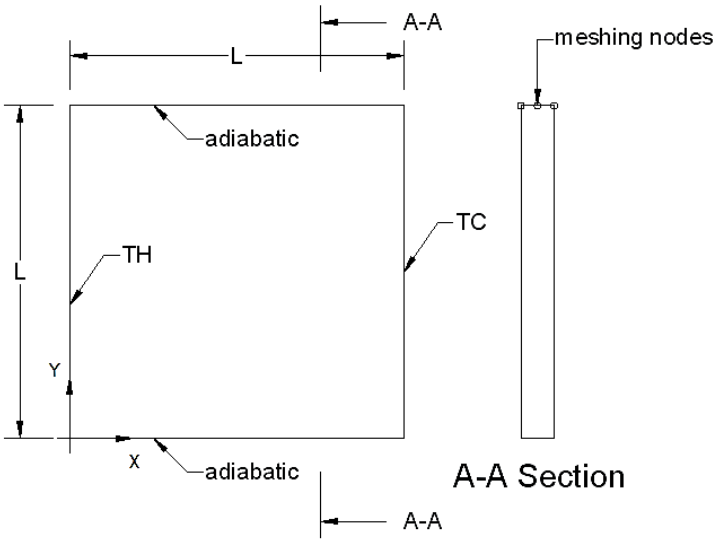

Figure 57-Geometry of air cavity and its boundary conditions for simulation

Table 14-Boundary conditions and dimensions of the air cavity with laminar and turbulent flows

Boundary	Laminar Flow	Turbulent Flow
L	4 cm	75 cm
Top boundary	adiabatic no slip wall	no slip wall (T is a polynomial curve fit of experimental data)
Bottom boundary	adiabatic no slip wall	no slip wall (T is a polynomial curve fit of experimental data)
Right boundary	fixed temperature $TC = 24.196°C$ no slip wall	fixed temperature $TC = 10°C$ no slip wall
Left boundary	fixed temperature $TH = 25.804°C$ no slip wall	fixed temperature $TH = 50°C$ no slip wall
Rayleigh number	10^4	1.58×10^9
Film Temperature	$25°C$	$25°C$

2.1. Laminar Validation

A series of uniform structured grids were applied for this test case. The Nusselt number was calculated and compared to the benchmark provided by De Vahl Davis [38]. As shown in Figure 58 and Table 15, as the grid was refined the predicted Nusselt number was in excellent agreement with the benchmark. Temperature contours are shown in Figure 59.

Table 15-Nusselt numbers calculated for different grid sizes for laminar flow in the square cavity

Number of nodes at the side of the square cavity	Nu number	% Error
20	2.356	5.2%
27	2.302	2.8%
40	2.264	1.1%
80	2.244	0.2%
100	2.242	0.1%
160	2.241	0.0%
200	2.241	0.0%
Benchmark	2.24	-

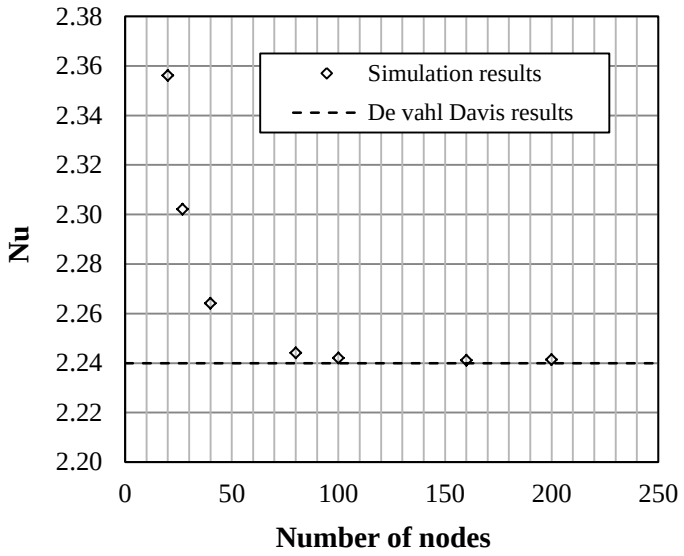

Figure 58-Nusselt number versus number of nodes at the side of the square cavity for laminar flow

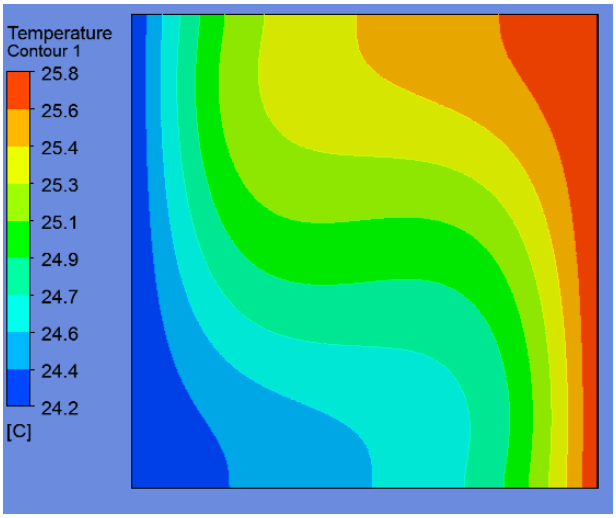

Figure 59-Temperature contours of laminar flow in air cavity

2.2. Turbulent Validation

A non-uniform expanding grid, with a bias factor of 50, was applied for simulation of the turbulent flow case. Grid independence was assessed by increasing the number of nodes from 100 per side to 200 per side. As Rundle [54] reported the $k-\omega$ model showed better predictions of the velocity profiles in the boundary layer region. In this validation case the standard $k-\omega$ turbulence model was applied. The numerical predictions were compared to the experimental results of Ampofo et al. [39]. To maintain the same boundary conditions as the experiment for the horizontal walls of the cavity, a polynomial curve fit, Figure 60, to the temperature data measured at the walls in the experiment was applied as boundary condition of the corresponding walls, Table 16.

Table 16-Polynomial fit in comparison to the benchmark data [39] at the horizontal walls of the cavity

X	$\theta_{top} = \frac{\overline{T} - T_c}{\Delta T}$	Polynomial fit	Error	$\theta_{bot} = \frac{\overline{T} - T_c}{\Delta T}$	Polynomial fit	Error
0.00000	1.0000	0.9658	-3%	1.0000	0.9506	-5%
0.00200	0.9490	0.9618	1%	0.9184	0.942743	3%
0.00667	0.9333	0.9526	2%	0.9038	0.924797	2%
0.01330	0.9342	0.9402	1%	0.8862	0.90026	2%
0.02670	0.9183	0.9168	0%	0.8639	0.853884	-1%
0.05330	0.8782	0.8767	0%	0.7733	0.773483	0%
0.10000	0.8210	0.8229	0%	0.6608	0.66386	0%
0.20000	0.7597	0.7534	-1%	0.5263	0.522176	-1%
0.30000	0.7107	0.7127	0%	0.4520	0.448266	-1%
0.40000	0.6779	0.6788	0%	0.3960	0.398803	1%
0.50000	0.6393	0.6443	1%	0.3503	0.35465	1%
0.60000	0.6135	0.6066	-1%	0.3116	0.311095	0%
0.70000	0.5578	0.5597	0%	0.2722	0.268088	-2%
0.80000	0.4880	0.4851	-1%	0.2214	0.220474	0%
0.90000	0.3372	0.3428	2%	0.1490	0.14823	-1%
0.94670	0.2338	0.2348	0%	0.0938	0.094655	1%
0.97330	0.1409	0.1564	11%	0.0445	0.055026	24%
0.98670	0.1334	0.1114	-16%	0.0352	0.031948	-9%
0.99330	0.1234	0.0878	-29%	0.0272	0.019725	-27%
0.99800	0.0967	0.0704	-27%	0.0185	0.010655	-42%
1.00000	0.0000	0.0628	-	0.0000	0.0067	-

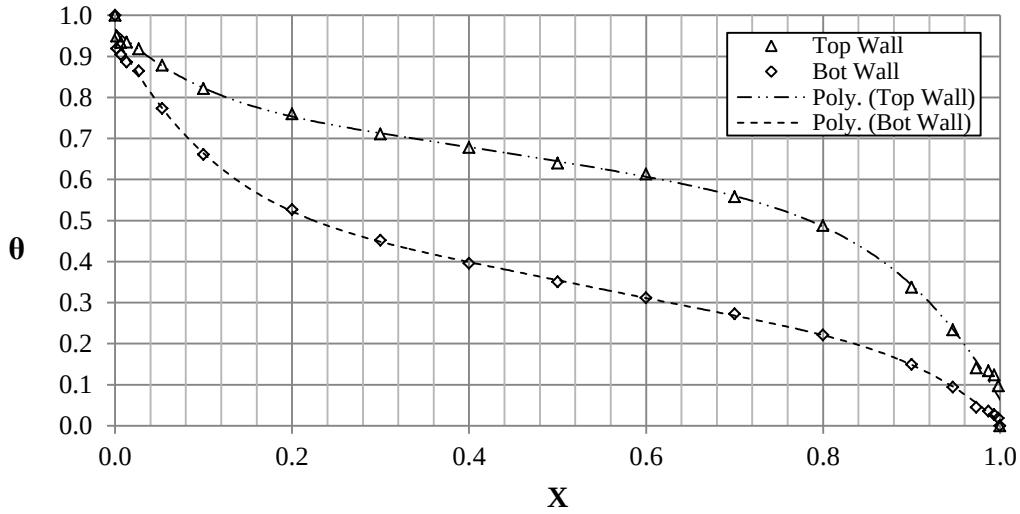

$$\theta_{top} = -8.1372X^5 + 22.285X^4 - 24.217X^3 + 13.08X^2 - 3.9547X + 0.9506$$

$$\theta_{bot} = -7.3772X^5 + 16.934X^4 - 15.765X^3 + 7.3252X^2 - 2.02X + 0.9658$$

Figure 60- Polynomial fit data in comparison to the benchmark data at the horizontal walls of the cavity

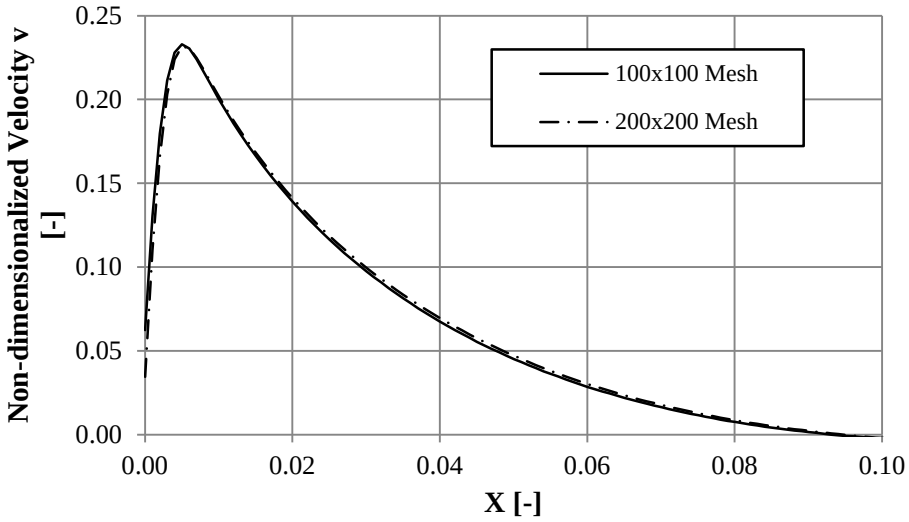

Figure 61-Velocity profiles at the mid-height of the cavity for two different meshes.

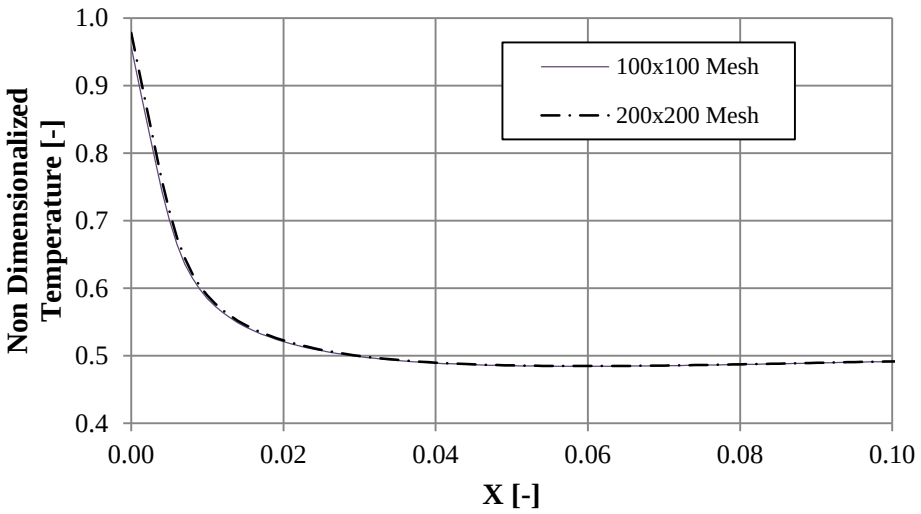

Figure 62-Non-dimensionalized temperature profiles at the mid-height of the cavity for two different meshes

Figure 61 and Figure 62 show a comparison between the non-dimensionalized vertical velocity and temperature profiles at the mid-height horizontal cross section of the cavity for the two different meshes. Vertical velocity is non-dimensionalized by dividing it by buoyancy velocity, V_o. As it is evident, the profiles are nearly identical and therefore the simulation results are grid independent. The Nusselt numbers calculated at the walls of the cavity for different meshes are compared in Table 17.

Figure 63 shows a comparison between the non-dimensionalized vertical velocity profiles of the simulation and the experimental data measured by Ampofo et al. [39] A closer look at the boundary layer region is also shown in Figure 64. These figures show that the velocity predicted by the $k-\omega$ model is in a relatively close agreement with the experimental data. The differences between the temperature polynomial fits used as the boundary conditions of the horizontal

walls and the experimental can also be a reason for the differences between the velocity profiles. It should also be noted that the air properties except the density in ANSYS CFX do not change with local temperatures and remain constant which could be another factor in creating the differences between the simulation and experimental results.

Table 17 -A comparison between the Nusselt numbers calculated at the walls of the cavity for different mesh sizes

Surface	Nu for 100x100 Mesh	Nu for 200x200 Mesh	Error
Hot Wall	51.9	52.6	1.3%
Cold Wall	51.5	52.1	1.2%
Bottom	20.8	20.6	1.0%
Top	20.3	21.1	4.3%

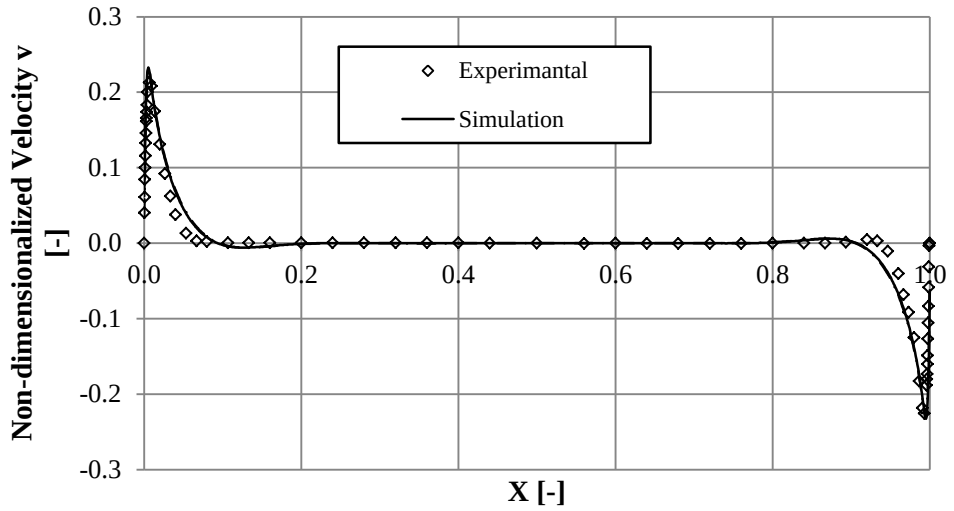

Figure 63-A comparison between non-dimensionalized vertical velocity profiles from the simulation and the experimental data by Ampofo [39] for turbulent flow in a square air cavity

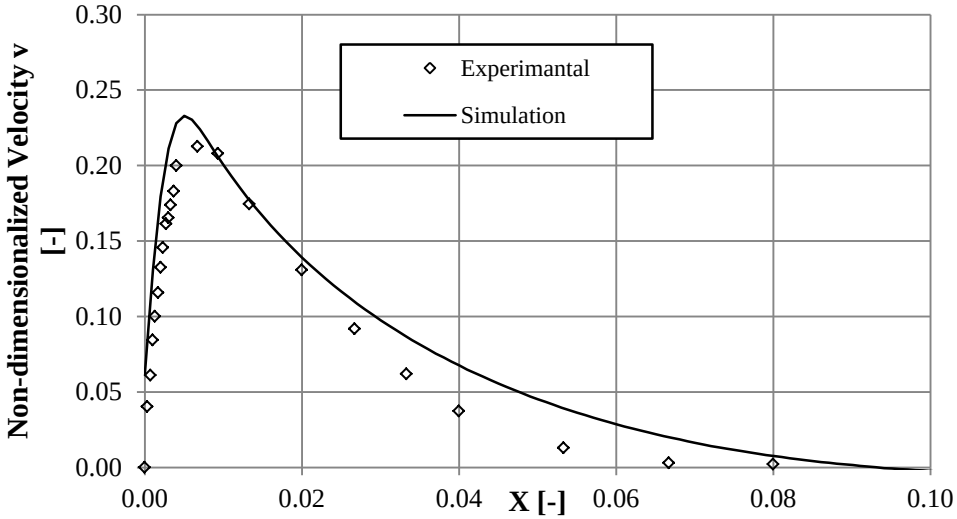

Figure 64- A closer look at the boundary layer region of the non-dimensionalized vertical velocity profiles from the simulation and the experimental data by Ampofo [39]

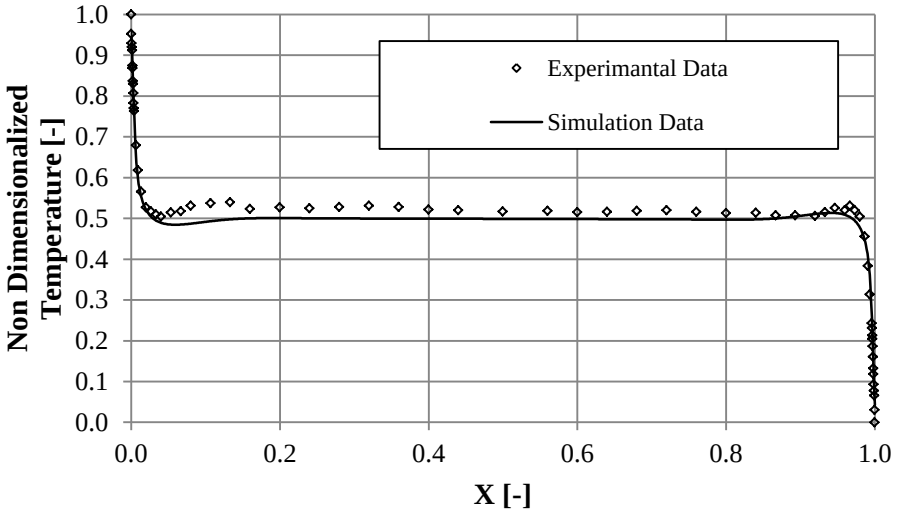

Figure 65-Temperature profile at Y=0.5 in the air cavity with turbulent natural convection flow

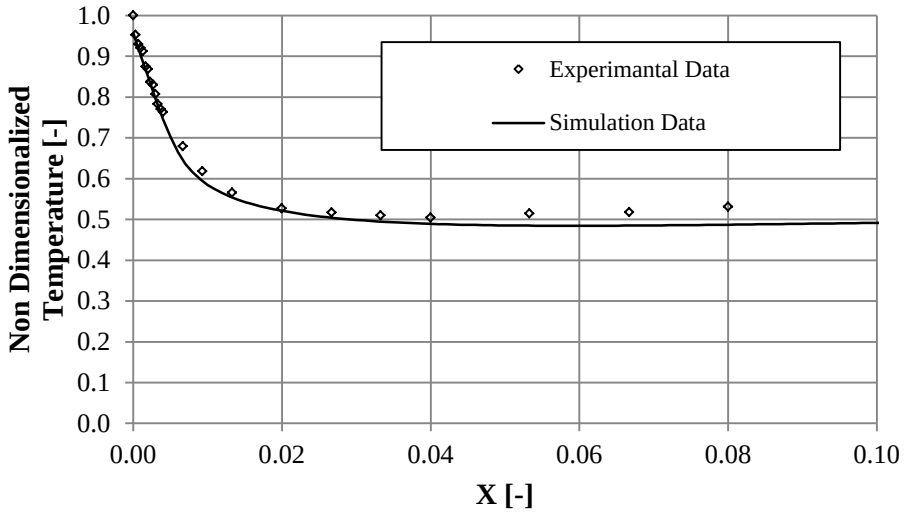

Figure 66-A closer look at the temperature profile at the mid-height of the cavity in the boundary layer region

Figure 65 shows a comparison between the temperature profiles of the simulation and experiment at the mid-height of the cavity. A closer look at the boundary layer region is given in Figure 66. It is evident that the temperature is slightly under-predicted at the mid-height of the cavity. Radiation is not modeled in this study which can be a source of error for low temperatures. However, the overall prediction of the temperature profile is close to the experimental data measured by Ampofo et al.

A comparison between Nusselt numbers at the walls of the cavity from the simulation and the experimental data is also presented in Table 18. The degree of uncertainty in the measured Nusselt numbers from the experimental data is 1.13%. As it is evident the Nusselt numbers are under predicted. Rundle [54] reported that all the turbulence models under-predicted the Nusselt numbers. The

high errors at the horizontal walls are basically due to the differences between the polynomial fit and the experimental data.

Table 18-Average Nusselt number at the walls of the turbulent flow in air cavity

Experimental		**Computational**	
Surface	**Nu**	**Average Nu**	**Error**
Hot Wall	62.9	52.3	16.8%
Cold Wall	62.6	51.8	17.3%
Bottom	13.9	20.5	47.5%
Top	14.4	21.0	45.8%

Temperature contours in the cavity is also shown in Figure 67. It is clear that almost throughout the cavity the temperature rises with the height.

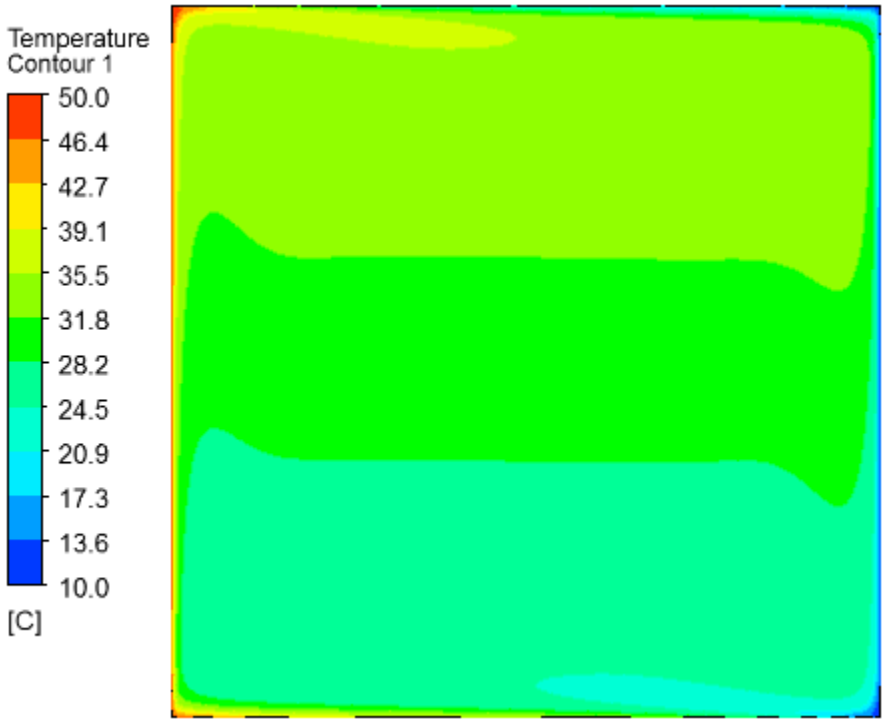

Figure 67-Temperature contours of turbulent flow in air cavity

Turbulence viscosity is shown in Figure 68.

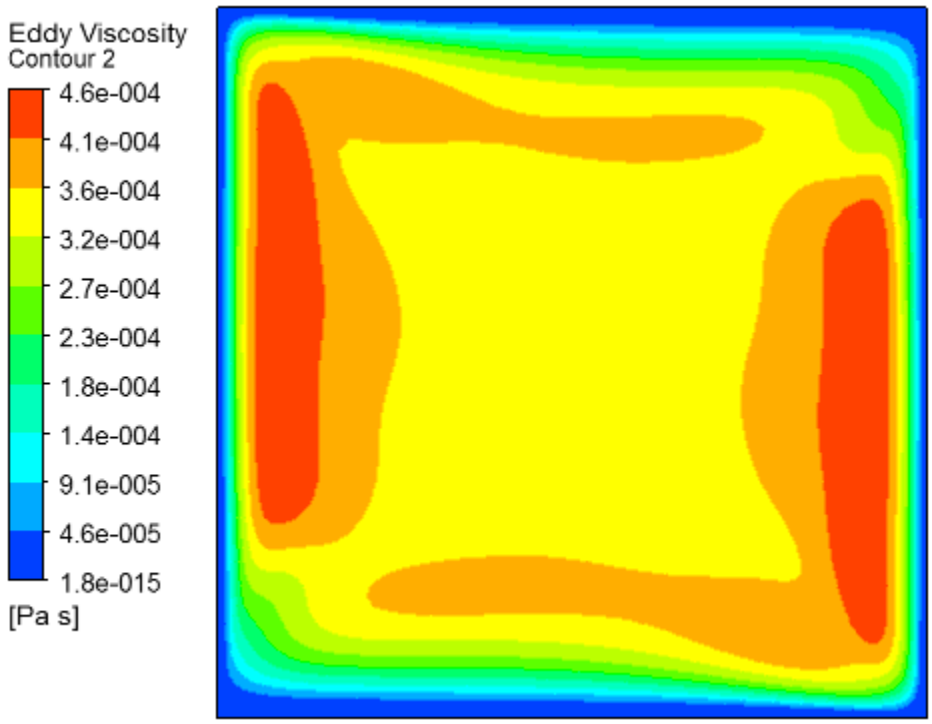

Figure 68-Turbulence viscosity for turbulent flow in air cavity

In the modeling of the validation case presented in the next section, and throughout this study, the SST turbulence model will be used, since it is reported to predict Nusselt numbers closer to the experimental data.

3. Cooled Vertical Flat Plate in an Infinite Environment

The second set of validations was performed for a two dimensional natural convection flow around a cooled vertical flat plate in water for both laminar and turbulent flows. The calculated average heat transfer coefficients for both cases were compared to the ones evaluated from the empirical correlations available in the literature, Appendix C. The geometry of the simulation is shown in Figure 69. The right wall of the domain was set to be a free slip wall and the effect of this

boundary condition was assessed by performing another simulation with the plate located within a larger domain to make sure that the wall is not affecting the results. The plate was assumed to be infinitely thin, and acted as a fixed temperature no slip wall. Table 19 shows the boundary conditions and domain dimensions for laminar and turbulent cases.

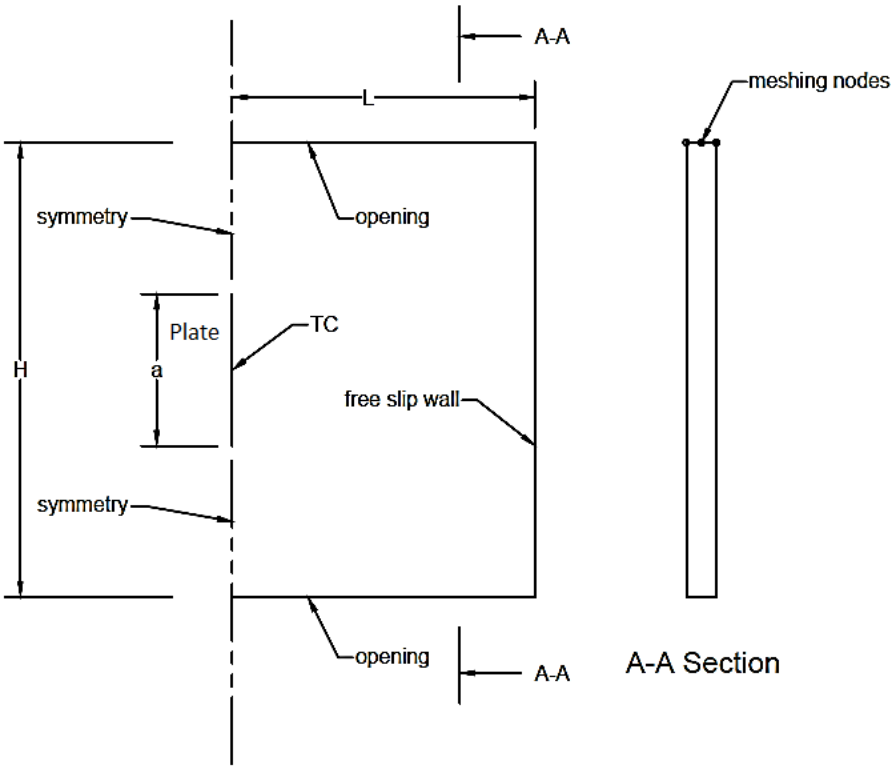

Figure 69-Geometry of cooled flat plate in an infinite environment and its boundary conditions for simulation

The model was meshed using a non-uniform grid. The left side mesh had an inflation factor of 1.03 and the thickness of the first layer adjacent to the wall was set to 0.2 mm and 0.1 mm for laminar and turbulent flow, respectively, to account for the thinner boundary layer. The grid is shown in Figure 70. Grid

independence was assessed by repeating the simulation with a finer grid. Also the dimensions of the geometry were extended in all directions and the results were compared to the previous ones to make sure the dimension of the domain is not affecting the results. For all the simulations with different mesh size and domain dimensions, the profiles for velocity and temperature in the middle of the plate height were essentially identical.

Table 19-Boundary conditions and dimensions of the domain of cooled vertical plate for laminar and turbulent flows

Dimensions	**Laminar Flow**	**Turbulent Flow**
a H L	10 cm 30 cm 20 cm	55 cm 75 cm 100 cm
Boundaries	**Boundary Details**	
Vertical flat plate	Fixed temperature no slip wall $T = 295K$	Fixed temperature no slip wall $T = 295K$
Top boundary	opening with fixed opening pressure $relative\ p = 0.0\ pa,\ T = 305K$	opening with fixed opening pressure $relative\ p = 0.0\ pa,\ T = 305K$
Bottom boundary	opening with fixed opening pressure $relative\ p = 0.0\ pa,\ T = 305K$	opening with fixed opening pressure $relative\ p = 0.0\ pa,\ T = 305K$
Right boundary	adiabatic free slip wall	adiabatic free slip wall
Symmetry	Symmetry	Symmetry
Rayleigh number	2.146×10^8	3.57×10^{10}
Film Temperature, T_f	$25°C$	$25°C$

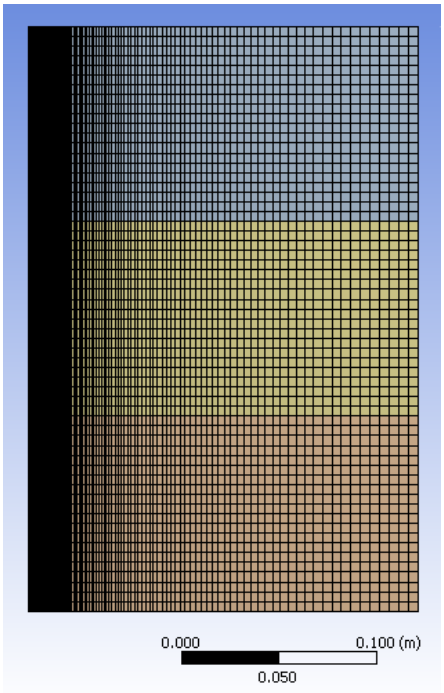

Figure 70- Coarse meshing of the domain for laminar natural convection flow around a cooled vertical flat plate

3.1. Laminar Validation

Heat transfer coefficients calculated from the available correlations for laminar flow are compared to the simulation results in Table 20. The formulas of the correlations used are given in Appendix C. As it is mentioned in Appendix C, the more reliable correlations are A, and B, which are in a very close agreement with the one evaluated from the simulation (less than 2% error).

For the laminar case, analytical velocity and temperature profiles from Ostrach [41] were compared with the simulation results in Figure 71 and Figure 72. Since Ostrach did not have results for Prandtl number equal to 5.83 which is our case for water, another simulation was performed by changing the Prandtl

number to 10. As it is shown in the figures, the profiles of the simulation agree very well with the analytical profiles from Ostrach [41].

Table 20-Comparison between the Nusselt numbers calculated computationally and from the experimental correlations for laminar natural convection around vertical flat plate (for the correlation formulas please see Appendix C)

Correlation	***Ra* number range that correlations are applicable for**	**Nusselt Number** $Ra = 2.146 \times 10^8$
A [42]	$10^4 \leq Ra \leq 10^9$	71.4
B [43]	$Ra \leq 10^9$	74.1
C [43]	$10^{-1} \leq Ra \leq 10^{12}$	93.9
Simulation	-	74.1

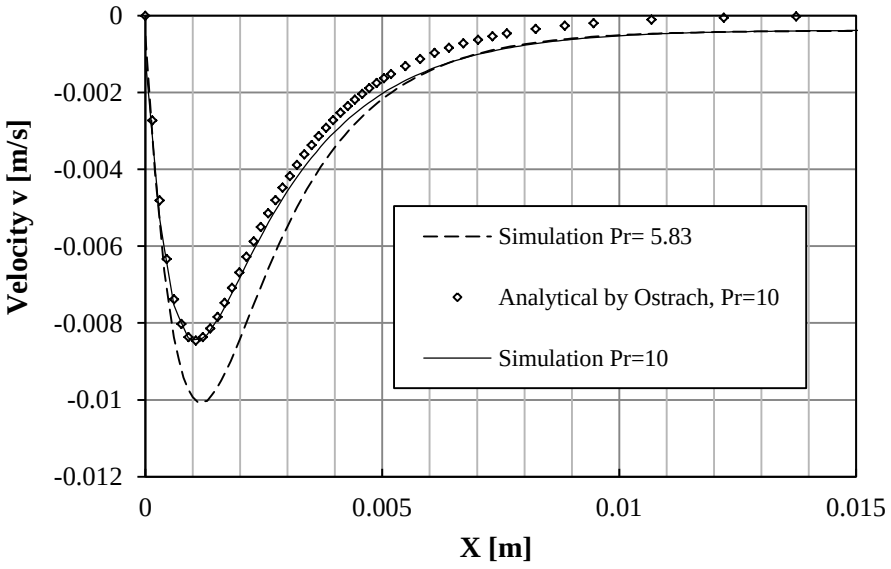

Figure 71-Comparison of velocity profiles at Y=H/2 by Ostrach [41] and simulation results for laminar natural convection around a vertical plate

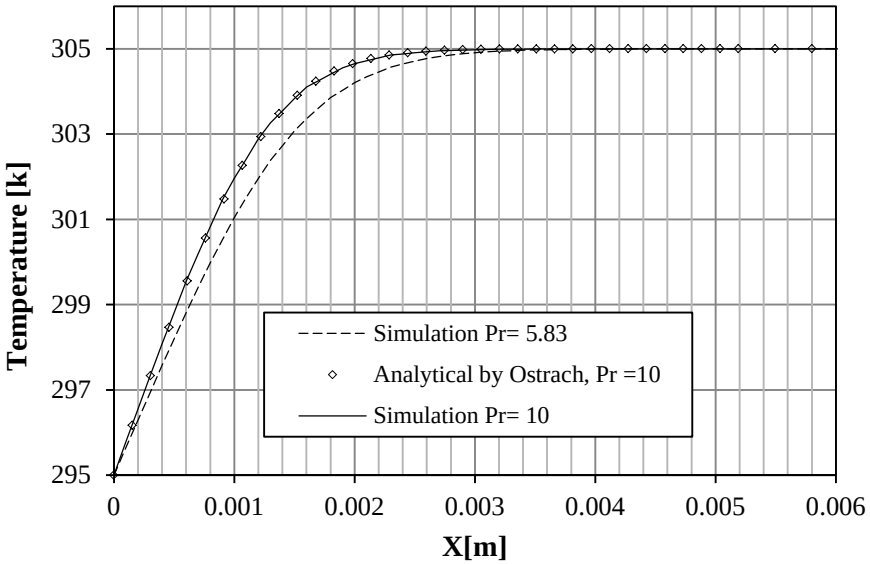

Figure 72-Comparison of temperature profiles at Y=H/2 by Ostrach [41] and simulation results for laminar natural convection around vertical plate

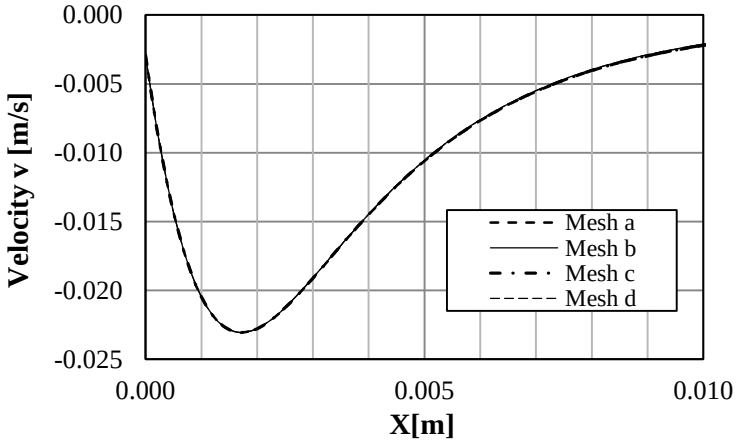

Figure 73-Velocity profile at Y=H/2 for different mesh sizes for turbulent natural convection around vertical plate

3.2. Turbulent Validation

For turbulent validation, the SST model was used. To confirm mesh independence of the results, the velocity and temperature profiles at the mid-height of the plate for four different mesh sizes are shown in Figure 73 and Figure 74. The details of different meshes are given in Table 21.

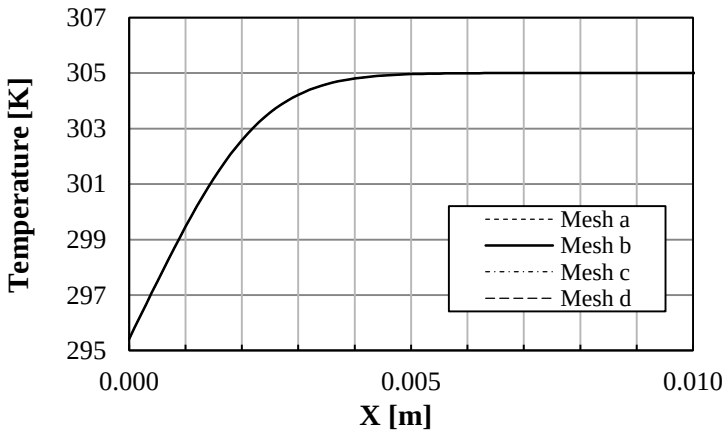

Figure 74-Temperature profile at Y=H/2 for different mesh sizes for turbulent natural convection around vertical plate

Table 21-Different mesh sizes for turbulent natural convection around cooled vertical plate

Mesh	Domain dimensions	Grid size	Total number of nodes
A	L=140 cm H=105 cm	X Dir. 5 mm Y Dir. 5 mm Z Dir. 5 mm	~200000
B	L=100 cm H=75 cm	X Dir. 3 mm Y Dir. 5 mm Z Dir. 5 mm	~200000
C	L=100 cm H=75 cm	X Dir. 5 mm Y Dir. 3 mm Z Dir. 5 mm	~225000
D	L=100 cm H=75 cm	X Dir. 5 mm Y Dir. 5 mm Z Dir. 5 mm	~125000

The heat transfer coefficients calculated from the available correlations for turbulent natural convection flow around a fixed temperature vertical plate are compared to the simulation results in Table 22. It is mentioned in the Appendix C,

that the most reliable correlation is correlation E. As it was expected the evaluated Nusselt number from the simulation is under-predicted. The error is 22%.

Table 22- Comparison between the Nusselt numbers calculated computationally and from the experimental correlations for turbulent natural convection around vertical flat plate for the correlation formulas please see Appendix C)

Correlation	$\boldsymbol{Ra}$ **number range that correlations are applicable for**	**Nusselt Number for** $\boldsymbol{Ra} = 3.57 \times 10^{10}$
C [43]	$10^{-1} \leq Ra \leq 10^{12}$	467.3
D [51]	$10^{9} \leq Ra \leq 10^{13}$	349.4
E [49], [50]	$10^{9} \leq Ra \leq 10^{13}$	329.3
Simulation	-	255.7

4. Heated Horizontal Cylinder in an Infinite Environment

The final validation study considered two dimensional natural convection around a heated horizontal cylinder in water, and the calculated average Nusselt number was compared to empirical correlations available in literature. The geometry of the simulation is shown in Figure 75. The cylinder is set to a fixed temperature no slip wall. The diameter of the cylinder is the same as the one of the coil which is considered in the thermal storage tank simulations. Table 23 shows the boundary conditions and their corresponding parameters.

The grid is shown in Figure 76. The mesh in the vicinity of the cylinder was inflated with an inflation factor of 1.03, with the first layer starting at 0.1 mm thickness to account for the large gradients within the boundary layer. The model was also simulated with finer grids to assure the results are grid independent. Also

the dimensions of the domain were extended and the results were compared to make sure that the dimensions of the domain are not affecting the results.

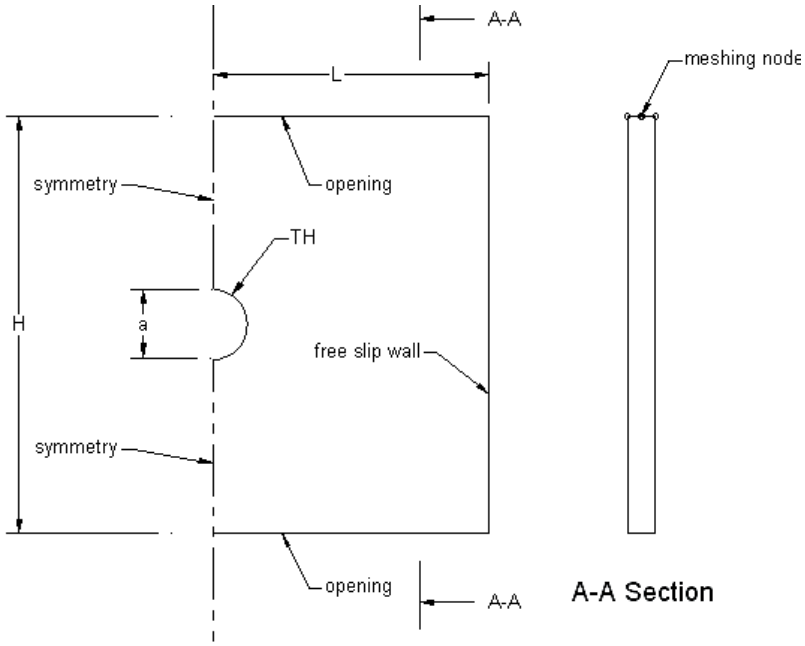

Figure 75-Geometry of heated horizontal cylinder in an infinite environment and its boundary conditions for simulation

Table 23-Boundary conditions and dimensions of the domain of heated horizontal cylinder for laminar natural convection

Parameter	**Value**
a	1.27 cm
H	21.27 cm
L	20 cm
Boundary	**Boundary details**
Cylinder	fixed temperature no slip wall
Top boundary	opening with fixed opening pressure relative $p = 0.0$ pa, $T = 305K$
Bottom boundary	opening with fixed opening pressure relative $p = 0.0$ pa, $T = 305K$
Right boundary	adiabatic free slip wall
Symmetry	Symmetry

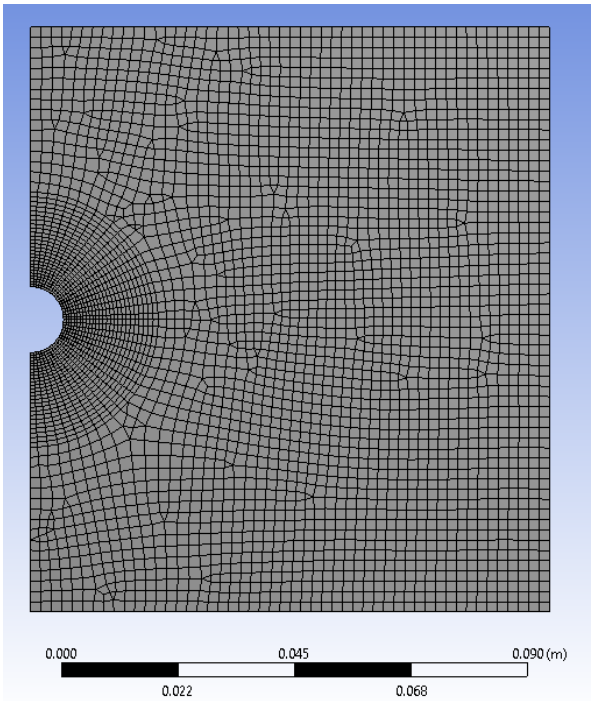

Figure 76-The coarse meshing of the domain for laminar natural convection flow around heated horizontal cylinder

Table 24-Details on different meshes used laminar natural convection around heated horizontal cylinder

Mesh	Domain dimensions	Grid size	Inflation layers	Cylinder rim size
a	L=20 cm H=21.27 cm	2 mm	Starting at 0.1 mm Inflation factor=1.03	0.2 mm
b	L=20 cm H=21.27 cm	2 mm	Starting at 0.05 mm Inflation factor=1.03	0.1 mm
c	L=25 cm H=31.27 cm	2 mm	Starting at 0.1 mm Inflation factor=1.03	0.2 mm
d	L=20 cm H=21.27 cm	2 mm	Starting at 0.1 mm Inflation factor=1.03	0.3 mm

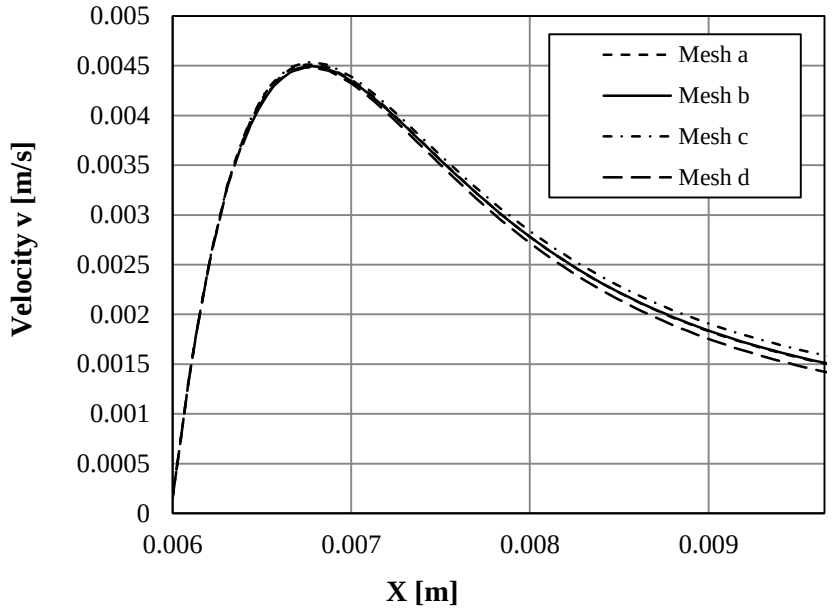

Figure 77-Velocity profile at Y=H/2 for different mesh sizes for laminar natural convection around horizontal cylinder

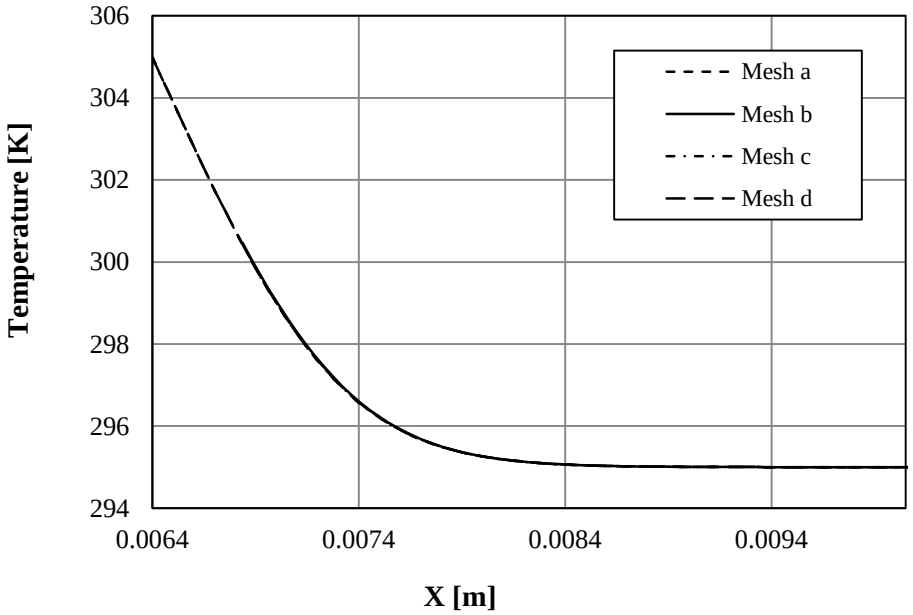

Figure 78-Temperature profile at Y=H/2 for different mesh sizes for laminar natural convection around horizontal cylinder

Velocity and temperature profiles at $Y = H/2$ are given in Figure 77 and Figure 78. As it is shown the profiles for different meshes are in very good agreement. Details on different grids used are given in Table 24. The calculated Nusselt numbers were compared with the experimental correlations in Table 25. As it is shown the Nusselt number from the simulation is in very good agreement with the experimental correlations. The error from the average of the Nusselt numbers from the correlations F, G and I (see Appendix C) is 1%.

Table 25-Comparison between the Nusselt numbers calculated computationally and from the experimental correlations for laminar natural convection around heated horizontal cylinder

Correlation	$\boldsymbol{Ra}$ **number range that correlations are applicable for**	**Nusselt Number for** $\boldsymbol{Ra} = 4.40 \times 10^5$
F [42]	$10^4 \leq Ra \leq 10^9$	13.7
G [44]	$10^4 \leq Ra \leq 10^7$	12.4
H [55]	$10^{-5} \leq Ra \leq 10^{12}$	14.0
I [55]	$10^{-6} \leq Ra \leq 10^9$	12.4
Simulation	-	12.7

5. Conclusions

Laminar natural convection for all three cases has shown promising results. Either comparing simulation data with an experimental benchmark, or using correlating equations, it is clear that the models have worked well. However modeling turbulent flow in either cavity or around cooled vertical plate is not as promising as it was for the laminar flow. In the cavity case, the $k - \omega$ model predicted the velocity and temperature profiles fairly well. However temperature was under-

predicted to some extent throughout the cross section of the cavity. Also the Nusselt numbers calculated for hot and cold walls have both about 17% error. One of the reasons that this error is higher for the top and bottom walls can be their approximated boundary condition. In the vertical plate case, the SST model under-predicted the Nusselt number by 22%. One thing that can be mentioned is that having a Rayleigh number of 10^{10} probably means that the flow is transient. This is because in this region a wide range of values is seen (Appendix C). Also the approximating nature of the equations or errors in experimental measurements can be a cause for the differences between the empirical correlations. However one common trend that is observed for both turbulent simulation results is that the Nusselt numbers calculated are by 15% to 25% less than what correlations predict.

It can be concluded that for laminar flows, CFD produced results in an excellent agreement with the experimental data. For turbulent flow, as Rundle [54] reported, the SST model does a better job in predicting the Nusselt numbers. However the Nusselt numbers are still being under-predicted by around 15% to 25%. CFD has been fairly successful in predicting different features of the flow, and the results are in close agreement with the experimental data.

Appendix B

CFD Modeling

1. Governing Equations

In order to study the fluid flow in detail, the CFD code solves the discretized forms of the equations of motion and heat transfer numerically. The differential equations for the conservation of mass, momentum and thermal energy are as follows:

$$\text{Continuity Equation: } \frac{\partial \rho}{\partial t} + \vec{\nabla}.\left(\rho \vec{U}\right) = 0 \tag{8}$$

$$\text{Momentum Equation: } \frac{\partial (\rho U)}{\partial t} + \vec{\nabla}.\left(\rho \vec{U} \times \vec{U}\right) = -\nabla p + \nabla.\tau + S_M \tag{9}$$

Where the stress tensor, τ, is related to the strain rate by

$$\tau = \mu\left(\nabla U + (\nabla U)^T - \frac{2}{3}\delta\nabla.U\right) \tag{10}$$

and,

$$The\ Thermal\ Energy\ Equation: \frac{\partial(\rho e)}{\partial t} + \nabla.\left(\rho\vec{U}e\right) = -\nabla.(\lambda\,\nabla\mathrm{T}) + p\,\nabla.U + \tau:\nabla U + S_E \tag{11}$$

where $'e'$ is the internal energy [46].

The above equations are integrated over control volumes that when agglomerated from the domain. Interpolation and linearization is used to create a set of algebraic equations which are solved iteratively. Solution on multiple grid density is critical to ensure that solutions are grid independent.

1.1. Buoyancy

For calculating buoyancy in flows with small temperature differences, a constant reference density ρ_{ref} is used for all terms, with a buoyancy source term added to the momentum equations in the direction of gravity. This term is given by:

$$S_{M,Buoy} = \left(\rho - \rho_{ref}\right)g \tag{12}$$

the density difference is then calculated using the Boussinesq approximation:

$$\rho - \rho_{ref} = -\rho_{ref}\beta\left(T - T_{ref}\right) \tag{13}$$

where β is the thermal expansion coefficient [46].

1.2. Turbulence

Turbulent flows can have large fluctuations in velocity and pressure and have a very wide range of time and length scales. Turbulent flows are unsteady and have length scales that are much smaller than the smallest finite volume mesh that can be used. Therefore, in these types of flows a statistical average of the flow field is solved for. This is done by applying the Reynolds averaging concept where the instantaneous quantity for example (U_i) is written as the sum of the mean value ($\overline{U}_i$) and a fluctuating value (u_i):

$$U_i = \overline{U}_i + u_i \tag{14}$$

By replacing the variables of the Navier-Stokes equations with their decomposition, the Reynolds-averaged Navier-Stokes equations 'RANS equations' are attained. These equations are conservation equations for the mean flow.

$$\text{Continuity Equation: } \frac{\partial \rho}{\partial t} + \frac{\partial}{\partial x_j}\left(\rho U_j\right) = 0 \tag{15}$$

$$\text{Momentum Equation: } \frac{\partial(\rho U_i)}{\partial \mathrm{t}} + \frac{\partial}{\partial x_j}\left(\rho U_i U_j\right) = -\frac{\partial p}{\partial x_i} + \frac{\partial}{\partial x_j}\left(\tau_{ij} - \rho\overline{u_i u_j}\right) + \mathrm{S_M} \tag{16}$$

in which the bar is dropped from the average velocity [46].

However, the RANS equations have new unknowns (Reynolds stresses) that are produced by the multiplication of the fluctuation terms and arise from the inherent non-linearity of the equations. In the current work an eddy viscosity model is used to close the RANS equations. This model assumes that the Reynolds stresses are proportional to the mean velocity gradients and the eddy viscosity (turbulent viscosity, μ_t):

$$-\rho\overline{u_i u_j} = \mu_t\left(\frac{\partial U_i}{\partial x_j}+\frac{\partial U_j}{\partial x_i}\right)-\frac{2}{3}\delta_{ij}\left(\rho k+\mu_t\frac{\partial U_k}{\partial x_k}\right) \quad (17)$$

The quantity μ_t has to be modeled [46]. While numerous models exist, two commonly applied two equation models are the $k-\varepsilon$ and $k-\omega$ models. In the $k-\varepsilon$ model, turbulence viscosity is assumed to be related to turbulence kinetic energy and dissipation while in the $k-\omega$ turbulence viscosity is assumed to be related to turbulent kinetic energy and turbulence frequency.

The $k-\omega$ model is more accurate and robust in treating the near wall computations in comparison to the $k-\varepsilon$ model [46]. However according to Menter [47] and [48], the main problem of the $k-\omega$ model is its high sensitivity to the free stream condition. Also neither of these two models account for the transport of turbulent shear stress which leads to over-predicting the eddy viscosity [46]. To overcome these deficiencies Menter suggested using $k-\omega$ model for the near wall regions and the $k-\varepsilon$ for the outer region which is the basics for the "Shear Stress Transport" (SST) model. The $k-\omega$ based SST model

as well as the Wilcox $k-\omega$ model are used for turbulence modeling throughout this work. The formulations of these models are given in Table 26.

Table 26-The formulations of turbulence models [46].

Turbulence model	Equations
The standard k-epsilon model	$\mu_t = C_\mu \rho \frac{k^2}{\varepsilon}$ $\frac{\partial(\rho k)}{\partial t} + \frac{\partial}{\partial x_j}(\rho U_j k) = \frac{\partial}{\partial x_j}\left[\left(\mu + \frac{\mu_t}{\sigma_k}\right)\frac{\partial k}{\partial x_j}\right] + P_k - \rho\varepsilon + P_{kb}$ $\frac{\partial(\rho \varepsilon)}{\partial t} + \frac{\partial}{\partial x_j}(\rho U_j \varepsilon) = \frac{\partial}{\partial x_j}\left[\left(\mu + \frac{\mu_t}{\sigma_\varepsilon}\right)\frac{\partial \varepsilon}{\partial x_j}\right] + \frac{\varepsilon}{k}(C_{\varepsilon 1}P_k - C_{\varepsilon 2}\rho\varepsilon + C_{\varepsilon 1}P_{\varepsilon b})$ $P_k = \mu_t\left(\frac{\partial U_i}{\partial x_j} + \frac{\partial U_j}{\partial x_i}\right)\frac{\partial U_i}{\partial x_j} - \frac{2}{3}\frac{\partial U_k}{\partial x_k}\left(3\mu_t\frac{\partial U_k}{\partial x_k} + \rho k\right)$ $C_{\varepsilon 1} = 1.44;\ C_{\varepsilon 2} = 1.92;\ C_\mu = 0.09;\ \sigma_k = 1.0;\ \sigma_\varepsilon = 1.3$
The Wilcox k-omega model	$\mu_t = \rho \frac{k}{\omega}$ $\frac{\partial(\rho k)}{\partial t} + \frac{\partial}{\partial x_j}(\rho U_j k) = \frac{\partial}{\partial x_j}\left[\left(\mu + \frac{\mu_t}{\sigma_k}\right)\frac{\partial k}{\partial x_j}\right] + P_k - \beta'\rho k\omega + P_{kb}$ $\frac{\partial(\rho \omega)}{\partial t} + \frac{\partial}{\partial x_j}(\rho U_j \omega) = \frac{\partial}{\partial x_j}\left[\left(\mu + \frac{\mu_t}{\sigma_\omega}\right)\frac{\partial \omega}{\partial x_j}\right] + \alpha\frac{\omega}{k}P_k - \beta\rho\omega^2 + P_{\omega b}$ $P_k = \mu_t\left(\frac{\partial U_i}{\partial x_j} + \frac{\partial U_j}{\partial x_i}\right)\frac{\partial U_i}{\partial x_j} - \frac{2}{3}\frac{\partial U_k}{\partial x_k}\left(3\mu_t\frac{\partial U_k}{\partial x_k} + \rho k\right)$ $\beta' = 0.09;\ \alpha = \frac{5}{9};\ \beta = 0.075;\ \sigma_k = 2;\ \sigma_\omega = 2$
The Shear Stress Transport (SST) model	$\frac{\partial(\rho k)}{\partial t} + \frac{\partial}{\partial x_j}(\rho U_j k) = \frac{\partial}{\partial x_j}\left[\left(\mu + \frac{\mu_t}{\sigma_{k3}}\right)\frac{\partial k}{\partial x_j}\right] + P_k - \beta'\rho k\omega + P_{kb}$

	$\frac{\partial(\rho\omega)}{\partial t}+\frac{\partial}{\partial x_j}(\rho U_j\omega)$ $=\frac{\partial}{\partial x_j}\left[\left(\mu+\frac{\mu_t}{\sigma_{\omega 3}}\right)\frac{\partial\omega}{\partial x_j}\right]+(1-F_1)2\rho\frac{1}{\sigma_{\omega 2}\,\omega}\frac{\partial k}{\partial x_j}\frac{\partial\omega}{\partial x_j}$ $+\alpha_3\frac{\omega}{k}P_k-\beta_3\rho\omega^2+P_{\omega b}$ $\phi_3=F_1\phi_1+(1-F_1)\phi_2$ $\beta'=0.09;\ \alpha_1=\frac{5}{9};\ \beta_1=0.075;\ \sigma_{k1}=2;\ \sigma_{\omega 1}=2$ $\alpha_2=0.44;\ \beta_2=0.0828;\ \sigma_{k2}=1;\ \sigma_{\omega 2}=\frac{1}{0.0856}$ $\nu_t=\frac{a_1 k}{\max(a_1\omega, SF_2)};\ \nu_t=\frac{\mu_t}{\rho}$ $F_1=\tanh(arg_1{}^4);\ arg_1=\min\left(\max\left(\frac{\sqrt{k}}{\beta'\omega\, y},\frac{500\nu}{y^2\,\omega}\right),\frac{4\rho k}{CD_{k\omega}\sigma_\omega 2y^2}\right)$ $CD_{k\omega}=\max\left(2\rho\frac{1}{\sigma_{\omega 2}\,\omega}\frac{\partial k}{\partial x_j}\frac{\partial\omega}{\partial x_j},1.0x10^{-10}\right)$ $F_2=tanh(arg_2{}^2);\ arg_2=\max\left(\frac{2\sqrt{k}}{\beta'\omega\, y},\frac{500\nu}{y^2\,\omega}\right)$

2. Boundary Conditions

Three different boundary conditions have been used in this study: opening, no slip wall and symmetry plane. At the opening boundary condition, the fluid can flow either into the domain, out of the domain or a mixture of both. By specifying a value for the relative pressure at the opening, the code interprets the value as the relative total pressure for flow inwards, and as the relative static pressure for flow outwards. The static temperature can also be specified at the opening boundary. At the no slip wall boundary condition all the velocity components are set to be zero. At the symmetry plane boundary condition, the properties of the flow are

mirrored. The scalar variable gradient as well as the velocity normal to the plane is set to zero [46].

Appendix C

Experimental Correlations for Natural Convention

1. Fixed Temperature Vertical Flat Plates

For natural convection around fixed temperature vertical flat plate, empirical correlations have been developed by researchers and are available in the literature. These correlations usually relate the average Nusselt number to Grashof number and Prandtl number. The definitions for these dimensionless numbers are given in the nomenclature. The correlations that were used in this study are given in Table 27. The characteristic length in evaluating the Rayleigh number for vertical flat plates is the length of the plate.

Table 27-Empirical correlations for laminar and turbulent natural convection around fixed temperature vertical flat plates used in this study

Name	$Ra_f = Gr_f Pr_f$	Correlation formula	Reference(s)
A	$10^4 \leq Ra_f \leq 10^9$	$\overline{Nu_f} = 0.59\ {Ra_f}^{1/4}$	McAdams [42]
B	$Ra_f \leq 10^9$	$\overline{Nu_f} = 0.68 + \frac{0.670\ {Ra_f}^{1/4}}{\left[1 + \left(0.492/Pr_f\right)^{9/16}\right]^{4/9}}$	Churchill and Chu [43]
C	$10^{-1} \leq Ra_f \leq 10^{12}$	$\overline{Nu_f} = \left[0.825 + \frac{0.387\ {Ra_f}^{1/6}}{\left[1 + \left(0.492/Pr_f\right)^{9/16}\right]^{8/27}}\right]^2$	Churchill and Chu [43]
D	$10^9 \leq Ra_f \leq 10^{13}$	$\overline{Nu_f} = 0.021\ {Ra_f}^{2/5}$	Eckert and Jackson [51]
E	$10^9 \leq Ra_f \leq 10^{13}$	$\overline{Nu_f} = 0.1\ {Ra_f}^{1/3}$	Warner and Arpaci [49], Bayley [50]

To compare these correlations, Nusselt number is plotted versus Rayleigh number for water at 25℃ (Pr= 5.83), and the graph is given in Figure 79. As it is shown in the graph, the correlations A and B for the laminar region ($Ra_f \leq 10^9$) match well. Also in the turbulent region the correlations D and E are fairly close. However correlation E is preferred by Holman [40]. Correlation C only matches the two correlations A and B when $Ra_f \leq 10^7$, but for higher Rayleigh numbers and in the turbulent region it is far from the recommended correlation E.

Therefore the best correlations to be used for laminar region are A and B, and for turbulent region is E.

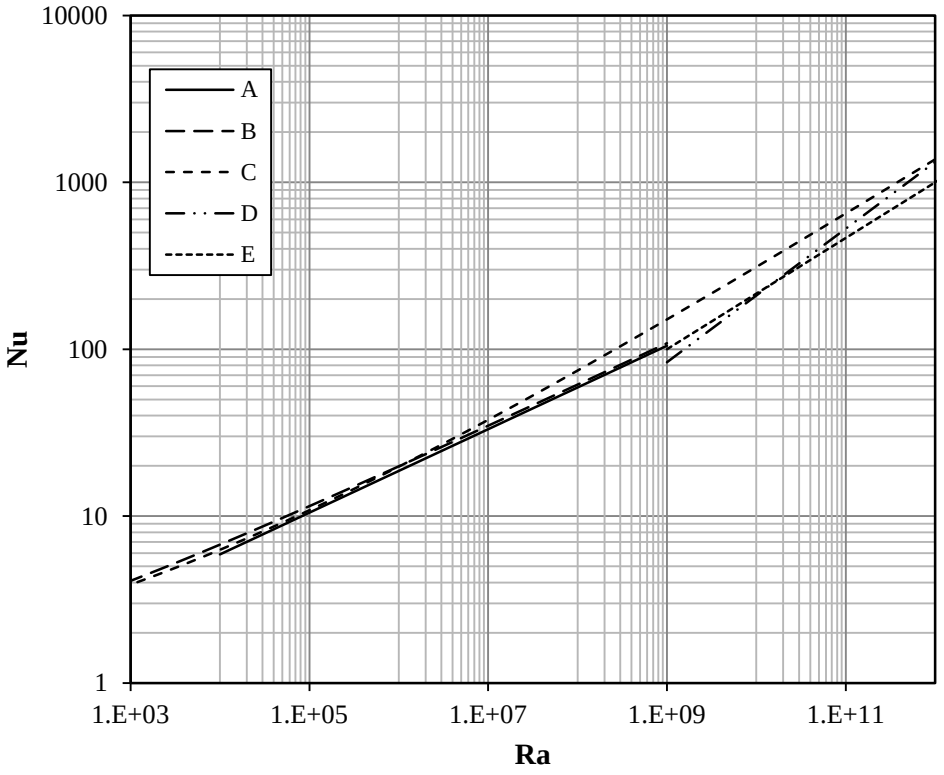

Figure 79-A comparison between different correlations available for natural convection flow arounf fixed temperature vertical flat plate

2. Fixed Temperature Horizontal Cylinders

For natural convection around fixed temperature horizontal cylinder, empirical correlations have been developed by researchers. The correlations that were used in this study for laminar flow are given in Table 28. The characteristic length in evaluating the Rayleigh number for horizontal cylinders is the diameter of the cylinder.

Table 28-Empirical correlations for laminar and turbulent natural convection around fixed temperature horizontal cylinders used in this study

Name	$Ra_f = Gr_f Pr_f$	Correlation formula	Reference
F	$10^4 \leq Ra_f \leq 10^9$	$\overline{Nu_f} = 0.53\ {Ra_f}^{1/4}$	McAdams [42]
G	$10^4 \leq Ra_f \leq 10^7$	$\overline{Nu_f} = 0.480\ {Ra_f}^{1/4}$	Morgan [44]
H	$10^{-5} \leq Ra_f \leq 10^{12}$	$\overline{Nu_f} = \left[0.60 + 0.387\left\{\frac{Ra_f}{\left[1+\left(0.559/Pr_f\right)^{9/16}\right]^{16/9}}\right\}^{1/6}\right]^2$	Churchill and Chu [55]
I	$10^{-6} \leq Ra_f \leq 10^9$	$\overline{Nu_f} = 0.36 + \frac{0.518\ {Ra_f}^{1/4}}{\left[1+\left(0.559/Pr_f\right)^{9/16}\right]^{4/9}}$	Churchill and Chu [55]

These correlations are plotted in Figure 80 for comparison. This graph is generated for water at 25℃. Figure 80 shows that the correlations are in good agreement for low Rayleigh numbers (less than 10^5), but then they diverge. The Rayleigh number that this study is dealing with is around 10^5, and if there is any differences between the evaluated Nusselt numbers from different correlations, their average will be taken into account.

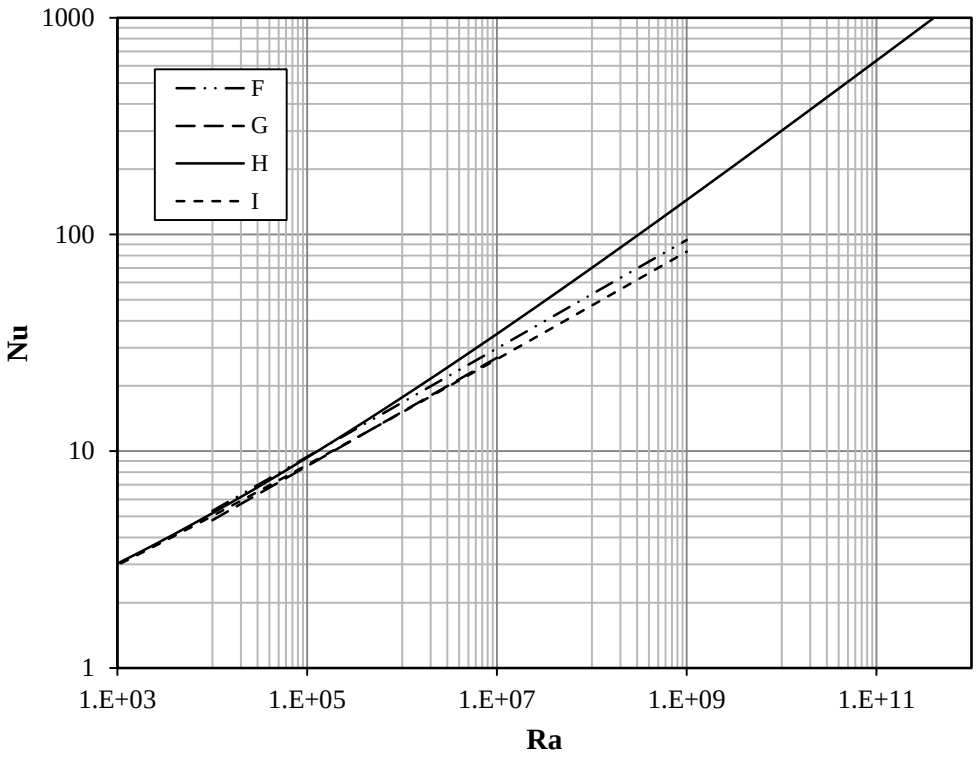

Figure 80-A comparison between different correlations available for natural convection flow around fixed temperature horizontal cylinder